

A FEASIBILITY STUDY OF THIN-SHELL DEFORMABLE MIRRORS WITH  
ADAPTIVE TRUSS SUPPORT FOR SPACED-BASED TELESCOPES

A Thesis  
Presented to  
The Academic Faculty

By

Russell K. Marzette, Jr.

In Partial Fulfilment  
Of the Requirements for the Degree  
Master of Science in Mechanical Engineering

Georgia Institute of Technology

August 2006

A FEASIBILITY STUDY OF THIN-SHELL DEFORMABLE MIRRORS WITH  
ADAPTIVE TRUSS SUPPORT FOR SPACED-BASED TELESCOPES

Approved by:

Dr. Harvey Lipkin, Advisor  
School of Mechanical Engineering  
Georgia Institute of Technology

Dr. Suresh K. Sitaraman  
School of Mechanical Engineering  
Georgia Institute of Technology

Dr. Ifeanyi Charles Ume  
School of Mechanical Engineering  
Georgia Institute of Technology

Date Approved: July 10, 2006

## ACKNOWLEDGEMENTS

I thank God for bringing about the fruition of this work; for bringing this chapter of my life to a successful close. I thank God for a wonderful and unconditionally supportive family. I thank God for my *church* family and close friends in and outside of Christ.

I thank the NASA Graduate Student Research Program for its generous financial support, in addition to that of Dr. Harvey Lipkin.

# TABLE OF CONTENTS

<b>ACKNOWLEDGEMENTS.....</b>	<b>III</b>
<b>LIST OF TABLES .....</b>	<b>VI</b>
<b>LIST OF FIGURES .....</b>	<b>VII</b>
<b>SUMMARY .....</b>	<b>XII</b>
<b>CHAPTER 1 INTRODUCTION .....</b>	<b>1</b>
1.1 Terrestrial and Space-Based Telescopes .....	1
1.2 Adaptive Optics .....	7
1.3 Summary and Objective.....	11
1.4 Major Contributions.....	12
<b>CHAPTER 2 INITIAL MODEL DEVELOPMENT .....</b>	<b>14</b>
2.1 Initial Model Development .....	14
2.2 Three Dimensional Modelling .....	17
2.3 FEM Model Development .....	21
2.4 Material Properties and Relevant Dimensioning.....	29
<b>CHAPTER 3 EVALUATION AND COMPUTATIONAL METHOD .....</b>	<b>31</b>
3.1 Introduction.....	31
3.2 Zernike Polynomials and Approximation of the OPD .....	34
3.3 Actuator Influence Coefficients .....	35
3.4 Determining the Actuators Strokes: Least Squares Fit of Influence Coefficient Data .....	37
3.5 Primary Metric of Evaluation: RMS Error.....	40
3.6 Optical Requirements of the Deformable Mirror .....	41
<b>CHAPTER 4 DEVELOPMENT OF A BASELINE 3D MODEL.....</b>	<b>43</b>
4.1 Introduction.....	43
4.2 Baseline Comparison: Zernike Modes .....	46
4.3 Baseline Comparison: Number of Actuators .....	50
4.4 Modality and Comments on Modes 7 and 10 .....	56
4.5 Surface Thickness .....	61
4.6 Truss Height.....	63
4.7 Qualitative Evaluation of Print-Through.....	69
4.8 Conclusions and Design Criteria for Feasibility .....	75
<b>CHAPTER 5 ANALYSIS OF THE SPA DEFORMABLE MIRROR FOR SELECT THERMAL GRADIENTS.....</b>	<b>77</b>
5.1 Thermal Boundary Conditions .....	78
5.2 Deformable Mirror Aberration: Negligible Substrate Structural Influence (Facesheet-Only) 79	79
5.3 Deformable Mirror Aberration: Comparison of Matched and Mismatched CTE cases .....	81
5.4 Deformable Mirror Aberration: Zero Substrate CTE.....	83
5.5 Summary of Thermal Loading.....	88
<b>CHAPTER 6 EVALUATION OF MODEL LINEARITY, ACTUATOR GLITCH, AND FORCE LEVELS.....</b>	<b>90</b>
6.1 Numerical (FEM) Verification of Linearity.....	90
6.2 Actuator Glitch.....	94
6.3 Actuator Forces and Stroke Levels .....	104
6.4 Summary .....	111
<b>CHAPTER 7 CONCLUSIONS.....</b>	<b>113</b>
<b>CHAPTER 8 FUTURE WORK.....</b>	<b>116</b>
<b>APPENDIX A MATERIAL PROPERTIES.....</b>	<b>120</b>

<b>APPENDIX B SPA AND SNA PERFORMANCE FOR HIGH ACTUATOR QUANTITIES ...</b>	<b>121</b>
<b>APPENDIX C SPA AND SNA P2V FOR LOW ACTUATOR QUANTITIES .....</b>	<b>123</b>
<b>APPENDIX D SPA AND SNA P2V FOR VARYING TRUSS HEIGHTS .....</b>	<b>125</b>
<b>REFERENCES.....</b>	<b>127</b>

## LIST OF TABLES

Table 1.	ANSYS Element Type Descriptions.....	28
Table 2.	Baseline SPA and SNA Case Parameters.....	45
Table 3.	Modes without Sinusoidal Components.....	49
Table 4.	Zernike Modes Used in Evaluation of Print-Through.....	70
Table 5.	Peak to Valley Deformations for the cases shown in Figure 70.....	85
Table 6.	Peak to Valley Deformations for cases shown in Figure 71.....	86
Table 7.	Summary Reproduction vs. Correction in terms of Normalized and Absolute Error for 15, 159, and 1563 Actuators. ....	94
Table 8.	Discrete vs. Random Glitch - Comparison of RMS value for 15, 159, and 1563 Actuators.....	100
Table 9.	Residual RMS Error and Operable Cut-off Wavelength.....	104
Table 10.	Performance Values for Representative Thermal Loads, 15- 1563 Actuators, and Stiffness of 68.3 GPa.....	107
Table 11.	Performance Values for Representative Thermal Loads, 15- 1563 Actuators, and Stiffness of 68.3 MPa.....	110
Table 12.	Material Properties for Each Component.....	120

## LIST OF FIGURES

Figure 1.	External View of the SUBARU Observatory.....	1
Figure 2.	Monolithic Actuator Supported Primary Deformable Mirror of SUBARU Telescope.....	2
Figure 3.	External View of the Hobby-Eberly Telescope.....	2
Figure 4.	Segmented Primary Mirror of the Hobby-Eberly Telescope.....	3
Figure 5.	Twin Domes of Keck Observatory .....	3
Figure 6.	One Twin Primary Mirror of the Keck Observatory.....	4
Figure 7.	Conceptual Rendering of the OWL Telescope .....	5
Figure 8.	NASA JWST Full Scale Model. ....	6
Figure 9.	Simplified Optical Train showing an AO System [11]. ....	8
Figure 10.	(a) Segmented and (b) Continuous Facesheet.....	10
Figure 11.	Surface Normal Actuation. ....	14
Figure 12.	Surface Parallel Actuation. ....	15
Figure 13.	(a) 2D Surface Normal and (b) Surface Parallel Influence Coefficients.....	16
Figure 14.	Global Coordinate System of Mirror.....	17
Figure 15.	3D SPA Hexagonal Truss Layout.....	17
Figure 16.	SPA Deformation Mirror Model.....	18
Figure 17:	3D Perspective View of SPA Deformable Mirror .....	19
Figure 18.	Facesheet Section/Cut Away with Exposed Substrate.....	19
Figure 19.	Bipedal Tripod Leg and Equivalent Single Actuator.....	20
Figure 20.	3D SNA Hexagonal Truss Layout. ....	20
Figure 21.	(a) Standard SPA Footprint, (b) Standard SNA Footprint.....	21
Figure 22.	Geometric Setup of the SPA Deformable Mirror .....	22
Figure 23:	Illustration of Hexagonal Prisms and Sphere (Top View) .....	23
Figure 24.	ANSYS Actuator Element (LINK 11) .....	29

Figure 25.	MATLAB GUI (STAS).....	32
Figure 26.	Evaluation, Methodology, and Process Flow. ....	33
Figure 27.	First 6 Zernike Polynomials.....	35
Figure 28.	3D SNA Influence Coefficient Example.....	36
Figure 29.	3D SPA Influence Coefficient Example.....	37
Figure 30.	Three Aberration Correction Approaches. ....	38
Figure 31.	Electromagnetic Spectrum from 400-5000 nm.....	42
Figure 32.	SNA vs. SPA Baseline Comparison for the First Sixty-Six Zernike Polynomials.....	46
Figure 33.	Percent Error Improvement of SPA over SNA for 243 Actuators.....	47
Figure 34.	SNA vs. SPA Baseline P2V Comparison for the First 66 Zernike Polynomials.....	48
Figure 35.	Improvement of SPA over SNA in term of P2V. ....	49
Figure 36.	SPA vs. SNA Rate of Change for RMS Errors.....	50
Figure 37.	Percent Error Improvement of SPA over SNA for 243, 933, 2073, and 3663.....	51
Figure 38.	SPA RMS Error for 15-933 Actuators. ....	52
Figure 39.	SNA RMS Error for 15-933 Actuators.....	52
Figure 40.	SPA P2V Performance for 243, 933, 2073, and 3663 Actuators.....	54
Figure 41.	SNA P2V Performance for 243, 933, 2073, and 3663 Actuators.....	54
Figure 42.	Ratio of SPA to SNA P2V for 243, 933, 2073, and 3663 Actuators.....	55
Figure 43:	Zernike Polynomial 7 .....	56
Figure 44.	Zernike Polynomial 10 .....	57
Figure 45.	Symmetry Zernike Mode 9.....	58
Figure 46.	Symmetry Zernike Mode 10 .....	59
Figure 47.	Zernike Polynomial 17 .....	60
Figure 48.	Zernike Polynomial 20 .....	60

Figure 49.	SPA RMS Error for Thickness of 50-25000 $\mu\text{m}$ for 243 Actuators.....	62
Figure 50.	SNA RMS Error for Thicknesses of 50-25000 $\mu\text{m}$ for 243 Actuators.....	62
Figure 51.	Improvement of SPA over SNA for Thicknesses of 50-500 $\mu\text{m}$ . .....	63
Figure 52.	Simplified Truss Bending. ....	64
Figure 53.	Simplified Single Span Displacement as a Function of Percent Decreased in Nominal Truss Height, $d$ .....	65
Figure 54.	SPA Deflection for 100% Truss Height and 243 Actuators. ....	66
Figure 55.	SPA P2V Deflection for 10% Truss Height and 243 Actuators. ....	67
Figure 56.	RMS Error for 100% and 10% truss height for 243 actuators. ....	68
Figure 57.	SPA Zernike Mode 10 - $r^3 \sin(3\theta)$ . ....	71
Figure 58.	SNA Zernike Mode 10 - $r^3 \sin(3\theta)$ . ....	71
Figure 59.	SPA Zernike Mode 14 - $(4r^4 - 3r^2) \sin(2\theta)$ . ....	72
Figure 60.	SNA Zernike Mode 14 - $(4r^4 - 3r^2) \sin(2\theta)$ . ....	72
Figure 61.	SPA Zernike Mode 18 - $(10r^5 - 12r^3 + 3r) \cos(\theta)$ . ....	73
Figure 62.	SNA Zernike Mode 18 - $(10r^5 - 12r^3 + 3r) \cos(\theta)$ . ....	73
Figure 63.	SPA Zernike Mode 16 - $r^5 \cos(5\theta)$ . ....	74
Figure 64.	SNA Zernike Mode 16 - $r^5 \cos(5\theta)$ . ....	74
Figure 64.	STAS Thermal Constraints (Boundary Conditions) .....	78
Figure 65.	FEM Cross-sheet of Facesheet, Truss, and Tripod .....	79
Figure 66.	Facesheet-Only Simulation - 10°C Uniform Load for 4 m Aperture. ....	81
Figure 67.	Comparison of CTE Match/Mismatch: 159 Actuators - 10°C. ....	82
Figure 68.	Comparison of CTE Match/Mismatch: 159 Actuators - 1°C/m. ....	82
Figure 69.	Facesheet-Only Simulation - 1°C/m Uniform Load for 2 m Aperture. ....	83
Figure 70.	Mirrors with 15 to 11775 Actuators and a 10°C Uniform Thermal Load. ....	85

Figure 71.	Mirrors with 15 to 11775 Actuators, with 1°C/m Thermal Load. ....	86
Figure 72.	159 Actuators with Mismatched CTE and 1°C/m Thermal Loads in the Y and XY directions.....	87
Figure 73.	Reproduction vs. Correction 15 Actuators 10°C Uniform Thermal Load.....	91
Figure 74.	Reproduction vs. Correction 15 Actuators 1°C/m Thermal Load.....	92
Figure 75.	Reproduction vs. Correction for 159 Actuators 10°C Uniform Thermal Load.....	93
Figure 76.	Reproduction vs. Correction 159 Actuators 1°C/m Thermal Load.....	93
Figure 77.	Random glitch applied to an unloaded facesheet (15 Actuators).....	95
Figure 78.	Random Glitch applied to a Unloaded Mirror (a) 159 and (b) 1563 Actuators. ....	96
Figure 79:	Visible Spectrum Exclude from Operation by Random Glitch - 159 Actuators.....	96
Figure 80:	Depiction of Spectrum Excluded by Random Glitch (1563 Actuators) .....	97
Figure 81.	Discrete vs. Random Glitch – 15 Actuators 10°C Thermal Load.....	97
Figure 82.	Discrete vs. Random Glitch – 159 Actuators 10°C Thermal Load.....	98
Figure 83.	Discrete vs. Random Glitch – 1563 Actuators 10°C Thermal Load.....	98
Figure 84.	Discrete vs. Random Glitch – 15 Actuators 1°C/m Thermal Load.....	99
Figure 85.	Discrete vs. Random Glitch – 159 Actuators 1°C/m Thermal Load.....	99
Figure 86.	Discrete vs. Random Glitch – 1563 Actuators 1°C/m Thermal Load.....	100
Figure 87.	Actuator Force Plot for 15 Actuators 10°C - Thermal Load. ....	105
Figure 88.	Actuator Force Plot for 159 Actuators 10°C - Thermal Load. ....	105
Figure 89.	Actuator Force Plot for 15 Actuators - 1°C/m Thermal Load. ....	106

Figure 90.	Actuator Force Plot for 159 Actuators - 1°C/m Thermal Load. ....	106
Figure 92.	SNA RMS Error for 243, 933, 2073, and 3663. ....	121
Figure 93.	SNA RMS Error for 243, 933, 2073, and 3663. ....	122
Figure 94.	SPA P2V Performance for 15-933 Actuators. ....	123
Figure 95.	SNA P2V Performance for 15-933 Actuators. ....	124
Figure 95.	SPA P2V Deflection for 15- 933 Actuators for 100% Truss Height. ....	125
Figure 96.	SPA P2V Deflection for 15- 933 Actuators for 10% Truss Height. ....	126

## SUMMARY

Space-based telescopes are limited by the payload requirements of existing launch vehicles. Thus, despite distinct advantages the resolution of terrestrial telescopes exceeds space-based telescopes due to larger size and powerful adaptive optics. To overcome payload limitations, a primary mirror technology that is lighter in weight, but no less effective, is required. As this will result in new structural conditions, new approaches to maintaining the optical shape (figure) of the mirror will also be required.

This thesis culminates work at the Georgia Institute of Technology in modelling a hexagonal thin-shell deformation mirror manipulated by an adaptive truss. This research specifically examines the feasibility of a surface parallel actuated (SPA) thin-shell CuZr deformable mirror (DM) as an alternative to a typical surface normal actuated (SNA) based mirror. It is believed that by using a thin-shell mirror (100  $\mu\text{m}$  or less in thickness) with a light weight substrate, such as a truss, that a significant weight-savings will occur, thus enabling larger space-based telescopes.

This thesis advances the SPA DM concept by 1) creating a representative model, 2) developing design evaluation methods, 3) evaluating the FEA simulated response of the deformable mirror over Zernike error modes, 4) evaluating the FEA simulated response to select thermal loads, and 5) evaluating the ability of the DM to remove thermal error, and the forces required to do so. Finally, it is concluded that overall the SPA DM concept is feasible.

# CHAPTER 1

## INTRODUCTION

The size of space-based telescopes is limited by the payload requirements of existing launch vehicles. It is this limitation that allows the quality of terrestrial telescope images to exceed that of space-based telescopes. To overcome payload limitations, a primary deformable mirror (DM) technology that is lighter in weight, but no less effective, is required. After a review of several examples of existing and proposed observatories and a brief discussion of adaptive optics, it is proposed that a thin-shell mirror maintained by an adaptive-truss is a viable alternative to existing DM technology.

### **1.1 Terrestrial and Space-Based Telescopes**

The SUBARU telescope, shown in Figure 1, has an 8.2 m aperture monolithic primary mirror. Two hundred sixty-one adaptive optics actuators, mounted to the back of the primary mirror (Figure 2), enhance image quality by controlling the optical shape or *figure* of the mirror. Nearly every modern telescope uses a similar DM.

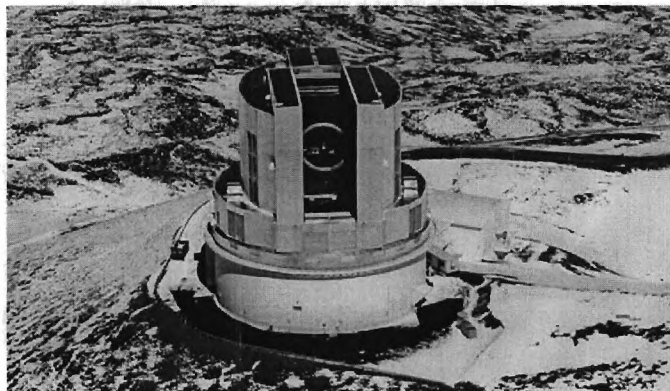


Figure 1. External View of the SUBARU Observatory.

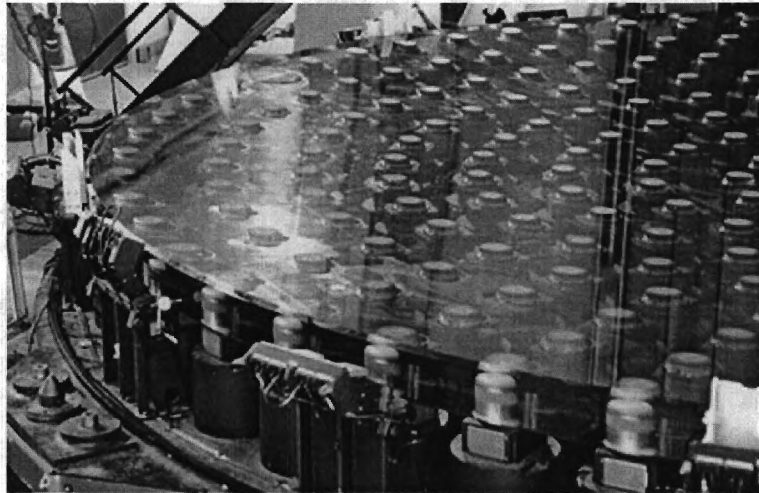


Figure 2. Monolithic Actuator Supported Primary Deformable Mirror of SUBARU Telescope.

University of Texas at Austin operates the Hobby-Eberly Telescope (HET), a segmented optical telescope that engages in spectroscopy (Figure 3). It has an effective aperture of 9.2 m (Figure 4). Each hexagonal segment is 1 m from flat-to-flat and weighs 250 lbs. There are three actuators per a segment that maintain the relative position of each segment [1, 2]. A deformable mirror similar to the primary mirror of the SUBARU is located elsewhere in the optical train.

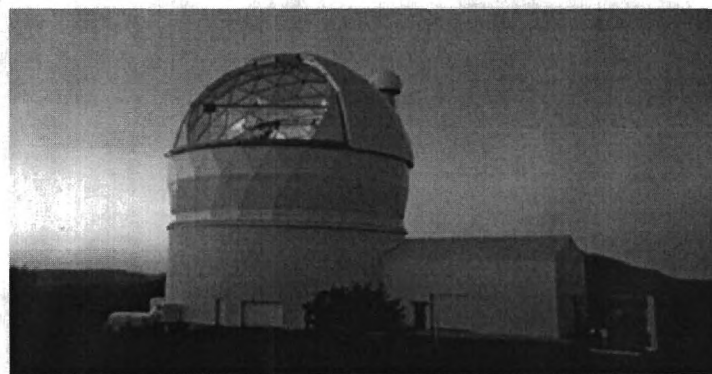


Figure 3. External View of the Hobby-Eberly Telescope.



Figure 4. Segmented Primary Mirror of the Hobby-Eberly Telescope.

The Keck observatory atop Mt. Mauna Kea in Hawaii houses twin 10 m optical telescopes, the largest in the world (Figure 5). The observatory benefits from two decades of significant innovations, specifically segmented mirrors, adaptive and active optics, and materials with increased strength to weight ratios. The observatory began making scientific observations in 1993 (It should be noted that on November 11, 2005 the South African Large Telescope (SALT), modeled after the HET was commissioned. It is also a 10 m aperture optical telescope).



Figure 5. Twin Domes of Keck Observatory

The adaptive and active optics systems of the telescopes are extensive and profoundly improve image quality. Both Keck telescopes utilize a thirty-six segment primary mirror (Figure 6).

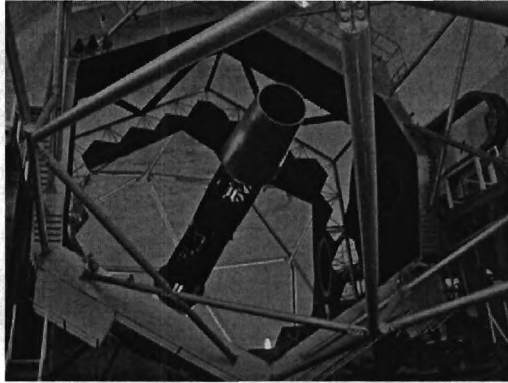


Figure 6. One Twin Primary Mirror of the Keck Observatory

Each hexagonal segment is 1.8 m from flat to flat, 7.5 cm thick, and weighs about a half-ton [3]. Three actuators per segment maintain the relative alignment of each segment. The mainstay of the image enhancing adaptive optics is found downstream of the primary mirrors of each telescope, in secondary and tertiary mirrors [4].

While the previously mentioned telescopes are “large” by today’s standards, they are small compared to ongoing projects, such as the “100 m class” (100 m aperture size) OWL in Figure 7. The OWL design proposes a primary mirror of 3048 segments and a secondary of 216. Each hexagonal segment would weigh 980 lbs and be 1.6 m (flat-to-flat) and 7 cm thick [5, 6].

With the above examples in mind, the key features to observe regarding terrestrial telescopes are that 1) as aperture size increases the mirror is thickened to

provide additional rigidity and the aerial density (mass per unit surface area) increases, and 2) some form of adaptive optics is used to maintain image quality.

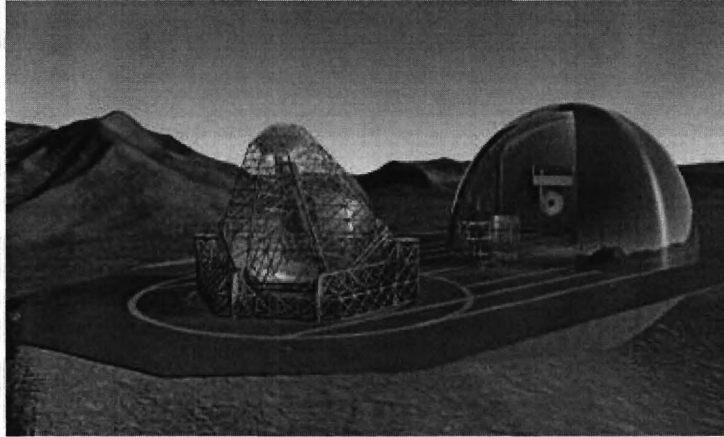


Figure 7. Conceptual Rendering of the OWL Telescope

Though a 100 m space-based telescope is no where near a reality at this time, a 10 m telescope is well within the expectations of current and emerging technologies. Spaced-based telescopes have several advantages over terrestrial telescopes, such as there ability to take prolonged exposures of objects, unobstructed field of view, and lack of atmospheric interference.

Currently, the Hubble Space Telescope (HST) is the only general use optical observatory in space. It suffices to say that with an aperture of 2.4 m, the Hubble is the equivalent of a small terrestrial telescope.

NASA's James Webb Space Telescope (JWST) is the primary initiative at this time to *narrow* the gap between space-based and terrestrial telescope technologies (Figure 8).

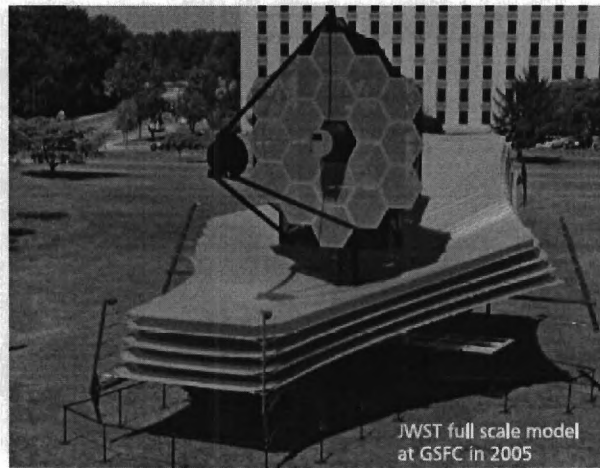


Figure 8. NASA JWST Full Scale Model.

The JWST is scheduled to launch in 2013 and will self-deploy from an existing rocket (i.e. the use of a space shuttle or new launch vehicle is not required). It will possess a ribbed, hexagonal, 18-segment, 6.5 m primary mirror, that will provide the same image quality as current adaptive optics enabled terrestrial 8 m telescopes. The aerial density of the JWST primary mirror will be between  $10 - 20 \text{ kg/m}^2$ , a factor of 100 when compared to the Hubble's  $180 \text{ kg/m}^2$  mirror. With its much larger and lighter mirror, its imaging ability will eclipse the Hubble considerably [3, 7, 8].

With image quality only as good as an 8 m terrestrial telescope, the JWST will not however exceed the image quality of the Keck observatory. To bridge the gap between space-based and terrestrial telescopes thinner, larger, and lighter mirrors are required. Further reductions in aerial density and advances in portability must be achieved and the resulting new structural conditions will likely necessitate that new control techniques be applied to the mirror figure.

Research teams at the Georgia Institute of Technology, the University of Florida, the National Reconnaissance Organization (NRO), Xinetics, Inc., and

NASA's Jet Propulsion Laboratory (JPL) have collaborated on varying aspects of a new, patented [9], deformable mirror technology, with the potential to meet future space-based needs. This thesis does not contribute the initial work resulting in the patent, but the subsequent body of work suggesting that a thin-shell deformable mirror supported by an adaptive truss can address the need for thinner lighter primary mirrors, and provide the additional figure control associated with thinner mirrors. Subsequent to the contributions from Georgia Tech, JPL continues to develop lightweight, large-displacement, low-force piezoelectric inch-worm actuators for integration into the adaptive truss [10], and Xinetics and NRO contractors continue to develop similar thin-shell ribbed mirrors with embedded actuators.

The next section discusses relevant adaptive optics background.

## **1.2 Adaptive Optics**

The field of adaptive optics (AO) has found application in both civilian and military arenas, such as projectile tracking, astronomy, and optical communications. With regard to astronomy, an incoming image is presented to the primary mirror of the telescope as a continually changing wavefront (Figure 9). That wavefront is passed through the optical train of the telescope to an observing instrument. An AO system, which is a component of the optical train, can be split into inertial and non-inertial (molecular in nature) approaches based upon the way in which the wavefront is influenced [11]. A non-inertial approach might involve the use of a magnetic field to modify an incoming wavefront; a similar principle is used in the picture tube of a television in which a beam of electrons is directed to produce the image seen by the viewer. No consideration of such molecular approaches is necessary for this research.

An inertial adaptive optics (AO) system uses mechanical means to reshape an incoming wavefront by adjusting a mirror or lens and thereby changing the phase of the wavefront

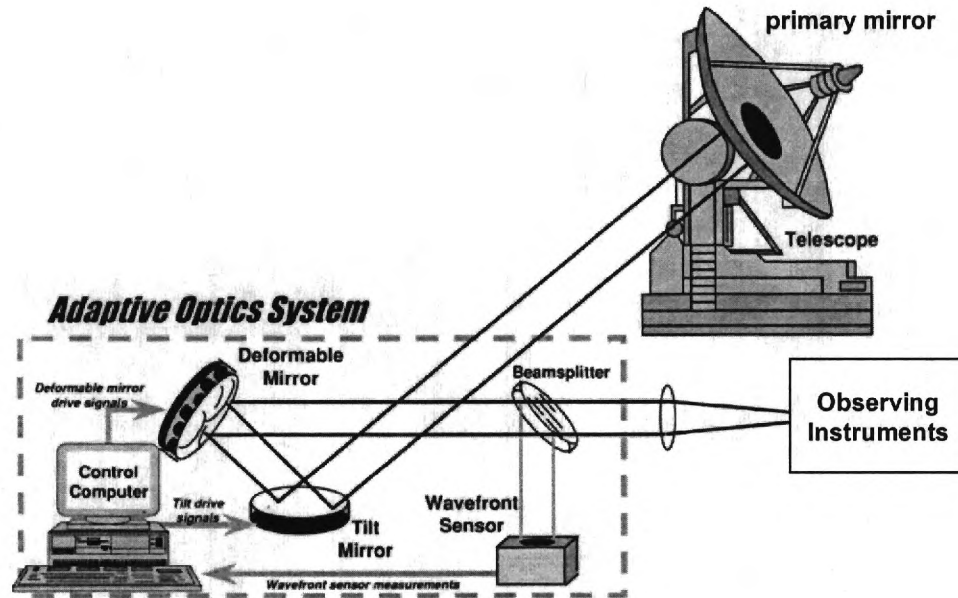


Figure 9. Simplified Optical Train showing an AO System [11].

The AO system of a terrestrial telescope copes with continual disturbances from the atmosphere at varying frequencies and with subtle temperature variations. Large aperture mirrors require compensation for gravitational sag. Space-based telescopes may encounter distortion due to thermal loads that distort the optics. In either case, the AO system must dynamically sense errors and correct the wavefront accordingly.

A number of configurations can be used in the design of an AO system, from a few basic component categories, functional types, and parameters. Depending upon the application, inertial adaptive optics may also be referred to as *active optics* which typically operate at 2 Hz or less. Active optics includes equipment that manipulates the overall massive optical assembly of the telescope to point the telescope, track

objects, or aligns the segments of the primary mirror. Adaptive optics, however, refers specifically to the manipulation of the optical wavefront for the purpose of image enhancement or correction. Joined together active and adaptive optics track objects across the sky and correct for atmospheric conditions or other aberrating effects dynamically and simultaneously.

AO is composed of three critical components: a deformable mirror, a control computer, and a wavefront sensor (Figure 9). Their design is based upon the desired telescope resolution and the environment, which dictate the extent and condition of uncompensated (pre-adaptive optics) distortion and ultimately limit the maximum resolution. The resolution is also limited by the aperture size of the primary mirror.

Wavefront sensors determine changes in the wavefront by examining the wavefront slope (1<sup>st</sup> derivative) or curvature (2<sup>nd</sup> derivative) and break the incoming wavefront into sub-apertures. Each sub-aperture corresponds to a channel that must be sensed and controlled by the AO system and control computer as part of a closed-loop system. This requires specialized digital signal processing units to handle large aperture telescopes such as those at the Keck observatory with more than 1000 channels.

Deformable mirrors use actuators to manipulate the wavefront by pushing or pulling on the mirror surface. The actuators may be either force-based actuators, which are typically electromechanical or hydraulic, or they may be displacement-based, such as piezoelectric or magnetostatic actuators [11]. The choice of actuator is application dependent; it also is related to the spectrum and environment in which the telescope is intended to operate.

There are two types of deformable mirrors: segmented and continuous facesheet. Segmented mirrors (Figure 10a) use actuators to maintain the relative

position of each segment of the complete reflector (mirror, reflector, and facesheet are interchangeable terms). Additionally, actuators may also be used to maintain the individual figure of each segment. In the continuous facesheet case (Figure 10b) actuators are used to position the mirror properly and maintain the figure of the entire mirror surface.

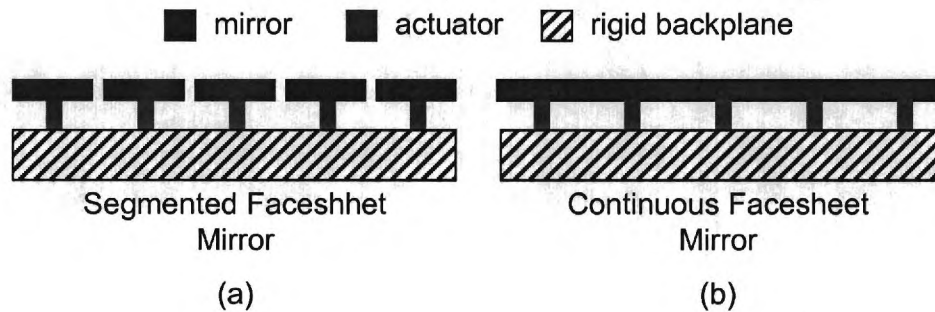


Figure 10. (a) Segmented and (b) Continuous Facesheet

Segmented mirrors have the advantage of isolating negative coupling effects between actuated regions of the mirror. Segmented primary mirrors also benefit from increases in manufacturability and decreases in weight. It is not uncommon for multiple deformable mirrors to exist within the optical train of a telescope. A telescope may employ adaptive optics in its secondary or tertiary mirrors, and often one mirror is devoted entirely to the removal of lower order aberrations. These aberrations include tilt (which is the most prevalent aberration) and piston. An example of a stand alone tilt mirror is shown in Figure 9.

Active optics plays a huge part in the design of the JWST primary mirror. The design specifies that each mirror segment possess four actuators to maintain relative position. The overall semi-rigidity of the mirror is relied upon to maintain figure. Control over the relative position and figure of each segment is of particular concern

as final adjustments to align the mirror segments and compensate for thermal loads in space, must take place upon deployment. No adaptive optics in the sense described above are utilized in the design of the JWST.

### **1.3 Summary and Objective**

Terrestrial telescopes do not have the same weight requirements as space-based telescopes. Furthermore, the same innovations in terrestrial designs are not adequate for space-based optics. Thus a new technology that is lighter in weight than current technology, but no less effective, is required. This study represents work at the Georgia Institute of Technology in modelling a hexagonal thin-shell deformation mirror with an adaptive truss. It is advanced that the solution lies in high strength to weight ratio materials and a novel adaptive truss for adaptive optics correction of the primary mirror.

This thesis specifically examines the feasibility of surface parallel actuation (SPA) of a thin-shell CuZr deformable mirror as an alternative to a typical surface normal actuation (SNA) based mirror. In SPA actuators are mounted parallel (rather than normal) to a mirror or *facesheet* as part of an adaptive truss or *substrate*. The substrate controls the shape of the facesheet and supports it. The combination of the facesheet and substrate is collectively referred to as a deformable mirror (DM). It is believed that by using a thin-shell mirror (100  $\mu\text{m}$  or less in thickness) with a light weight substrate that a significant weight-savings will occur, thus enabling larger space-based telescopes.

Since, an SPA DM is a recently patented concept neither experimental data nor a baseline design exists. Subsequently, this thesis advances the SPA DM concept by

- 1) creating a representative model,

- 2) developing design evaluation methods and establishing basic feasibility and design criteria by comparing the SPA DM to existing SNA DM technology,
- 3) evaluating the FEA simulated response of the DM over Zernike error modes,
- 4) evaluating the FEA simulated response to select thermal loads, and
- 5) evaluating the ability of the DM to remove thermal error, and the forces required to do so.

Feasibility criteria such as acceptable levels of uncorrected aberration, the spectrum of operation, force levels, and number of actuators are inferred from a few stated requirements and component specifications, such as the error budget of the primary mirror and actuator force and stroke limitations. Finally, this thesis concludes that overall the SPA DM concept is feasible.

#### **1.4 Major Contributions**

This thesis contributes a comprehensive structural-thermal finite element model that determines the corrective ability and shows the feasibility of a thin-shell surface parallel actuated deformable mirror. Evaluations performed for varying numbers of control points, facesheet thicknesses, geometric and material parameters, errors modes and thermal loads were reduced to four primary metrics of evaluation: peak to valley displacement, RMS error, and actuator force and stroke levels. Using representative thermal loads, conclusions were drawn regarding the thermal response of the facesheet and rigidifying (“stiffening”) affects of additional actuators. A method was developed to confirm the linearity of the SPA DM through a comparison of aberration reproduction and correction. Small glitches were designed into the FEM model, to evaluate the sensitivity of the results to errors in the actuator position. Finally,

feasibility criteria was developed using the existing technology (surface normal actuation), an assumed spectrum of operation (visible to near-infrared light), and the proposed piezoelectric actuators.

In support of the analyses and conclusions an ANSYS script library and MATLAB support tools were developed that:

1. Generate the geometry and parameterization of the deformable mirror
2. Generate the thermal analysis of the facesheet and substrate
3. Determine the influence coefficients of each mirror configuration
4. Control the data storage and processing
5. Generate Zernike polynomials and Least Square Fit
6. Automate the analysis and provide a Graphical User Interface

In summary, tools were developed, analyses performed, and relevant conclusions drawn, such that the feasibility of the SPA DM is uniquely and explicitly justified in this thesis. Specifically, not included as contributions are the MATLAB based truss tessellation algorithm, optimized least squares fit which were developed by Dr. Harvey Lipkin. Also excluded is the recently issued patent upon which this research is based.

## CHAPTER 2

### INITIAL MODEL DEVELOPMENT

#### 2.1 Initial Model Development

SNA is the current prevailing adaptive optics technology (Figure 11). It uses actuators mounted to a heavy rigid backplane to push or pull on a facesheet creating a deformable mirror. The backplane contributes to the high aerial density of the structure. Structures with a high aerial density do not scale well in either terrestrial or space-based applications.

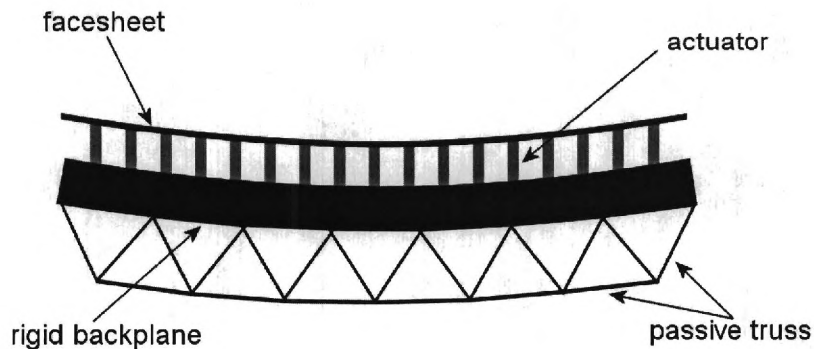


Figure 11. Surface Normal Actuation.

As terrestrial observatories grow in size, they require more structural reinforcement and more active or adaptive components. This is unacceptable in space-based telescopes as no economical way exists to transport high aerial density structures into space. This research investigates the feasibility of replacing the heavy rigid backplane and relatively thick mirror with a thin-shell or membrane like mirror (100  $\mu\text{m}$  or less in thickness) attached to a lightweight truss with embedded actuators.

Due to the approximate orientation of the actuators this approach is collectively referred to as Surface Parallel Actuation (SPA) (Figure 12).

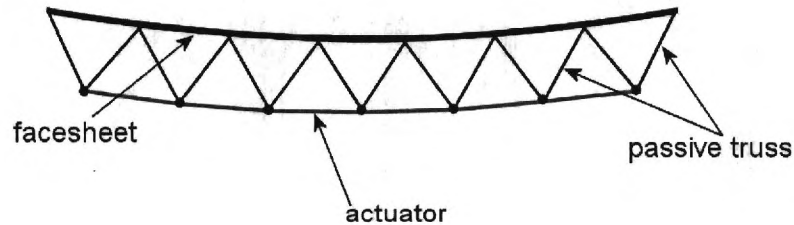


Figure 12. Surface Parallel Actuation.

In Figure 12 the connections to the facesheet are flexure joints. The facesheet (mirror) and actuators are separated by struts. As an actuator extends or contracts the truss (also referred to as *substrate*) exerts forces normal and tangential to the mirror surface causing the facesheet to flex.

A 2D beam analysis was conducted to understand how SNA and SPA reshape the facesheet. Specifically, each substrate was studied in terms of its ability to form polynomial and sinusoidal profiles, which showed that the influence of a single actuator is highly localized for SNA while for SPA it is spread throughout the facesheet.

For the SNA substrate Figure 13a shows half a beam section with the fifth actuator from the right extended (circled in red). Other than minor deflections across adjacent spans the actuator has a limited effect beyond the two adjacent spans. However, the analogous surface parallel actuator (fifth from the right, also circled in red) significantly affects the six spans to the left of it (Figure 13b). The way each actuator affects the facesheet is referred to as the *influence function* of that actuator.

Plots of the influence functions are shown for the entire mirror section below each of the half mirror sections in Figure 13a and b. Figure 13a shows SNA deflecting the surface to 0.050 mm (50  $\mu\text{m}$ ), and SPA deflecting the surface to 0.4 mm (400  $\mu\text{m}$ ). This illustrates that each actuator configuration controls the facesheet differently.

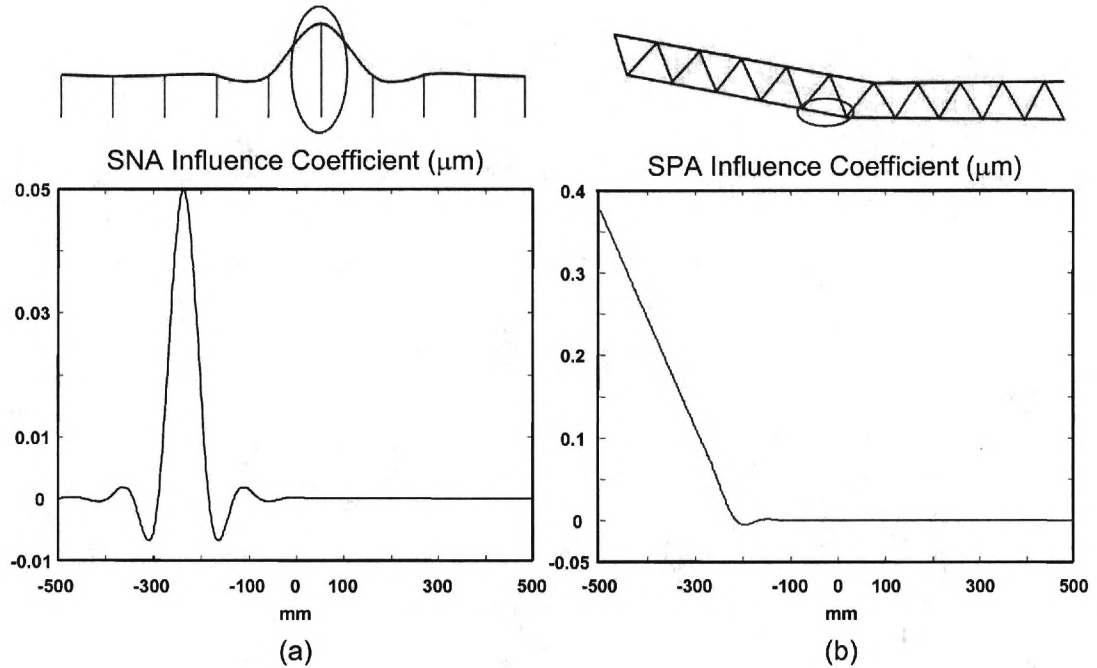


Figure 13. (a) 2D Surface Normal and (b) Surface Parallel Influence Coefficients.

Additional, SNA inherently corrects for three rigid body displacement modes, while SPA requires a tripod. These modes, known as tip, tilt, and piston, are a rotation about the  $x$  and  $y$  axes and translation along the optical ( $z$ ) axis of the mirror, as seen in Figure 14).

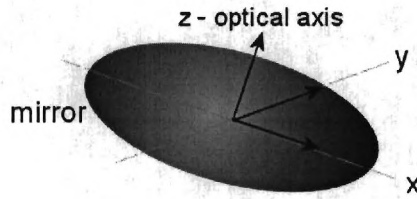


Figure 14. Global Coordinate System of Mirror.

## 2.2 Three Dimensional Modelling

The 3D SPA model, is based on the patterning of the 2D SPA design and is illustrated in Figure 15. Actuator nodes (red) are uniformly offset from the facesheet and follow its radius of curvature (a flat facesheet is depicted in Figure 15). The actuators (red bars) are tangent to the surface and struts (black) connect actuators to evenly spaced mirror nodes (blue). All struts are the same length and each actuator node connects to six struts.

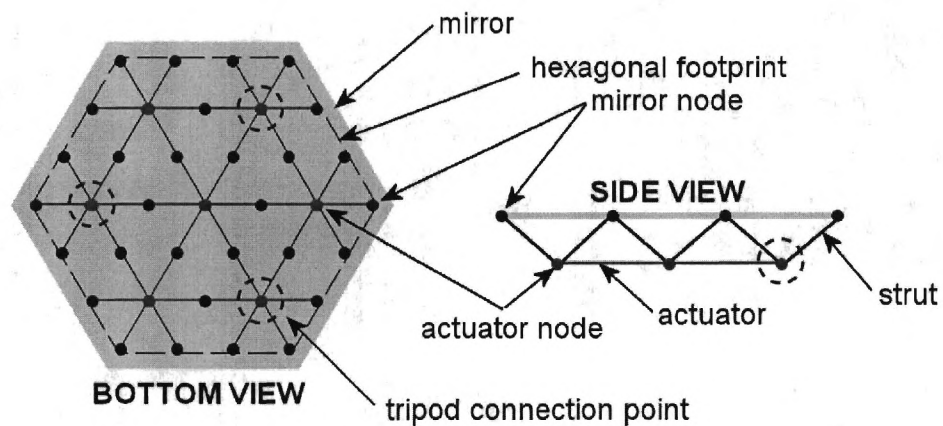


Figure 15. 3D SPA Hexagonal Truss Layout.

The outermost mirror nodes outline the hexagonal footprint of the substrate, which is adjusted to span 98% of facesheet. This ensures that the substrate fits within the facesheet and limits edge effects. Three bipedal tripod legs connect the substrate to ground via there actuator nodes, as shown in Figure 15, Figure 16, and Figure 17 (which shows a 3D perspective view). Figure 18 shows a cut-away view of the substrate and Figure 19 shows how the two bipods of each tripod leg are constrained to operate as a single actuator.

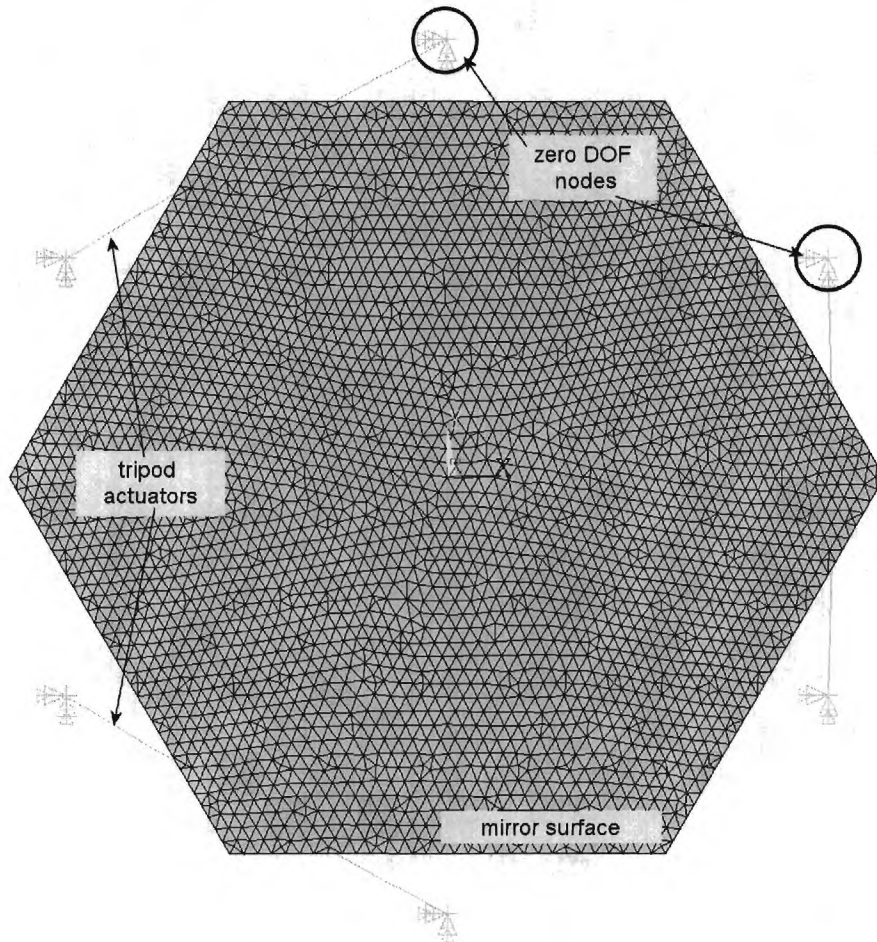


Figure 16. SPA Deformation Mirror Model.

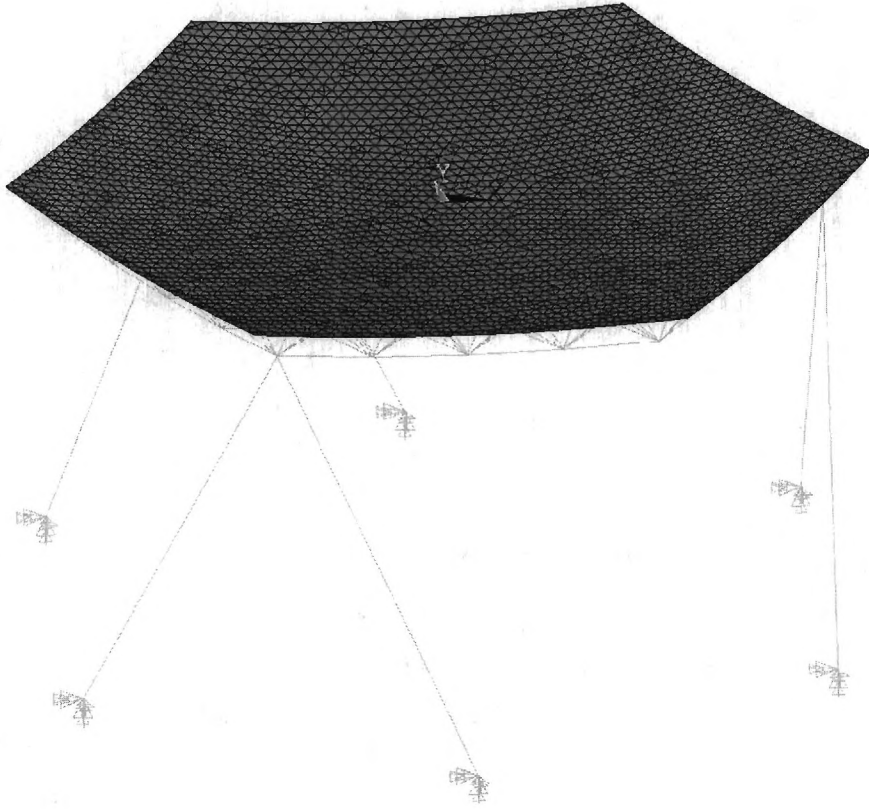


Figure 17: 3D Perspective View of SPA Deformable Mirror

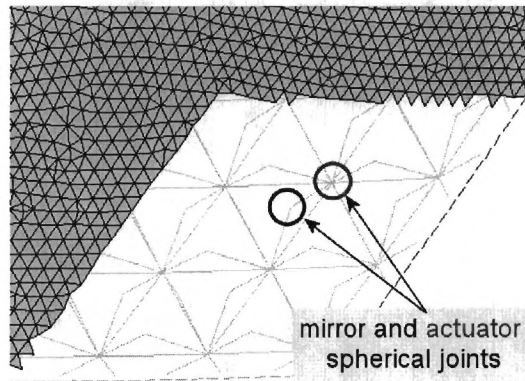


Figure 18. Facesheet Section/Cut Away with Exposed Substrate

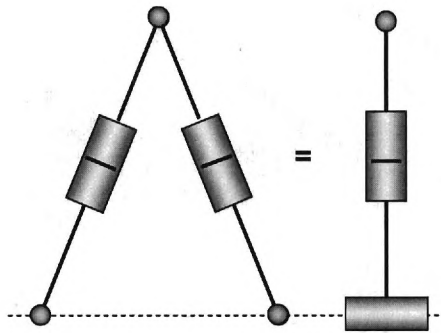


Figure 19. Bipedal Tripod Leg and Equivalent Single Actuator.

Figure 20 shows a SNA version of the same fifteen-actuator (12 truss and 3 tripod actuators) deformable mirror shown in Figure 15, again there is one SNA actuator used per a SPA actuator. This is illustrated in the side view of Figure 20 and in Figure 21a and b, where it is shown that each SNA actuator straddles the center point of a corresponding SPA actuator (Figure 21b).

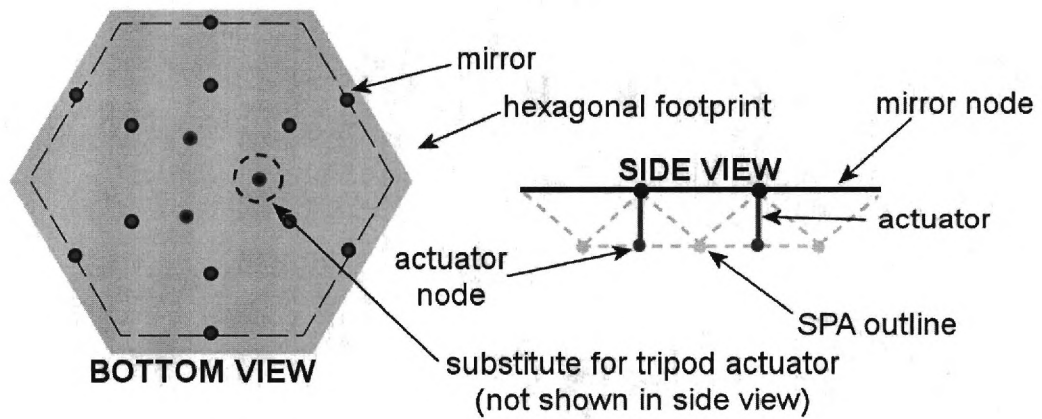


Figure 20. 3D SNA Hexagonal Truss Layout.

Three actuators are positioned near the center of the mirror to account for the bipedal tripod legs of the SPA case (circled and inverted, blue on red, in Figure 20).

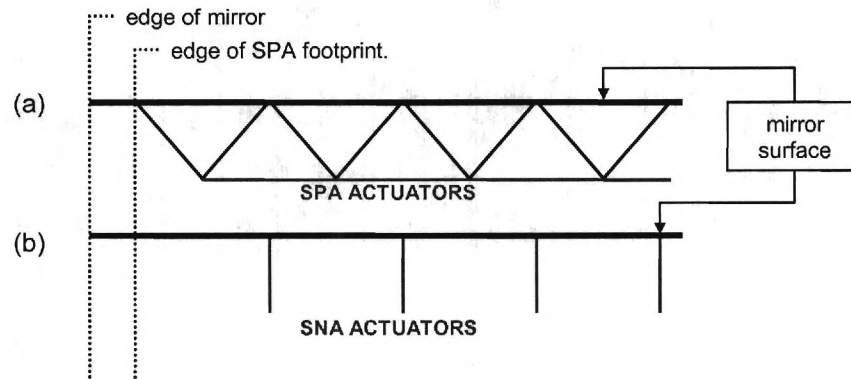


Figure 21. (a) Standard SPA Footprint, (b) Standard SNA Footprint.

### 2.3 FEM Model Development

The ANSYS FEM model is constructed from a series of imported MATLAB data files that store the configuration of the deformable mirror. MATLAB generates the layout of the hexagonal substrate and stores it in a dimensionless rectangular format. One data file contains the node locations for the facesheet, struts, and actuators, while a second data file stores the connectivity of these elements to the nodes. A third file stores the number of elements and nodes, and several other files store user controlled parameters.

The model is generally parametric and the truss configuration is specified by the number actuators along the longest truss line and fit proportionally to the specified aperture and figure. The mirror figure is spherically curved (Figure 22 **Error! Reference source not found.**) and is controlled by the figure number,  $f$ , which gives the radius of curvature as

$$r_c = 2f \left( \frac{a}{2} \right) \quad (1)$$

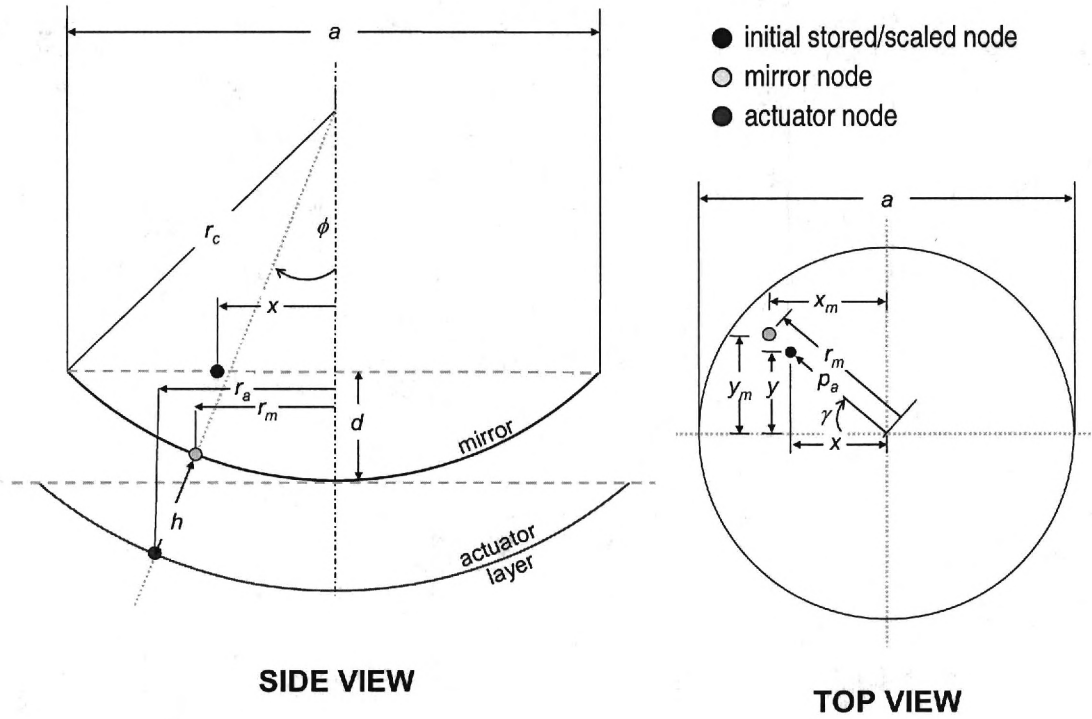


Figure 22. Geometric Setup of the SPA Deformable Mirror

Beyond  $f$  only a few basic parameters are necessary to control the configuration (thickness, truss-height, number of actuators, etc.) of the deformable mirror. The facesheet is defined first by revolving an arc about the  $x$ -axis into a sphere. Next two hexagonal prisms as shown in Figure 23 encompass the unwanted portion of the sphere and subtract it away; the extra top surface is deleted leaving the hexagonal thin-shell shown in Figure 19.

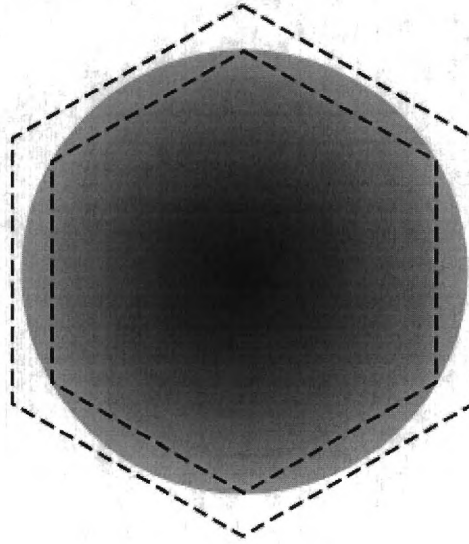


Figure 23: Illustration of Hexagonal Prisms and Sphere (Top View)

Since the substrate is stored as dimensionless rectangular data it must be rescaled to its hexagonal form and then scaled to fit the selected mirror aperture. The code calculates an overall truss scaling factor and applies a hexagonal adjustment factor of  $\tan(\pi/3)$  in the  $y$ -direction. Figure 22 **Error! Reference source not found.** shows evenly spaced scaled nodal locations (blue) that must be transferred to the mirror (light blue) and actuator layer (red) with a similar equal spacing.

The blue node (level with the rim of the facesheet) is the initial placement of the node based upon the scaled rectangular coordinate value. The parameters necessary to determine the location of a mirror (facesheet) node or actuator node are indicated in **Error! Reference source not found.**. The following geometric parameters determine the locations of the nodes:

- 1) The half cone angle  $\phi$ ,
- 2) The distance from center of the mirror to the rim vertically along the optical axis,  $d$ ,
- 3) The radial of curve of the “actuator layer”,  $(r_c+h)$ .

If  $h$  is the distance of the actuator layer from the facesheet (mirror), and is defined as some percentage,  $p_d$ , of  $d$ ,  $r_c$  is the radius of curvature of the facesheet and  $a$  is the aperture, then  $d$  and  $h$  are defined in equations (2) and (3) as:

$$d = r_c - \text{sqrt}\left(r_c^2 - \left(\frac{a}{2}\right)^2\right) \quad (2)$$

$$h = (p_d)d \quad (3)$$

**Error! Reference source not found.** shows  $x$ ,  $y$ , and  $p_a$  the initial scaled coordinates and radial distance from the optical axis of each node. Next the figure shows  $x_m$ ,  $y_m$ , and  $r_m$  the mirror coordinates and radial distance from the optical axis of the facesheet. **Error! Reference source not found.** also defines  $r_a$  the radial distance of an actuator and is accompanied by a corresponding  $x_a$  and  $y_a$  (both not shown) defining the location of an actuator node. Lastly, the figure defines an angle,  $\gamma$  which locates  $x_m$  and  $y_m$  (or  $x_a$  or  $y_a$ ) relative to  $r_m$  (or  $r_a$ ). Note that the  $z$  and  $z_m$ ,  $z_a$  coordinates, all along the optical axis, are not shown for clarity but are calculated below.

To transfer the nodal locations to the mirror and actuator layer, the cone angle,  $\phi$ , is calculate using a fraction of half the aperture,  $f_h$ , where

$p_a = \sqrt{(x^2 + y^2)}$ $f_h = \left(\frac{2p_a}{a}\right)$	(4)
--	-----

and then, the angle  $\phi$  is calculated as the full cone angle of the mirror multiplied by  $f_h$ .

$\phi = f_h \left( \sin^{-1} \left( \frac{r_c}{2a} \right) \right)$	(5)
---	-----

Finally the angle,  $\gamma$  (**Error! Reference source not found.** TOP VIEW) is determined as  $\tan^{-1}(y/x)$ .

From equation (5),  $\phi$ , is used to determine  $r_m$  (TOPVIEW), and subsequently  $x_m$  and  $y_m$  are calculated as shown in equations (6)-(8):

$$r_m = r_c \sin(\phi) \quad (6)$$

$$x_m = r_m \cos(\gamma) \quad (7)$$

$$y_m = r_m \sin(\gamma) \quad (8)$$

$z_m$  which is not shown in **Error! Reference source not found.**, is the z-coordinate of the new mirror node, and is calculated as:

$$z_m = r_c (1 - \cos(\phi)) \quad (9)$$

Mirror nodes are initially created as hard-points, which force the free-mesh routine to include them as nodes, thus guaranteeing a precise truss to mirror connection point. The actuator nodes are created similarly to the mirror nodes, where  $r_a$  is used as the distance from the optical axis. Recalling that  $h$  is the distance the truss drops down from the facesheet and  $r_c$  the radius of curvature, the location of actuator nodes is then determined per equations (10) - (13).

$$r_a = (r_c + h) \sin(\phi) \quad (10)$$

$$x_a = r_a \cos(\gamma) \quad (11)$$

$$y_a = r_a \sin(\gamma) \quad (12)$$

$$z_a = (r_c - (h)(1 - \cos(\phi))) \quad (13)$$

As a matter of convenience, actuator nodes are placed as key-points and then converted individually to nodes.

The facesheet is meshed with linear triangular elements because low stress gradients are expected [12] and they produce a mesh consistent with the hexagonal geometry. The element size is controlled by the element boundary length which is associated with the areas (or surfaces) that comprise the facesheet. Boundary length is very small when compared to the over all feature size (half-aperture of the mirror) and finicky as the ANSYS free-mesh routine often struggles to incorporate the explicitly defined nodes. Thus, the boundary length is adjusted to facilitate a free-mesh around the hard-points, rather than convergence. Subsequently, the strut and actuator elements are inserted into the FEM model. Since, actuator elements do not have a thermal component, during a thermal analysis they are replaced with a structurally equivalent strut element.

Each tripod leg is placed an integer number of segments along a major diagonal, relative to the optical axis. This is specified in terms of a percentage and is shifted to the nearest node. The design of the tripod provides for the correction of tip, tilt, and piston modes of aberration (3 DOF). In the case of a thermal analysis tripod actuators are also replaced with a structurally equivalent strut.

FEM analyses were performed using ANSYS Versions 6.1-7.2.

Table 1 summarizes the element types used in this study.

Table 1. ANSYS Element Type Descriptions.

FEA - Model Elements					
ANSYS Structural Name	Structural DOF	Thermal DOF	Related Thermal Element	Possible Element Types	Model Component
LINK8	UX, UY, UZ	None	Link 33	3D SPAR	Struts
LINK11	UX, UY, UZ	None	Link 33*	3D SPAR	Actuator
SHELL63	UX, UY, UZ, ROTX, ROTY, ROTZ	None	Shell 57	linear triangular and quadrilateral	Mirror
SHELL93	UX, UY, UZ, ROTX, ROTY, ROTZ	None	None	quadratic triangular or quadrilateral	Mirror

\* LINK11 must be manually changed to LINK8 to facilitate conversion to LINK33.

After meshing is complete a routine allocates an approximately rectangular grid of data points to the facesheet, these points are associated with the closest nodes, and used to sample deflection values.

The deformable mirror was constructed from a series of SPARS (members that handle only axial loads) for the struts and actuators and linear and/or quadratic shell elements for the facesheet. Each structural element has a corresponding ANSYS thermal element. A special ANSYS mechanical actuator (Figure 24) was used to simulate the substrate and tripod actuators. The element is capable of operating based upon a force or a displacement input. This study uses the displacement input and for some evaluations monitors the force output of the actuator. The element requires a stiffness  $k$ . The damping coefficient is not used in these simulations.

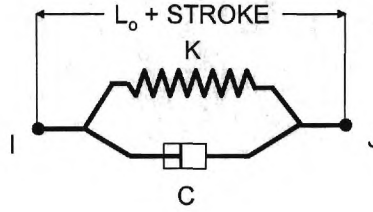


Figure 24. ANSYS Actuator Element (LINK 11)

No intermediate connecting elements exist between struts, actuator, or mirror elements as described. Linear elements are used in the final analysis of the model. Though quadratic elements are generally more accurate, linear elements for the case of the simple curved, nearly flat mirror yield the best accuracy when one considers the required computational effort.

#### **2.4 Material Properties and Relevant Dimensioning**

Key material characteristics of this deformable mirror are the overall rigidity and coefficients of thermal expansion for the facesheet, struts, and actuators. Significant changes in performance of the deformable mirror occur based upon the rigidity of the facesheet and substrate (struts and actuators). For the purpose of this study, the struts are made inflexible using a modulus of elasticity of approximately 70 GPa, which is similar to aluminium.

Thermal properties are significant in that the ideal deformable mirror would have a uniform CTE throughout to minimize distortions. However, this is not the case and each sub-component (mirror, actuator, and struts) is assigned a CTE value. No other significant material properties were considered over the course of this study. Table 12 in Appendix A contains a complete list of material properties.

The strut and shell elements must have a cross-sectional area and thickness defined respectively. The diameter of the strut element is set to 1.16 mm, in

accordance with work performed in [12]. The nominal thickness of the facesheet used is either 1000  $\mu\text{m}$  (Chapter 4 and Chapter 5) or 100  $\mu\text{m}$  (Chapter 6), where the latter is in the thickness range of a CuZr laminate prototype mirror and the former was an arbitrary starting point prior to the prototype specification.

Modelling details such as baseline parameters and method are discussed in the next chapter, and thermal modelling details are discussed in Chapter 5.

## CHAPTER 3

### EVALUATION AND COMPUTATIONAL METHOD

This chapter discusses the tools and metrics used in the evaluation of the SPA deformable mirror. Section 3.1 describes the graphic user interface and modelling coordination tool built in MATLAB. Section 3.2 discusses Zernike polynomials as representative modes of optical wavefront and facesheet aberration. Section 3.3 discusses the effect of each actuator on the facesheet in terms of its influence coefficients. A discussion of the least squares used to shape the facesheet follows in Section 3.4, the primary metric of evaluation, RMS error, is explained in Section 3.5, and in Section 3.6 the optical requirements are defined in terms of a fraction of the shortest wavelength of light upon which the deformable mirror might operate.

#### **3.1 Introduction**

The MATLAB SPA Truss Analysis Setup Toolbox (STAS) generates data files that are necessary to construct the SPA and SNA FEM models. STAS also controls and organizes each analysis through the graphic user interface shown in Figure 25.

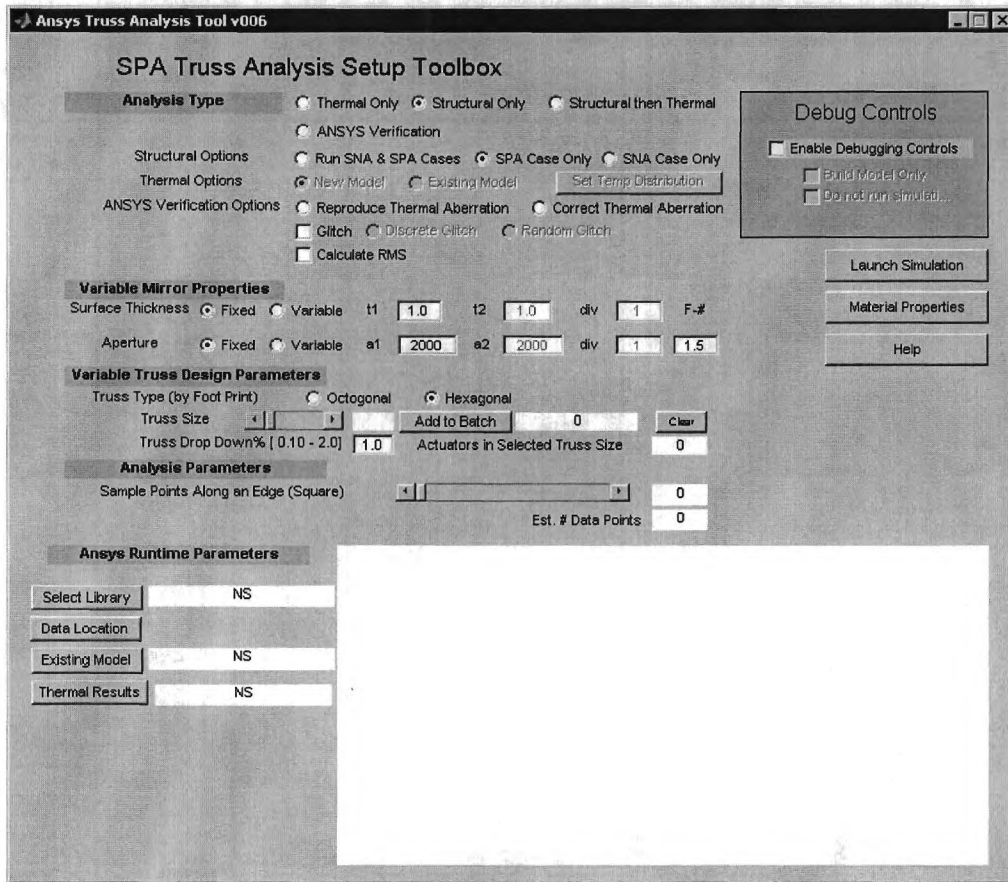


Figure 25. MATLAB GUI (STAS).

The STAS GUI supplies physical and runtime parameters such as: aperture, thickness,  $f$ -number, footprint type (only a hexagonal footprint is presented), truss size (controls the number of actuators), “truss height” (or drop down) as a percentage of the mirror depth, number of facesheet sample points, use of a pre-existing thermal profile or structural model, material properties, and thermal loads. Other relevant parameters must be varied from within the ANSYS APL script library.

The functionality of the combined MATLAB and ANSYS procedures are separated roughly into seven modules, which are summarized in the process flow diagram shown in Figure 26.

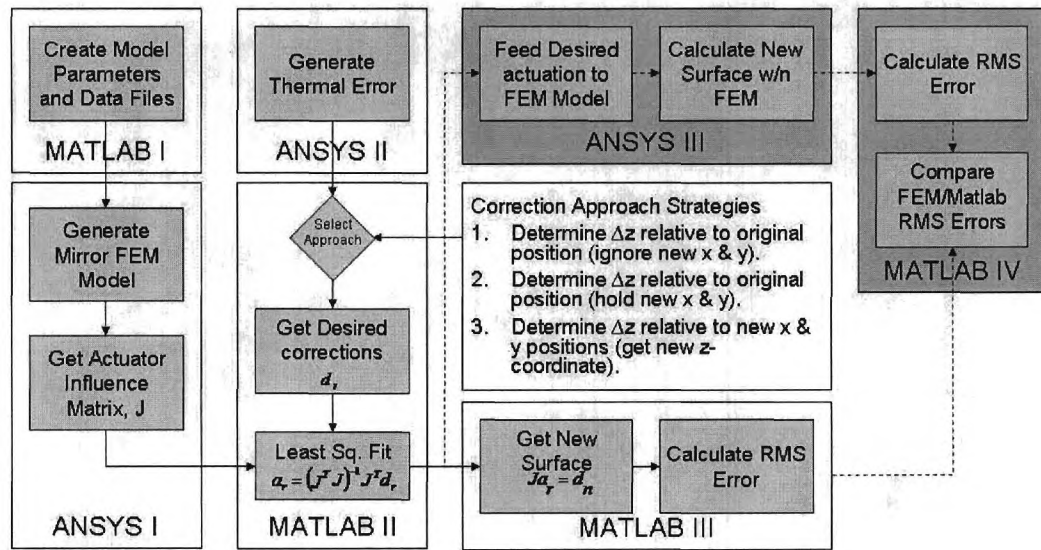


Figure 26. Evaluation, Methodology, and Process Flow.

The first block labelled MATLAB I creates the data files necessary for building a structural model. This includes node locations, element types and connectivity, as well as, simulation parameters, and a script control file. The following block labelled ANSYS I generates the structural models and solves for the influence coefficients of each actuator. This matrix of influence coefficient data is passed to MATLAB Block II (discussed in Section 3.3).

The routines in MATLAB Block II and ANSYS Block II produced error in terms of Zernike error modes or actual thermal aberrations, and determine the actuator strokes required either to correct or mimic an aberration (the latter is used for evaluation purposes only). MATLAB Block III deflects the facesheet using actuator strokes determined in MATLAB Block II. The resulting deflection is compared to a reference shape and a root mean squared (RMS) error is calculated. Alternatively the actuator strokes can be fed back into ANSYS Block III to simulate the reaction of the

facesheet and compare it to the desired shape. MATLAB Block IV optionally compares MATLAB and ANSYS results.

### 3.2 Zernike Polynomials and Approximation of the OPD

A Zernike series represents optical wavefront aberrations over a circular region in the same manner as a Fourier series representation of a periodic function. It can also represent the physical aberration of a mirror or optical lens.

Each series is composed of orthogonal Zernike polynomials which are defined in terms of cylindrical coordinates,  $r$  and  $\theta$  [11, 13]. They consist of a sinusoidal component varying with angle  $\theta$  about the  $z$ -axis of a cylindrical coordinate system and a polynomial component varying in the radial direction. An aberration is expressed as a linear combination of Zernike polynomials. Equations (17)-(19) define a single Zernike polynomial  $Z_p^q$ , where  $q$  is the radial order and  $p$  is the azimuthally order of the polynomial. Figure 27 shows plots of the first six polynomials. The first three are the rigid body displacements of piston, tip, and tilt. The remaining three referred to as astigmatism x, power, and astigmatism y.

$$Z_p^q = R_p^q(r, \theta) * W^q(\theta) \quad (14)$$

$$R_p^q(r, \theta) = \sum_{s=0}^{\frac{(p-q)}{2}} (-1)^s \frac{(p-s)!}{s! \left(\frac{p+q}{2} - s\right)! \left(\frac{p-q}{2} - s\right)!} (r)^{(p-2s)} \quad (15)$$

$$W^q(\theta) = \begin{cases} \cos(\theta) & q < 0 \\ \sin(\theta) & q > 0 \\ 1 & q = 0 \end{cases} \quad (16)$$

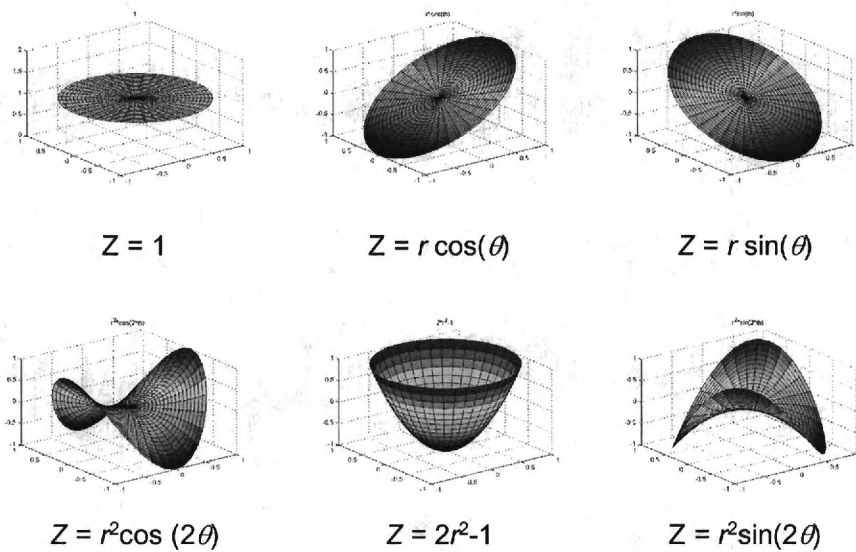


Figure 27. First 6 Zernike Polynomials.

In a stricter sense, a Zernike series describes the aberration of the wavefront in terms of optical path differences (OPD) over a flat disk like region. In terms of a single ray of light, OPD describes the phase variation due to an aberration with respect to a reference wavefront. In this study the reference wavefront is spherical, which is the same as the unaberrated figure of the facesheet.

This study assumes that for small  $f$ -numbers (virtually flat mirrors found in telescopes) the facesheet deforms parallel to the optical axis and is given by the usual approximation of one half the OPD.

### 3.3 Actuator Influence Coefficients

The effect of each actuator on the facesheet is to create a single column of influence coefficients, which is gathered by sampling at distinct points at the beginning of each analysis by individually moving each actuator through a nominal displacement. Each column of influence coefficients is aggregated into a *matrix of influence coefficients*

defined as the *Jacobian*  $J$ . It is structure as an  $n$  data points by  $m$  actuators by  $p$  deep matrix. The dimension  $p$  indexes the  $x$ ,  $y$ , and  $z$  displacements of each data point, due to each nominal actuator displacement.  $J$  is further discussed again in Section 3.4. Ultimately, adjustments are made to the facesheet by moving actuators such that their collective movement best achieves the desired shape of the facesheet, based upon the influence coefficients.

Figure 28 graphically illustrates a typical highly localized deflection profile of a 3D SNA influence coefficient for a single actuator. Notice that the effects of coupling are limited to the immediately surround surface.

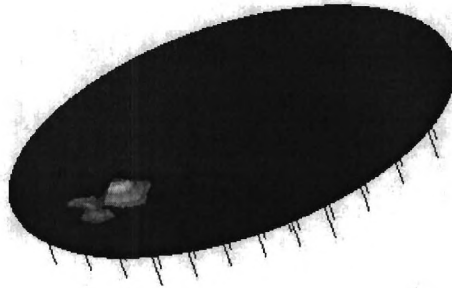


Figure 28. 3D SNA Influence Coefficient Example.

Figure 29 represents a typical SPA influence coefficient, where the actuator is located towards the center of the mirror and the effect spans the entire facesheet. Despite the coupled nature of the SPA DM, the assumption is made that the influence coefficients remain constant for small aberrations and the deformable mirror operates linearly.

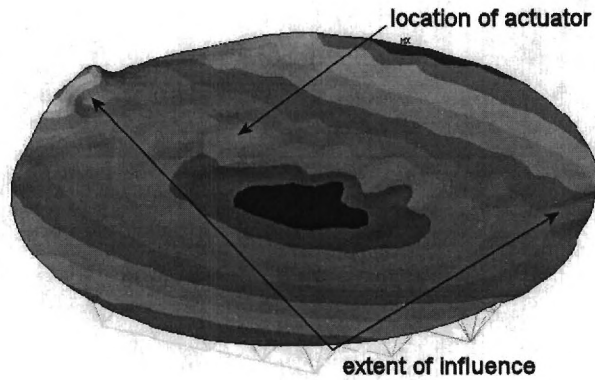


Figure 29. 3D SPA Influence Coefficient Example.

### **3.4 Determining the Actuators Strokes: Least Squares Fit of Influence Coefficient Data**

For any continuous surface described in terms of discrete sample points, operations on that surface are an approximation, unless an exact analytical solution exists. Since the influence of each actuator is discretely specified in terms of an  $m$  by  $n$  by  $p$  matrix, manipulation of the surface must be performed using the “best” actuator strokes. A least squares fit is the approximating method used to determine the actuator strokes that most accurately adjust the facesheet to the desired shape.

Though the method chosen here is the simplest, there are three possible approaches to shaping the mirror via a least squares fit, as illustrated in Figure 30.

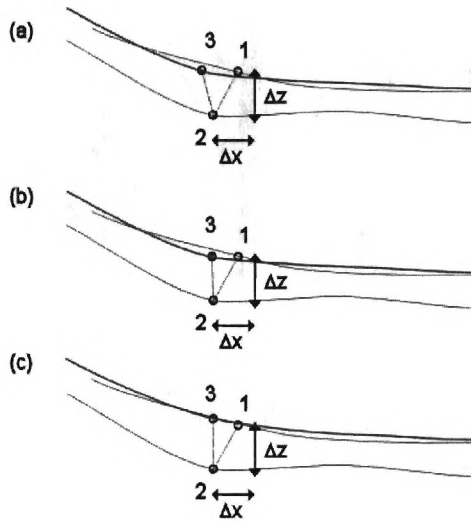


Figure 30. Three Aberration Correction Approaches.

Figure 30a shows the basic three steps by which the facesheet is displaced from its original shape and then adjusted. Point 1 is located on the original surface and is aberrated to point 2 by some  $\Delta x$ ,  $\Delta y$ , and  $\Delta z$  ( $\Delta y$  is not shown). In an effort to correct the facesheet, point 2 becomes point 3 after applying the actuator strokes calculated using a least squares fit. In this case the  $x$  and  $y$  displacement is not considered, and the facesheet is corrected only in the  $z$ -direction.

In Figure 30b point 1 is aberrated to point 2 again. The primary difference is that the new  $x$  and  $y$  position are held, however, the surface is still adjusted to compensate for the  $z$  displacement relative to the original location.

Finally, in Figure 30c point 1 is again aberrated to point 2, however, the new  $x$  and  $y$  position is held and used to determine the new  $z$  location relative to its new  $x$  and  $y$  position.

There are at least two advantages that method (b) or (c) might yield: (1) greater accuracy and (2) some degree of stress relief. While these advantages could be

beneficial they are not critical to showing the feasibility of the SPA approach and thus the simple method (a) is used for this work, which only requires the  $z$  plane of the Jacobian yielding a  $m$  by  $n$  matrix  $J_z$ .

A least squares fit determines the best actuator strokes to shape the facesheet by minimizing the square of the error between the desired and actual  $z$  displacements of the facesheet. The error in the  $z$ -direction is related to the Jacobian, by equation (17):

$$E_z^2 = |J_z \bar{a} - d_z|^2 \quad (17)$$

where  $E_z$  is the error in the  $z$ -direction,  $\bar{a}$  is a column vector of required actuator strokes, and  $d_z$  is the desired surface position in the  $z$ -direction. Differentiating with respect to  $\bar{a}$  yields

$$\frac{d}{d\bar{a}} E_z^2(\bar{a}) = \frac{d}{d\bar{a}} ((J_z \bar{a})^T J_z \bar{a} - 2(J_z \bar{a})^T d_z - d_z^T d_z) \quad (18)$$

and setting it to equal zero gives

$$dE_z = J_z^T J_z \bar{a} - J_z^T d_z = 0 \quad (19)$$

thus yielding

$$\bar{a} = J_z^+ d_z = (J_z^T J_z)^{-1} J_z^T d_z \quad (20)$$

where  $J_z^+$  is the pseudoinverse of  $J_z$ . For explanatory purposes the vectors  $\bar{a}$  and  $d_z$ , as well  $J_z^+$ , can be expanded as:

$$\begin{bmatrix} a_1 \\ a_2 \\ \cdot \\ \cdot \\ \cdot \\ a_n \end{bmatrix} = \begin{bmatrix} j_{z11} & j_{z12} & \cdot & \cdot & \cdot & j_{z1n} \\ j_{z21} & & & & & \\ \cdot & & & & & \\ \cdot & & & & & \\ \cdot & & & & & \\ j_{zm1} & & \cdot & \cdot & \cdot & j_{zmn} \end{bmatrix}^+ \begin{bmatrix} d_{z1} \\ \cdot \\ \cdot \\ \cdot \\ d_{zm} \end{bmatrix}. \quad (21)$$

To create consistency across different numbers of actuators, actuation types, and aberrations the strokes of all actuators are proportionally scaled such that the maximum stroke is 50  $\mu\text{m}$ . The scaled actuator strokes create a new theoretical surface. Since the deformable mirror operates linearly the reference aberration is scaled by the same factor to make a comparison between it and the new surface.

### 3.5 Primary Metric of Evaluation: RMS Error

RMS error (or residual RMS error) is used in two senses throughout this study, absolute and normalized. Absolute RMS error,  $RMS_a$  is a physical measure of the error remaining in the corrected facesheet,

$$RMS_a = \sqrt{\frac{\sum_i^n (as_i - ds_i)^2}{n}} \quad (22)$$

where  $as_i$  is the actual (or actuated) surface displacement generated by the actuators and  $ds_i$  is the desired surface displacement. Index  $i$  represents the  $i^{\text{th}}$  sample point and  $n$  is the total number of sample points. Note the *term residual RMS error* refers specifically to the error remaining after the removal of an aberration. However, in this study RMS error refers to any deformation between a desired test shape and the shape formed by the deformable mirror.

Normalized RMS error,  $RMS_n$  is the absolute RMS error normalized by the RMS magnitude of the aberration, given in terms of a ratio or percentage,

$$RMS_n = \frac{\sqrt{\frac{\sum_i^n (as_i - ds_i)^2}{n}}}{\sqrt{\frac{\sum_i^n (es_i)^2}{n}}} = \sqrt{\frac{\sum_i^n (as_i - ds_i)^2}{\sum_i^n (es_i)^2}} \quad (23)$$

The term  $es_i$  is introduced as the magnitude of the aberration (error surface) at a given point. In cases of aberration reproduction  $es_i$  will equal  $ds_i$  so the error surface becomes the desired surface. Unless explicitly stated otherwise, RMS error or RMS refers to the normalized value.

### **3.6 Optical Requirements of the Deformable Mirror**

To evaluate the feasibility of this deformable mirror optical requirements are defined as a fraction of the shortest wavelength of light upon which the deformable mirror operates. This fraction of a wavelength corresponds to an error budget or RMS error within which the mirror surface must be positioned. For this study the specified level of performance is that the optical wavefront be corrected to within one tenth of the shortest wavelength over which the telescope might operate,  $\lambda_m$ . It is assumed that aberration of the facesheet is the sole cause of wavefront aberration and the wavefront itself is perfect.

As stated earlier, the mirror must operate at half the requirement applied to the wavefront (half the OPD). Thus if the wavefront must be correct to within one tenth of a wavelength, then the facesheet correction must be within  $1/20^{\text{th}}$  of a wavelength over the entire spectrum of operation.

For example, consider a telescope operating in the range of 800-5000 nm range (red to near-infrared), see Figure 31.

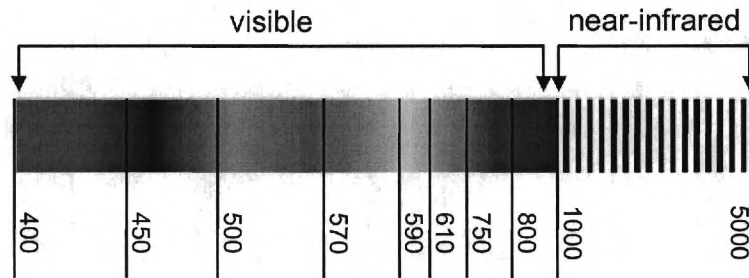


Figure 31. Electromagnetic Spectrum from 400-5000 nm.

For a  $1/10^{\text{th}}$  wavelength error budget the residual RMS wavefront error due to the deformable mirror must fall below 80 nm ( $800 \text{ nm} \times 1/10$ , where 800 nm the shortest wavelength of operation). The facesheet of the deformable mirror must then operate below 40 nm absolute RMS error ( $800 \text{ nm} \times 1/20$ ).

For example, consider a 900 nm RMS aberration of the wavefront corrected to a 10% RMS residual error giving an absolute error 90 nm RMS. Again we assume that in terms of facesheet deformation, deflections along the optical axis (z-axis) are approximately equal to one-half the wavefront error. To achieve a 10% correction the surface must be positioned to within 5% yielding a 45 nm absolute RMS. Though a significant amount of error has been removed, 45 nm is not nearly enough to allow observation over the entire spectrum seen in Figure 31. To allow observations over the entire spectrum the facesheet would be required to have a residual absolute RMS error of 20 nm ( $1/20^{\text{th}}$  of the lower end of the spectrum).

## CHAPTER 4

### DEVELOPMENT OF A BASELINE 3D MODEL

Feasibility of the SPA deformable mirror (DM) technology is established by comparing the ability of equivalent SPA and SNA cases to accurately form individual Zernike polynomials over a range of selected parameters: number of actuators, facesheet thickness, and truss height. The number of actuators affects the number of connections or *control points* attached to the facesheet. The facesheet thickness affects the rigidity of the deformable mirror. The truss height affects the forces applied to the facesheet by the substrate. Parameters not varied in the analysis are the *f*-number, aperture size, and tripod placement. This section closes with observations of print-through seen in each design.

#### **4.1 Introduction**

It is not necessary for the SPA design to outperform the SNA design, only that it perform well enough to meet similar requirements. The first sixty-six Zernike polynomials are used as representative error modes, and applied to a mirror with the baseline parameters specified in

Table 2. Looking at the observatories in Section 1.1, a reasonable segment ranges between 1.2 to 2.0 m in diameter. The thickness of 1000  $\mu\text{m}$  and actuator influence coefficient test stroke of 50  $\mu\text{m}$  (the stroke used to generate influence coefficients) are similar to those referenced in [12, 14]. The actuator quantity of 243, and the number of data points facilitated a reasonable simulation speed on a mid-grade PC. The  $f$ -number is a given project parameter designated for a spherical mirror.

Table 2. Baseline SPA and SNA Case Parameters.

Parameter	Value
Aperture	2.0 m
F-Number	1.5
Mirror Thickness	1000 $\mu\text{m}$
Data Points	9961
Number of Actuators	243
Influence Coefficient Actuator Test Stroke	50 $\mu\text{m}$

Feasibility is established using the following criteria:

1. An evaluation of the RMS error between the desired and actual Zernike modes produced by the SNA and SPA deformable mirrors.
2. The Peak to Valley deflection (P2V) achieved in forming a given Zernike polynomial, which can be interpreted as an output to input ratio.

For feasibility it is assumed that SPA RMS error and SPA P2V values do not fall an order of magnitude poor than those yielded by SNA. In evaluating these criteria the maximum actuator stroke is rescaled to 50  $\mu\text{m}$ , and the desired Zernike polynomial is rescaled for comparison purposes using the same scale factor required to rescale the actuator strokes. If the maximum actuator extension was 150  $\mu\text{m}$ , a scale factor of 1/3 would be applied to the actuator strokes ( $150 \mu\text{m} \times 1/3 = 50 \mu\text{m}$ ) and magnitude of the Zernike polynomial, thus making the desired and actuated surfaces comparable. The next section compares SNA and SPA using the first 66 Zernike modes.

## 4.2 Baseline Comparison: Zernike Modes

This section compares the abilities of SPA and SNA to shape the facesheet to each of the first sixty-six Zernike polynomials or *error modes*. For small deflections it is assumed that if the mode can be formed, then it can be removed from an aberrated facesheet by an equivalent reversal of the actuator strokes.

Figure 32 shows the RMS error in forming the first sixty-six Zernike modes and 243 actuators. The accuracy of SPA (blue) clearly exceeds SNA (red) for nearly the entire range.

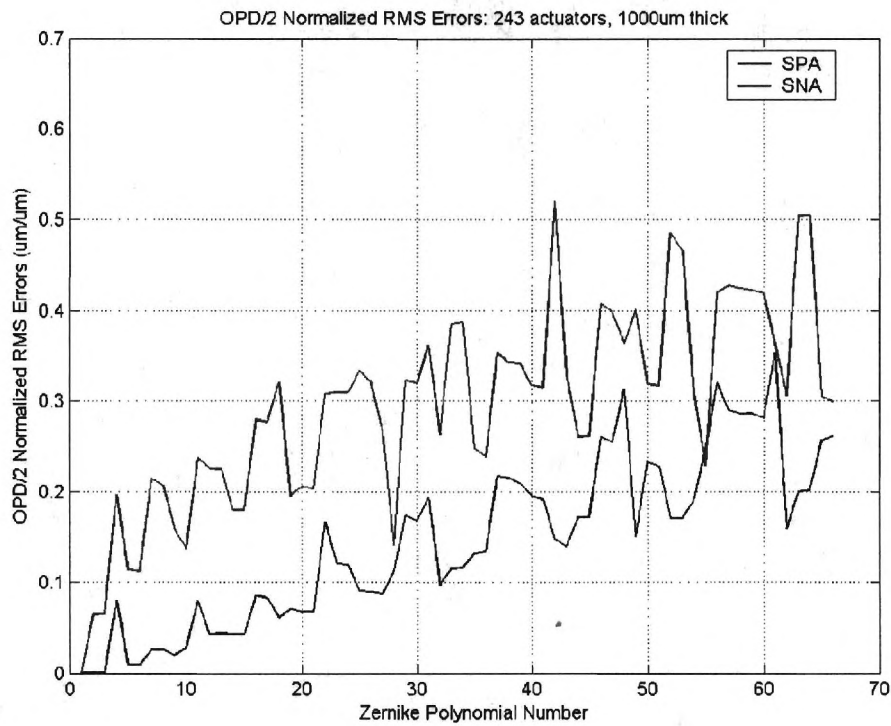


Figure 32. SNA vs. SPA Baseline Comparison for the First Sixty-Six Zernike Polynomials.

Figure 33 compares the percent error improvement of SPA over SNA in terms of RMS ( $RMS_{SPA}$  and  $RMS_{SNA}$  in Equation 11),

$$\% \text{ error improvement} = \frac{RMS_{SNA} - RMS_{SPA}}{RMS_{SNA}} \cdot 100\% \quad (24)$$

There is only one Zernike mode for which the SPA system does not show an improvement (mode 55).

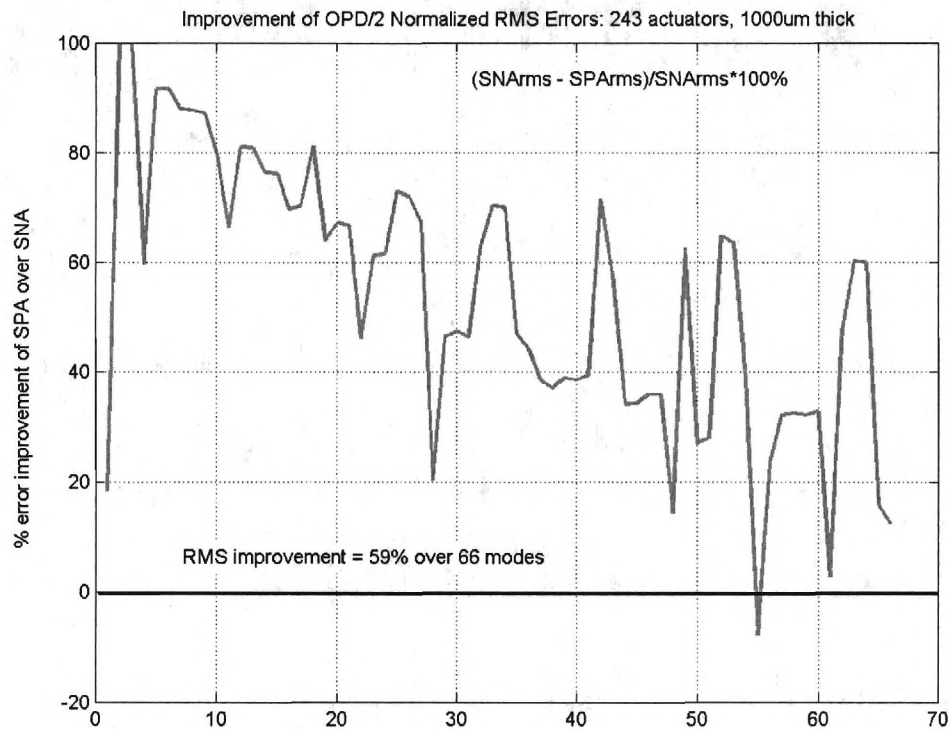


Figure 33. Percent Error Improvement of SPA over SNA for 243 Actuators.

Figure 34 compares the SPA and SNA P2V and in Figure 35 they are presented as a ratio. The P2V characterizes the bounds or overall magnitude of the deformation and because of the scaled actuator strokes is easily compared from mode to mode and between designs. Generally, SPA has greater amplitude for modes less

than 20, and SNA has greater amplitude for modes greater than 20. Mode 10 shows an unusually high value for SPA, this is further examined in Section 4.4.

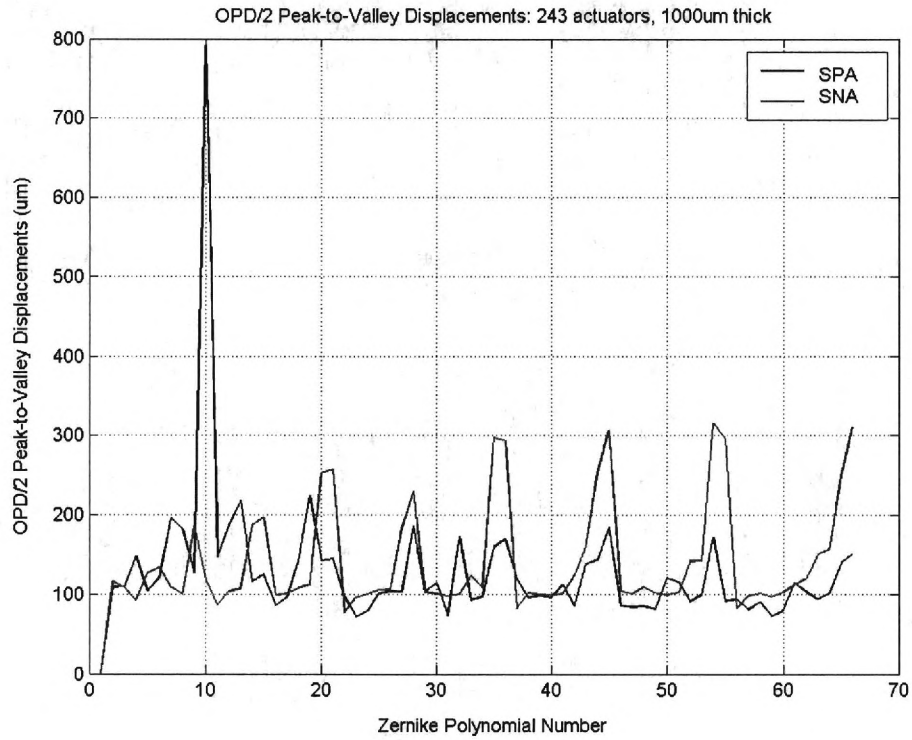


Figure 34. SNA vs. SPA Baseline P2V Comparison for the First 66 Zernike Polynomials.

The P2V deflection results might have significant impact on the effectiveness of the SPA system should an aberration of the facesheet be composed of high-amplitude, high-order Zernike modes. However, deformation requirements are application dependent and a parameter optimization could improve performance for relevant modes.

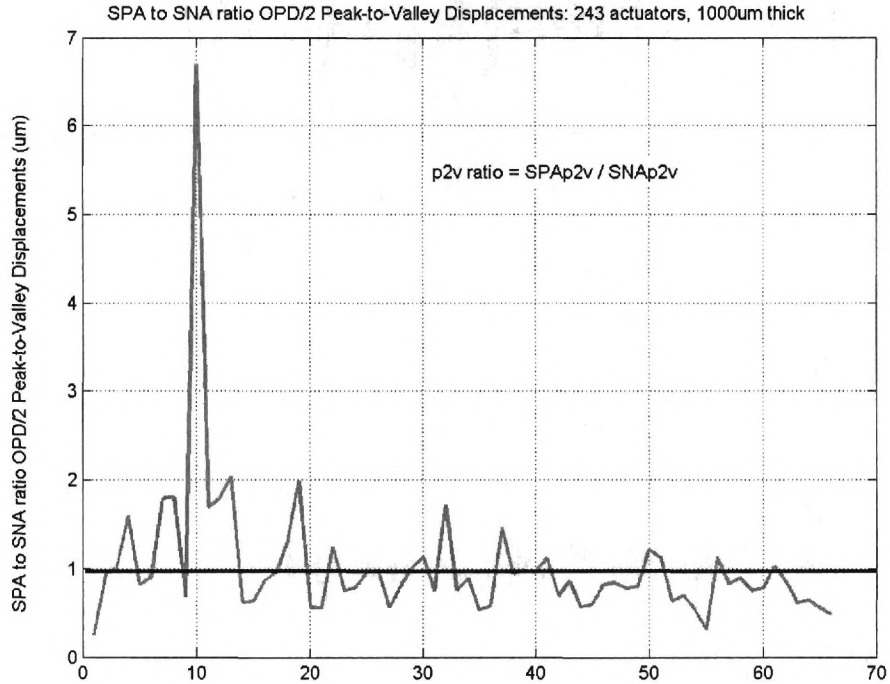


Figure 35. Improvement of SPA over SNA in term of P2V.

SPA consistently out performs SNA in terms of the RMS error between the actuated and desired Zernike mode shape. For P2V the SPA out performs SNA in only 18 of 66 modes (27%). The SPA case is particularly proficient at forming modes without a sinusoidal component, as listed in Table 3.

Table 3. Modes without Sinusoidal Components

Zernike Mode	Polynomial
13	$6*r^4-6*r^2+1$
25	$20*r^6-30*r^4+12*r^2-1$
41	$70*r^8-140*r^6+90*r^4-20*r^2+1$
61	$252*r^{10}-630*r^8+560*r^6-210*r^4+30*r^2-1$

In no case does SPA perform an order of magnitude worse than SNA, and is thus comparable in terms of both RMS error and P2V suggesting that overall all SPA is feasible.

### 4.3 Baseline Comparison: Number of Actuators

This section examines the RMS error in forming the first sixty-six Zernike polynomials for 15 to 3663 actuators. While this indicates the expected result that for SPA and SNA designs RMS error decreases as the number of actuators is increased, it also indicates that beyond the 45-93 actuator range, RMS error decreases faster for SNA and until rates converge at 2073 actuators. Figure 36 shows the affect of increasing actuators on RMS.

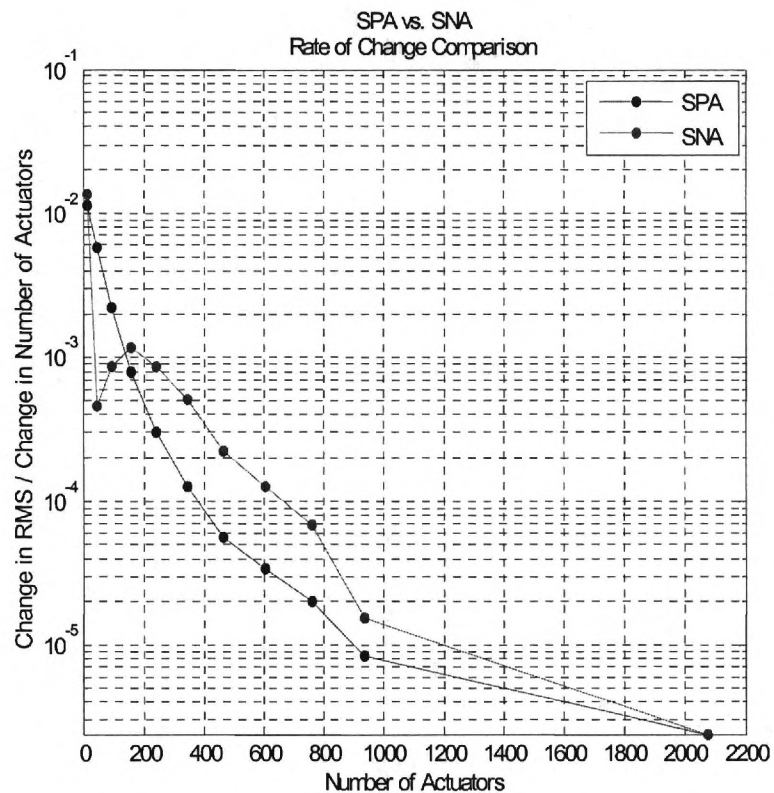


Figure 36. SPA vs. SNA Rate of Change for RMS Errors.

The higher rate of decrease for SNA is reflected in Figure 37 where SNA more efficiently utilizes additional actuators.

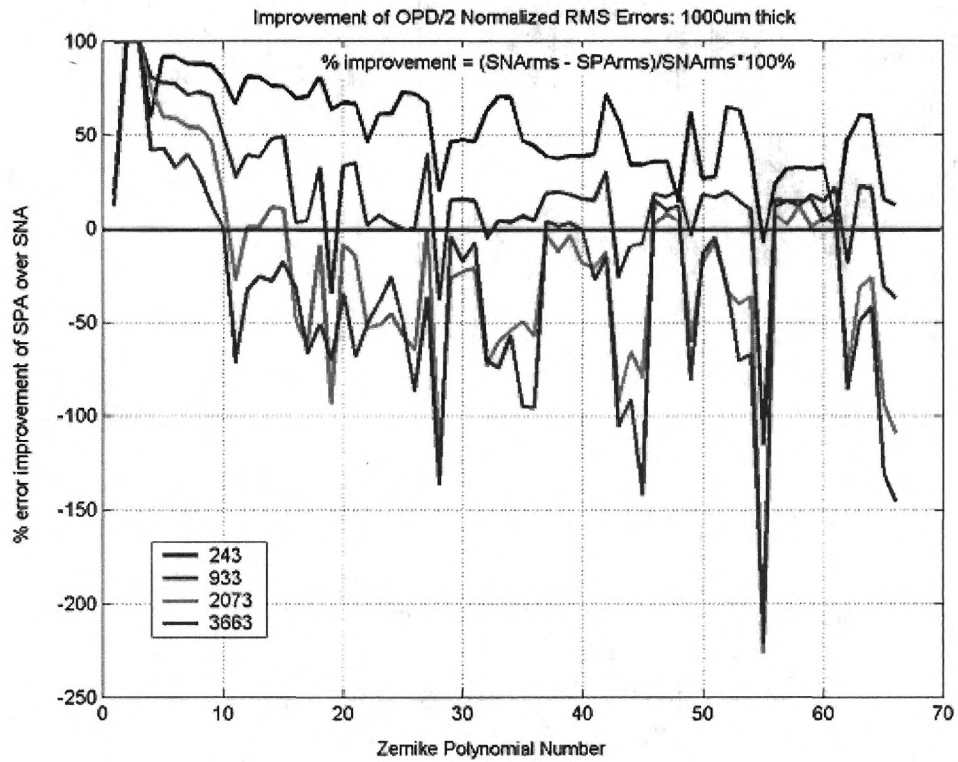


Figure 37. Percent Error Improvement of SPA over SNA for 243, 933, 2073, and 3663.

As seen in Figure 38 and Figure 39, for increasing actuators the RMS error profile for SPA and SNA each approach a different characteristic shape and magnitude. The characteristic shapes seen towards the bottom of Figure 38 and Figure 39 are clearly present in the baseline case of 243 actuators. As suggested in Section 4.2, this indicates that each design has unique strong and weak modes of correction, and as discussed in Section 4.4 the orientation of the Zernike modes across the substrate influences performance.

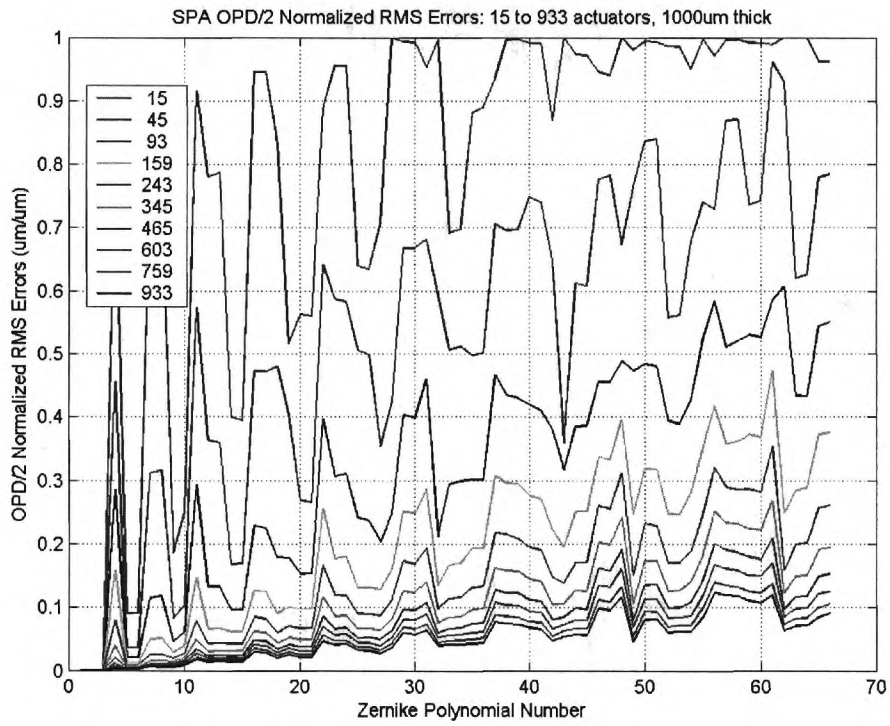


Figure 38. SPA RMS Error for 15-933 Actuators.

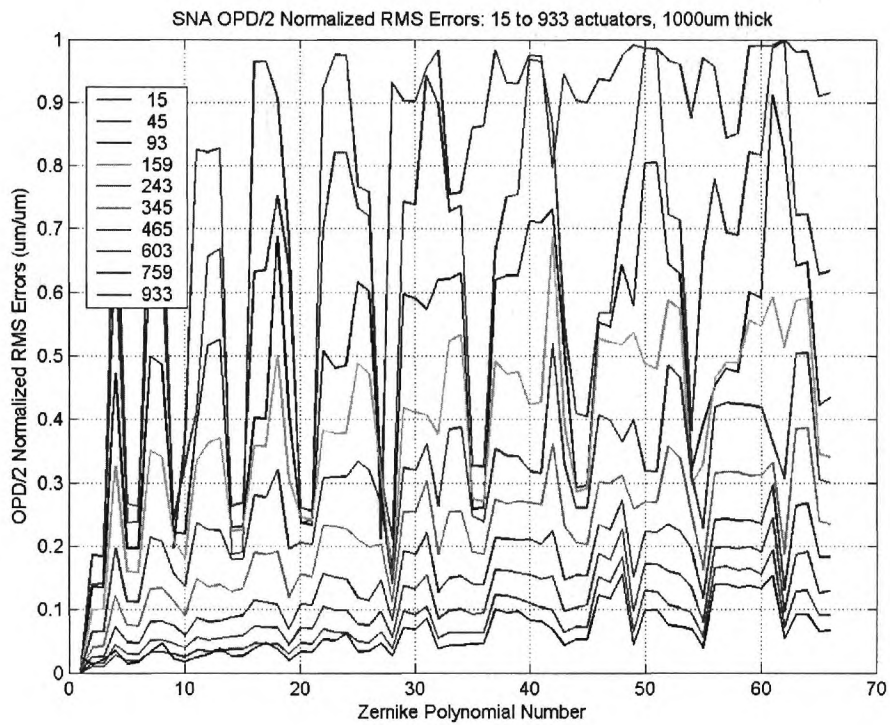


Figure 39. SNA RMS Error for 15-933 Actuators.

P2V, as shown in Figure 40 and Figure 41, was evaluated for varying quantities of actuators. For lower numbers of actuators (in this case 243 and 933) the SPA and SNA designs perform similarly for a large number of Zernike modes. For higher numbers of actuators such as 2073 and 3663 the SPA P2V is greater.

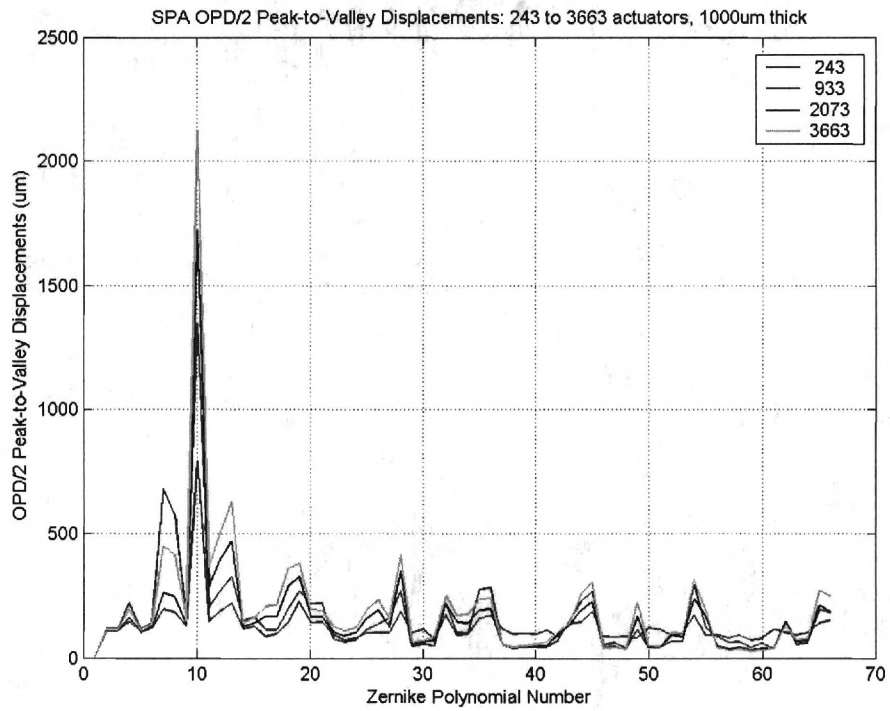


Figure 40. SPA P2V Performance for 243, 933, 2073, and 3663 Actuators.

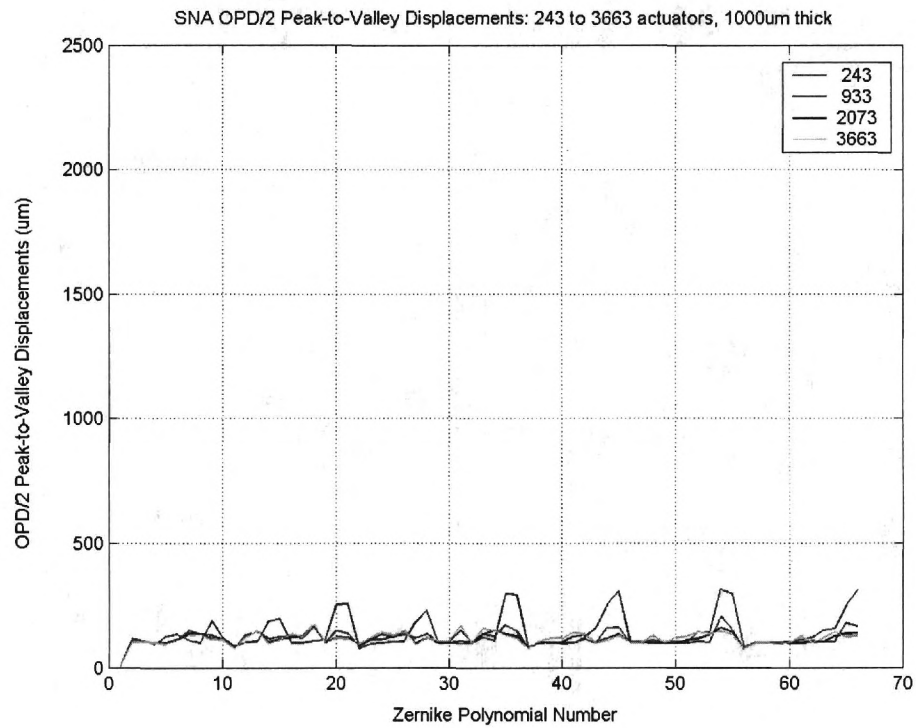


Figure 41. SNA P2V Performance for 243, 933, 2073, and 3663 Actuators.

Figure 42 plots the ratio of SPA to SNA P2V. For 2073 and 3663 actuators the ratio favors SPA for the majority of Zernike modes. As the number of actuators decreases to 243, the SPA P2V is consistently exceeded by SNA. This is consistent with Figure 94 and Figure 95, located in Appendix C, which show P2V for 15 to 933 actuators. Importantly, these figures emphasize that despite variations from mode to mode, for lower numbers of actuators SPA and SNA generally perform similarly. For both designs most P2V values range from 100 to 400  $\mu\text{m}$ , which is sufficient for SPA feasibility.

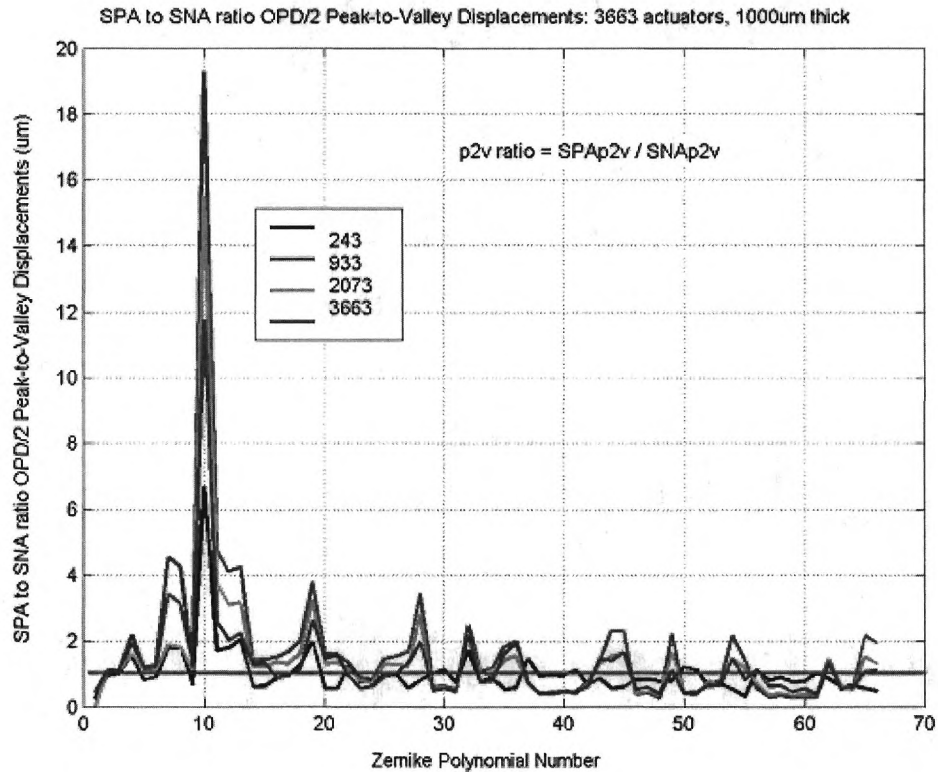


Figure 42. Ratio of SPA to SNA P2V for 243, 933, 2073, and 3663 Actuators.

In summary, for increasing numbers of actuators SPA produces a decrease in RMS error similar to that of SNA, though SNA does so more efficiently. Increasing

the number of actuators leads to similar characteristic RMS error plots for each, but values differ from mode to mode. As the number of actuators increase the P2V values for both designs generally remain within the 100 to 400  $\mu\text{m}$  range.

#### 4.4 Modality and Comments on Modes 7 and 10

As indicated in previous sections, certain modes are manipulated with a higher accuracy and deformation than other modes. To illustrate this, modes 7 and 10 (shown in Figure 43 and Figure 44) are discussed in this section. Mode 7 and 10 are show that a slight rotation about the optical axis, in this case  $30^\circ$ , greatly affects performance between modes. Though modes 7 and 10 are otherwise identical, the  $30^\circ$  rotation causes the peak to valley deflection to differ significantly, going from 127 to 792  $\mu\text{m}$ .

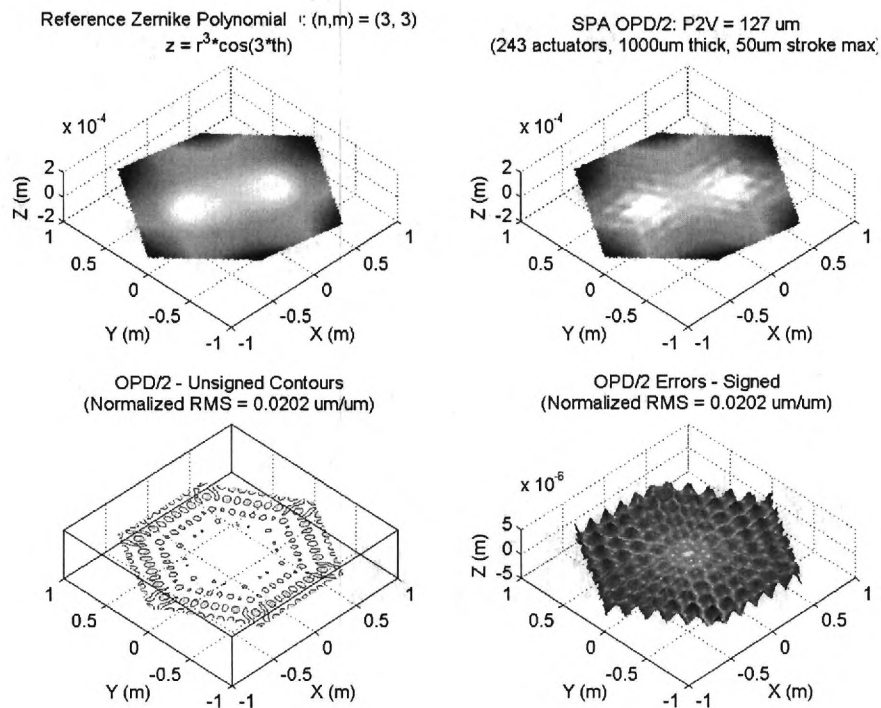


Figure 43: Zernike Polynomial 7

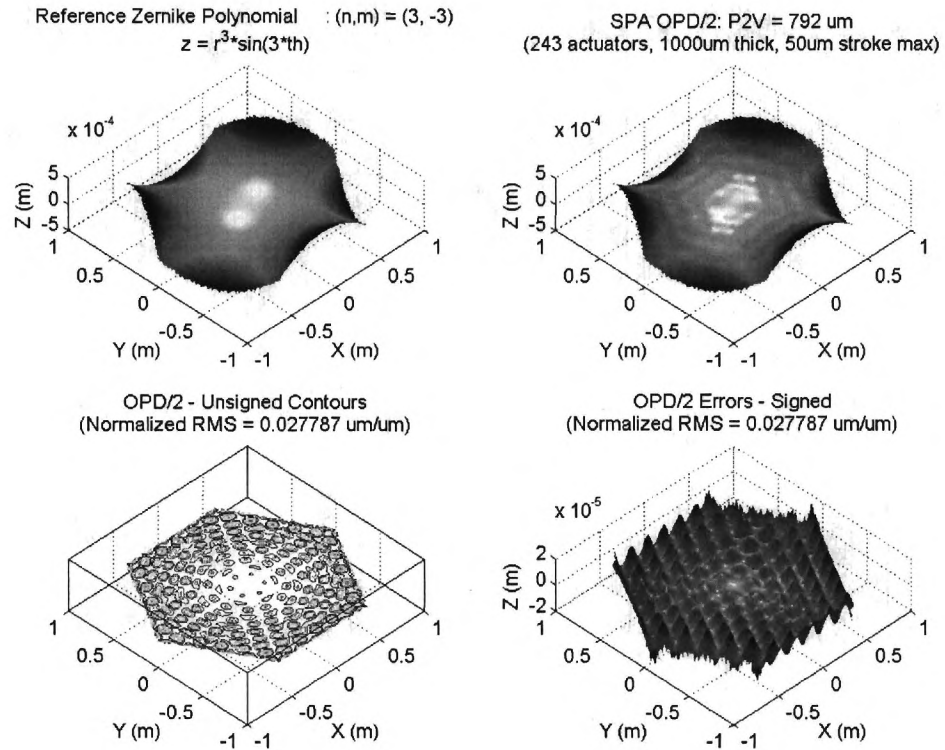


Figure 44. Zernike Polynomial 10

Since each Zernike mode is "forced" onto the facesheet, identical aberrations, less a rotation, should impart identical displacements (prior to the scaling of the actuator strokes). However, when the strokes are scaled to produce a maximum stroke of 50  $\mu\text{m}$  the resulting deflection of the facesheet for nearly identical aberrations differs because:

1. The deformable mirror is stiffer in some directions than others, and
2. The cumulative effect of the actuators is directional.

Thus, when scaled, the deformations of modes similar to 7 and 10 will differ significantly between one another because the strokes required to produce them differed initially.

Figure 45 and Figure 46 show that the number of circumferential sinusoidal oscillations for modes 7 and 10 correspond exactly to the substrate symmetry. In Figure 45 the sinusoidal peaks and valleys of mode 7 conform to the actuator runs along the three primary diagonals (red lines Figure 45). The zero deflection region lies *in between the major actual runs*.

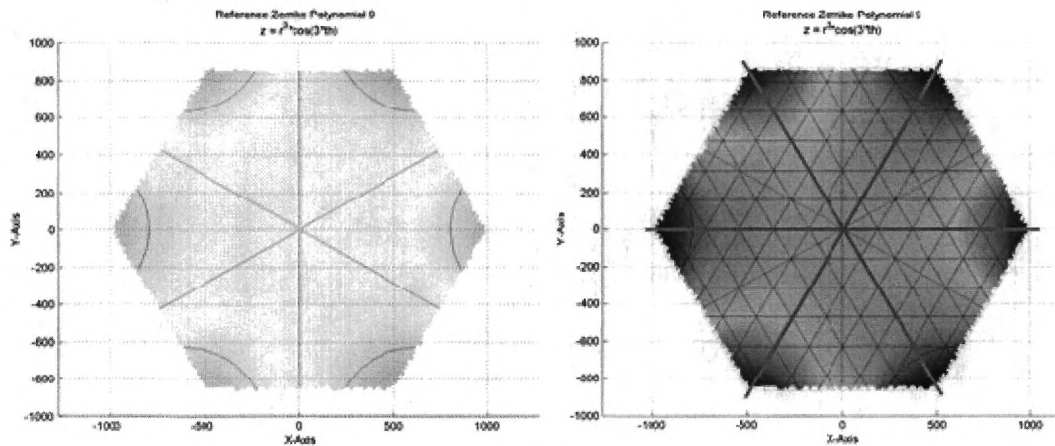


Figure 45. Symmetry Zernike Mode 9

For mode 10 in Figure 46 the peaks and valleys are bordered by the major diagonals of the substrate. The areas of zero or minimal deformation then lie *along the major actuator runs*. The truss sections located in between the major diagonals are also oriented differently relative to mode 7. This suggests that between modes there is either a variance in flexibility, local actuator influence, or both.

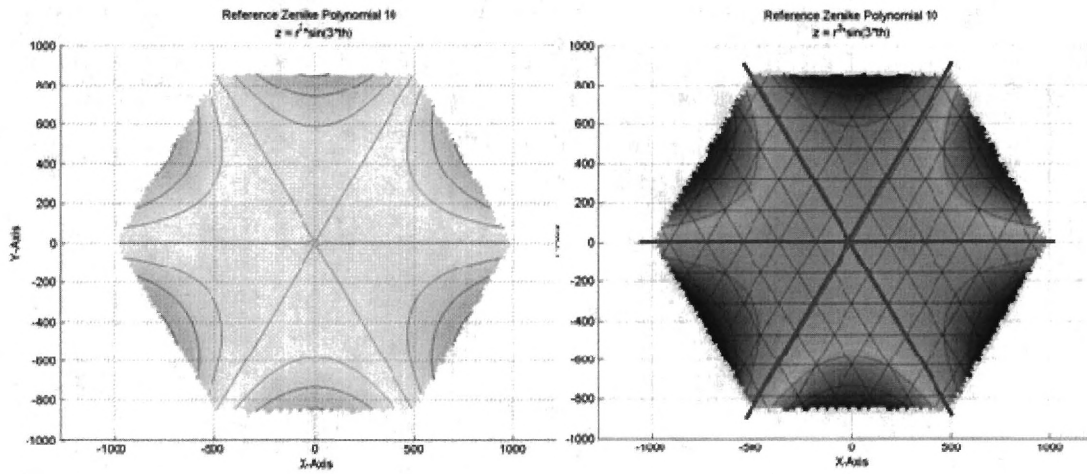


Figure 46. Symmetry Zernike Mode 10

Similar results are seen in modes 17 and 20 (Figure 47 and Figure 48) which have the same sinusoidal symmetry as modes 7 and 10 respectively. Though the difference is not as extreme there is still a significant variation in deflection between the modes (143 and 223  $\mu\text{m}$  respectively).

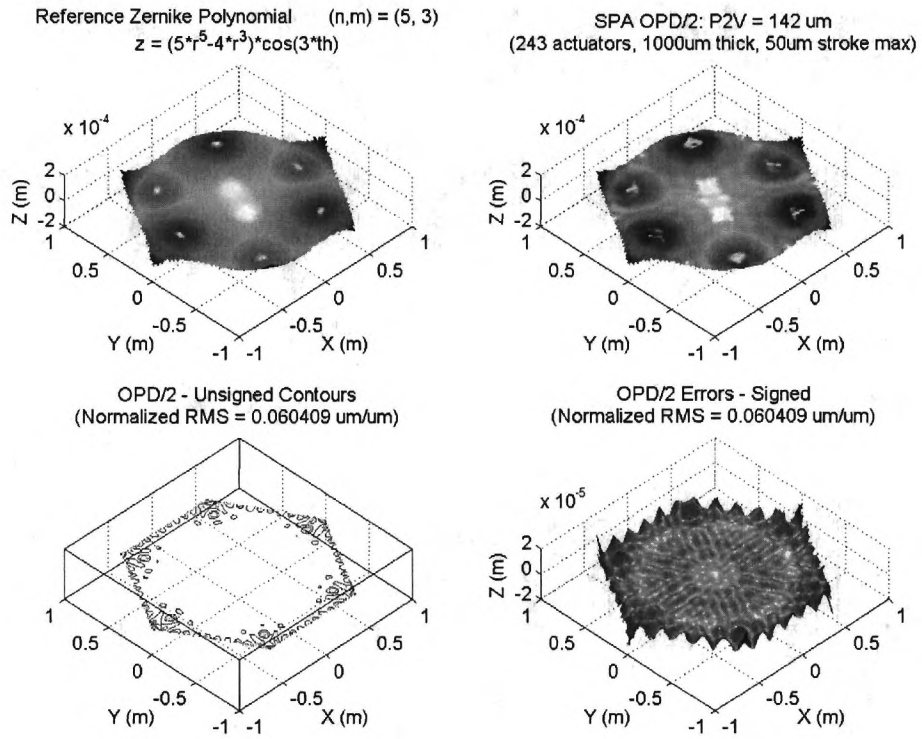


Figure 47. Zernike Polynomial 17

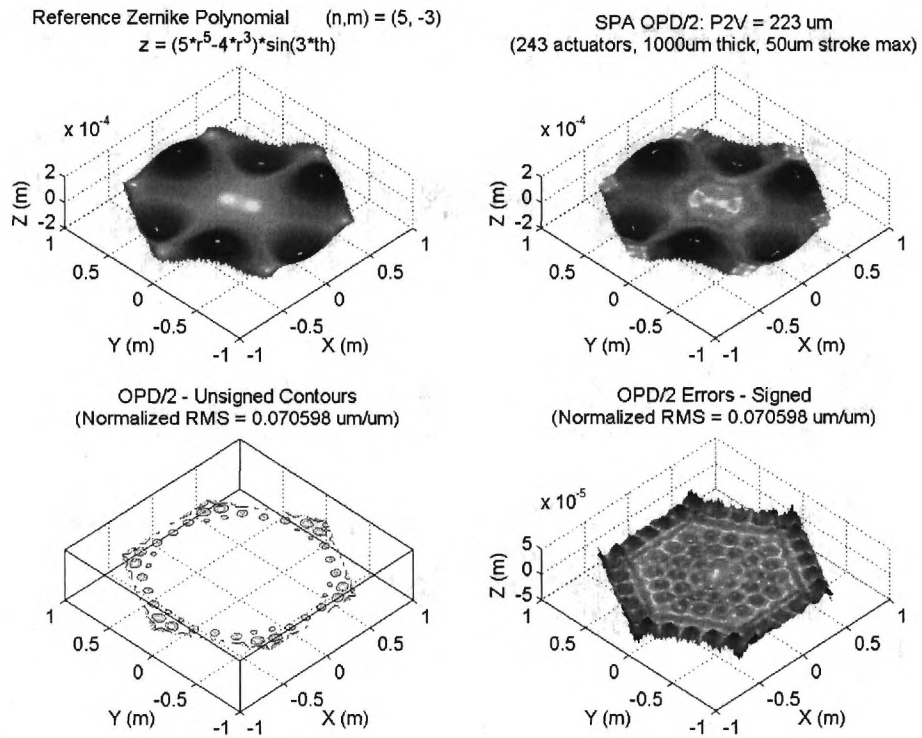


Figure 48. Zernike Polynomial 20

In summary a substantive example of SPA's modal nature has been provided and it reasonable to conclude that some modes will be better corrected than others do to their relative orientation, and furthermore that it would be advantageous to design or orient the mirror away from those modes.

#### **4.5 Surface Thickness**

Thickness strongly influences the performance of SPA and SNA in terms of aberration RMS error. Generally, the performance of SPA and SNA designs for varying thicknesses differ from each other and from mode to mode (Figure 49 and Figure 50). Changing the thickness from 100 to 1000  $\mu\text{m}$  in both the SPA and SNA designs causes each to approach a characteristic shape.

In comparison to SPA, SNA has more stratification over the same thickness range. This stratification does not appear to have a germane effect on feasibility and is described for completeness.

The percent improvement in RMS error of SPA over SNA is shown in Figure 51, and is germane to feasibility. It indicates that for thicknesses between 50-500  $\mu\text{m}$  SPA is significantly better than SNA for almost all modes. Thus, for the baseline case it is advantageous to use SPA for thinner facesheets than SNA, which is a poignant indication of the feasibility of SPA.

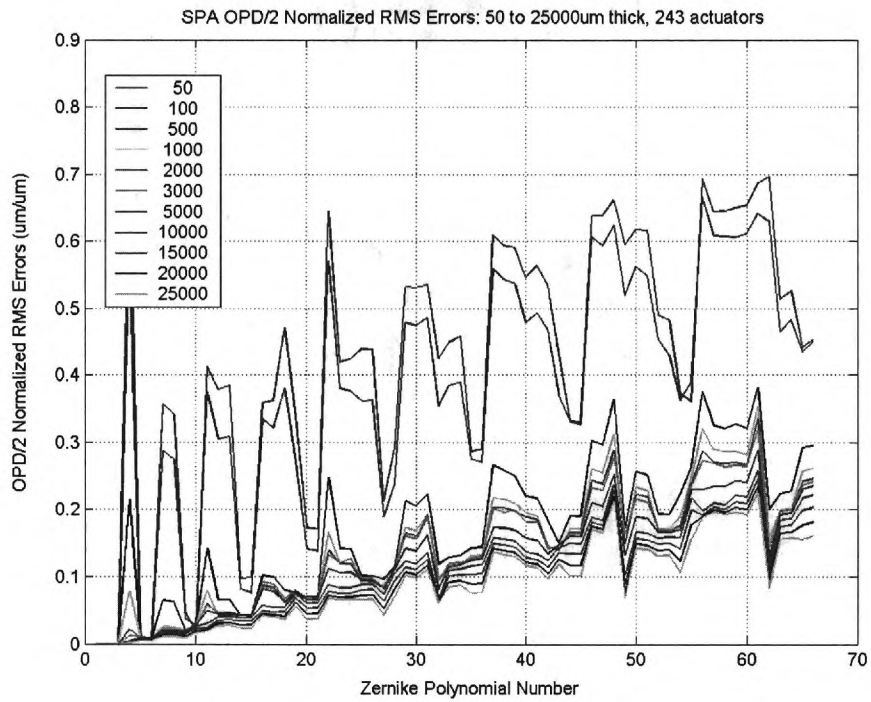


Figure 49. SPA RMS Error for Thickness of 50-25000  $\mu\text{m}$  for 243 Actuators.

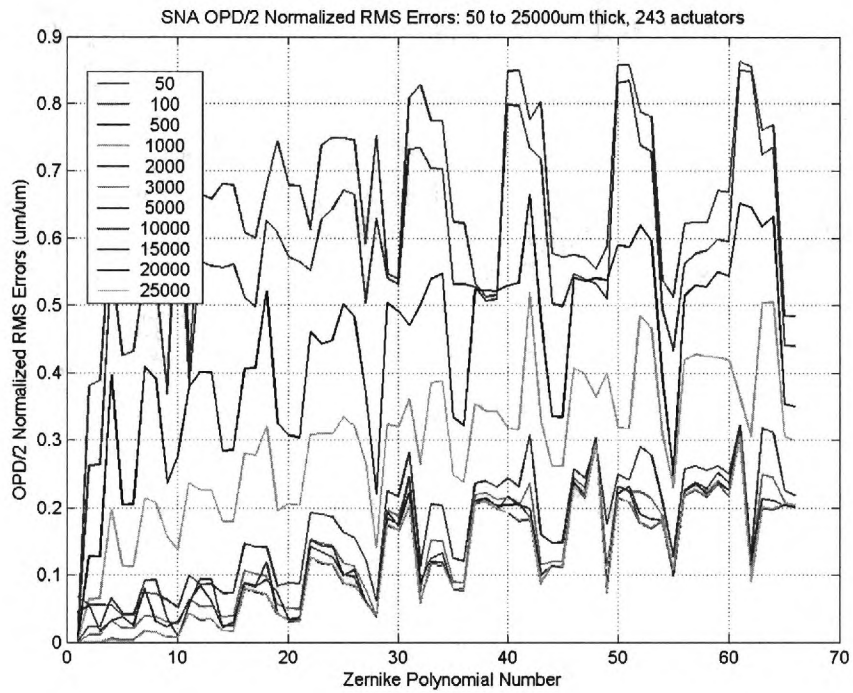


Figure 50. SNA RMS Error for Thicknesses of 50-25000  $\mu\text{m}$  for 243 Actuators.

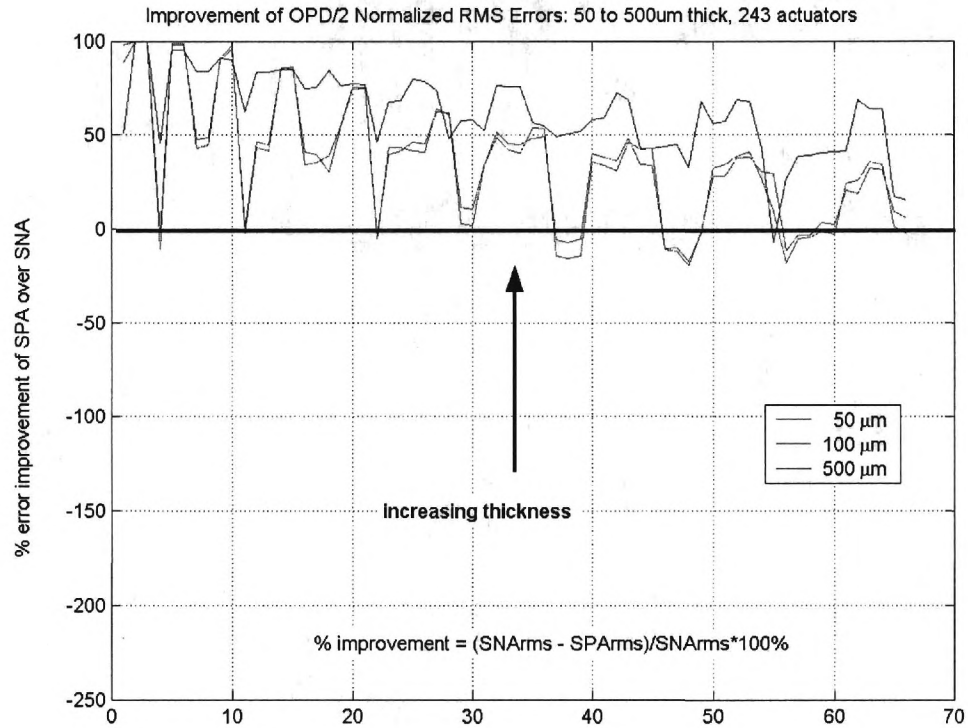


Figure 51. Improvement of SPA over SNA for Thicknesses of 50-500  $\mu\text{m}$ .

#### 4.6 Truss Height

Truss height,  $h$ , is defined as a percentage of the depth of the mirror along the optical axis from rim to center,  $d$  (recall **Error! Reference source not found.** on page **Error! Bookmark not defined.**). The parameter  $h$  is only valid for the SPA since it is the amount by which the truss is off-set from the mirror. This principally affects the deflection of the facesheet for a given amount of stroke and the ratio of tangential to normal force imparted to the facesheet. Figure 52 represents a simplification of truss bending, in which a single truss section pivots about a center “joint” rather than flexing.

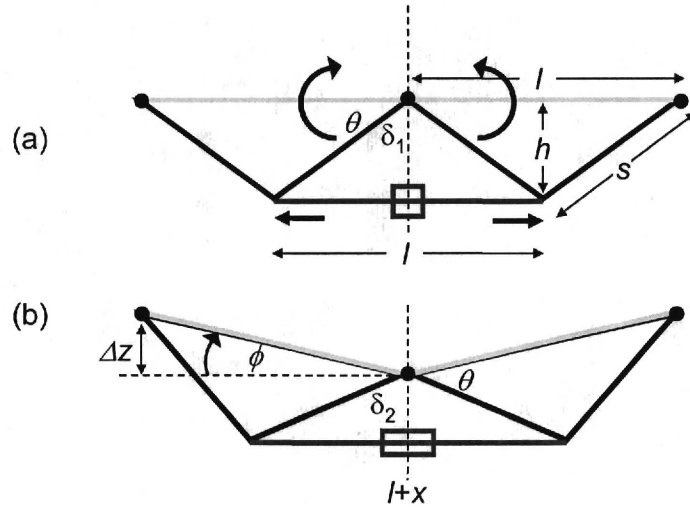


Figure 52. Simplified Truss Bending.

Based upon the above simplification, the strut length  $s$  is given as a function of truss height,  $h$ ,

$$s = \left( \frac{l^2}{4} + h^2 \right)^{\frac{1}{2}} \quad (25)$$

where  $l$  is half the length of a section and equal to the initial actuator length.  $\delta_1$ , which equals  $\theta$  initially, represents half the center angle of the truss and  $\delta_2$  is the value after the actuators have extended by  $x$ ,

$$\begin{aligned} \theta &= \delta_1 \\ \delta_1 &= \sin^{-1} \left( \frac{l}{2s} \right) \end{aligned} \quad (26)$$

$$\delta_2 = \sin^{-1} \left( \frac{l+x}{2s} \right) \quad (27)$$

Angle  $\phi$  is the change in the inside angle, and  $\Delta z$  is the deflection of the facesheet for small angles,

$$\phi = \delta_2 - \delta_1 \quad (28)$$

$$\Delta z = l\phi \quad (29)$$

Using equations (25)-(29), Figure 53 shows that an order of magnitude decrease in truss height should increase deflection of the facesheet by an order of magnitude. This is confirmed for some modes in Figure 54 and Figure 55.

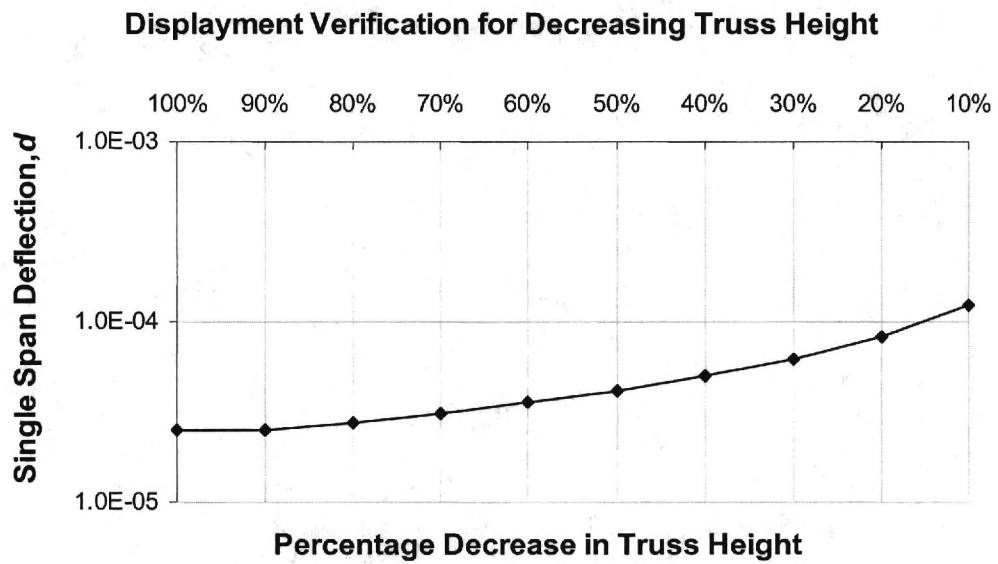


Figure 53. Simplified Single Span Displacement as a Function of Percent Decreased in Nominal Truss Height,  $d$

Using the baseline 243 actuator case, Figure 54 shows that for the nominal truss height the P2V for mode 10 is about 800  $\mu\text{m}$ . Figure 55 shows that for 10 percent of the nominal truss height, the P2V for mode 10 is greater than 8000  $\mu\text{m}$ . Consistent with the previously mentioned modal nature of SPA only some modes are significantly affected by a change in truss height.

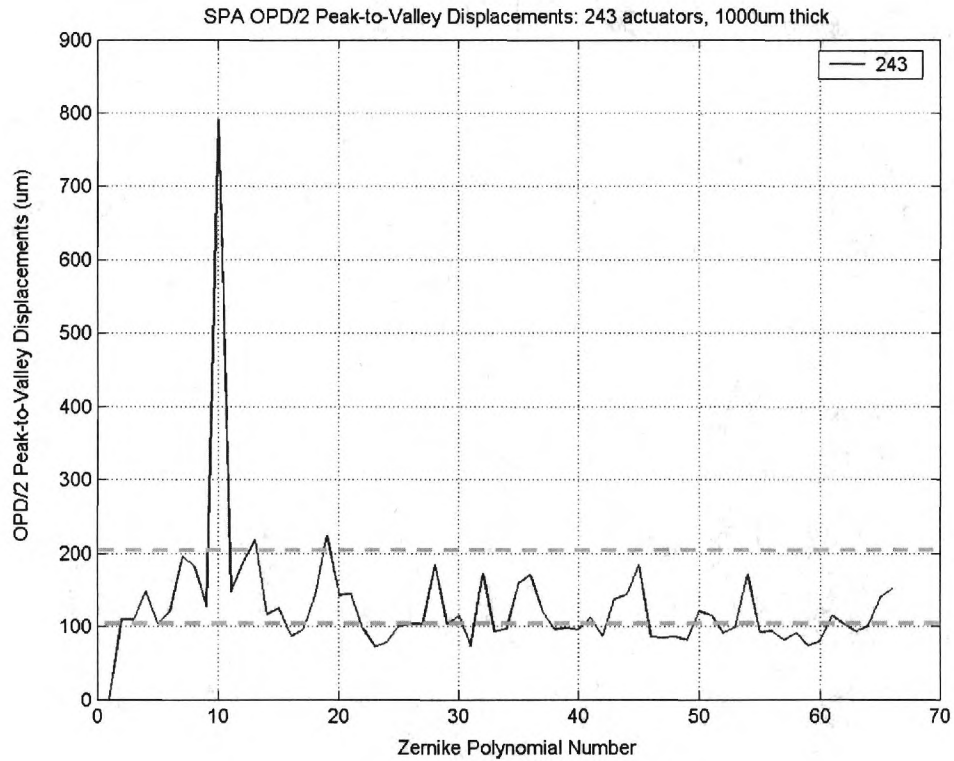


Figure 54. SPA Deflection for 100% Truss Height and 243 Actuators.

Within the 100 and 200  $\mu\text{m}$  P2V range (Figure 54) and the 1000 and 2000  $\mu\text{m}$  range (Figure 55), the baseline case does not perform similarity, aside from overall magnitude. These ranges are highlighted by orange dashed boundary lines in both figures. In general, while many modes increase several times, they do not increase anywhere near a full order of magnitude. Several of the modes straddling the 100  $\mu\text{m}$  line in the one hundred percent truss height case only increase by a few 100  $\mu\text{m}$  when

the truss height is decreased to ten percent. The 100  $\mu\text{m}$  line is indicated approximately by a green line in Figure 55. The lack of increase across all modes is further indication of the modality mentioned in Section 4.4.

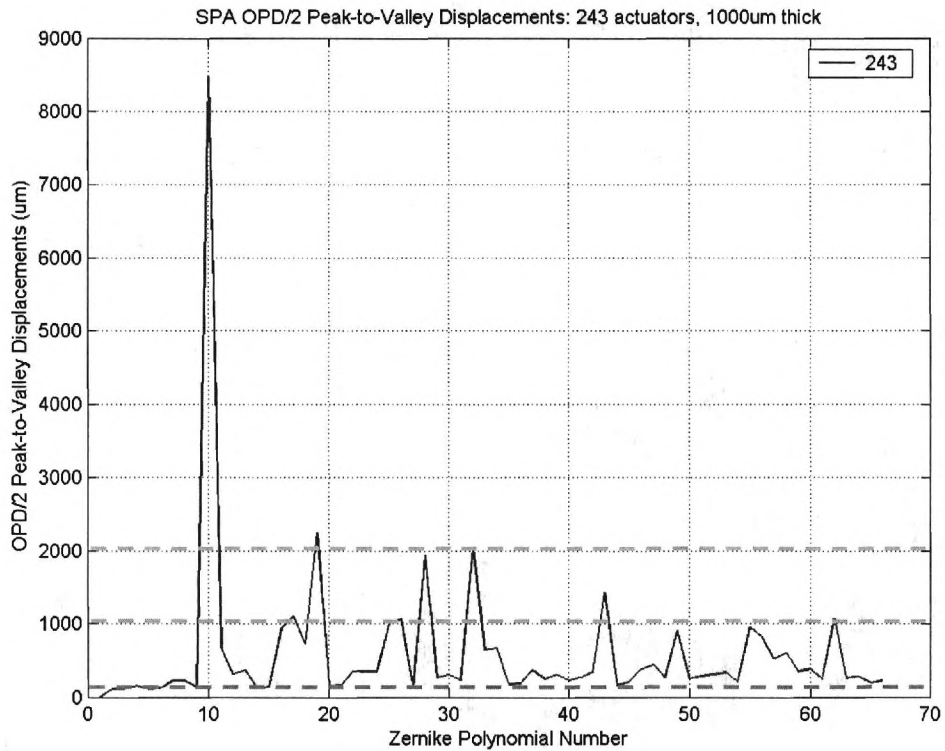


Figure 55. SPA P2V Deflection for 10% Truss Height and 243 Actuators.

RMS values are generally not adversely affected by adjusting the truss height (Figure 56) and variation between truss values from mode to mode is relatively slight. The changes range from about quarter to a half of a percent. Therefore, the primary advantage in varying the truss height is in the ability to increase the P2V deflection, and thus the magnitude of aberration, that can be addressed for select modes.

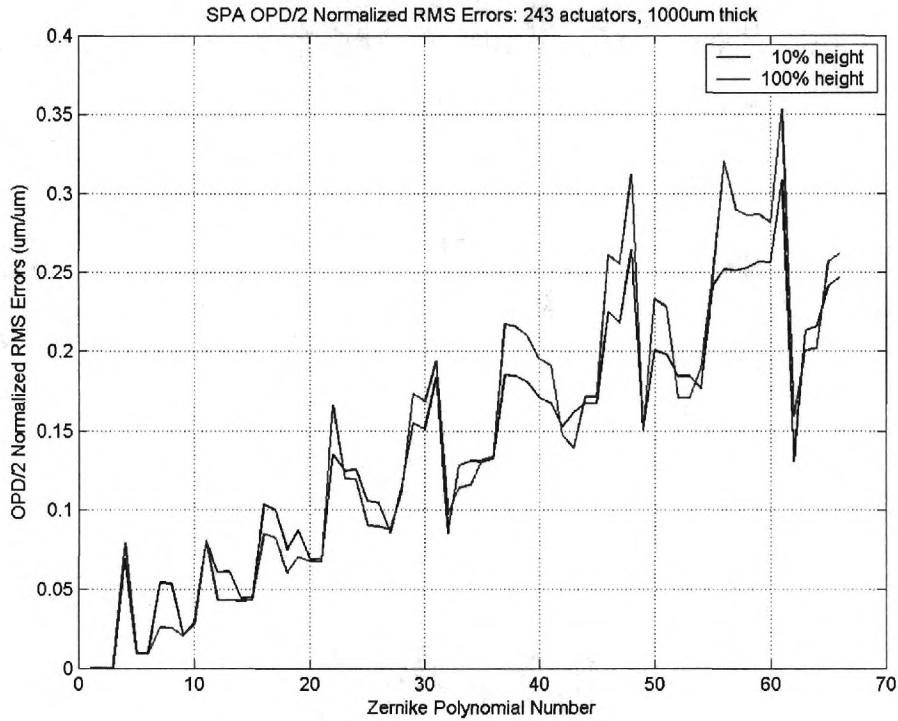


Figure 56. RMS Error for 100% and 10% truss height for 243 actuators.

Forces were not explicitly simulated in this portion of the study. However, as  $\theta$  (see Figure 52) approaches zero so does  $\tan\theta$  requiring greater tangential forces is applied to the facesheet. The SPA design was not studied to determine the optimum forces to apply to efficiently manipulate various Zernike modes. However, based on the JPL actuators that are being researched for this application (high-displacement low-force), it is clear that truss height must be optimized to provide the most useful forces to the facesheet.

In summary, adjusting truss height increases displacement for select modes, but exerts little influence over RMS error. It decreases the normal force transmitted by the actuators and increases the tangential force. It can be concluded that for low-force high-displacement actuators, decreasing truss height to provide for additional

displacement maybe a poor design choice. Truss height should be optimized to maximize the size of aberration that can be corrected while providing optimal forces to the facesheet.

#### **4.7 Qualitative Evaluation of Print-Through**

Print-through is the highly localized aberration of the facesheet at truss connection points. However, it is not well quantified in literature (if at all). Here it is defined as any repeating pattern of aberration that adheres closely to one or more strut-facesheet connection points. Since print-through is not characterized numerically, this study assumes it is adequately accounted for in RMS error calculations.

Print-through occurs because of an aberrating effect such as a thermal load or a displacement of the substrate. The level of acceptable print-through is delineated by the spectrum of light over which the telescope will operate. Significant print-through causes unwanted localized shifts in the phase of the incident light thus impairing the ability of the telescope to correct an aberration. For operation in the visible to near infrared spectrum print-through (or its effects) must be limited to tens of nanometers (based upon an error budget of one tenth of a wavelength).

Four pairs of representative examples illustrate the print-through “properties” of the two designs (Figure 57 through Figure 64). Table 4 lists the Zernike aberrations used.

Table 4. Zernike Modes Used in Evaluation of Print-Through.

Zernike Mode	Polynomial
10	$r^3 \sin(3\theta)$
12	$(4r^4 - 3r^2) \sin(2\theta)$
18	$(10r^5 - 12r^3 + 3r) \cos(\theta)$
21	$r^5 \cos(5\theta)$

Two examples of a simple polynomial with high sinusoidal oscillation (modes 10 and 21) were chosen along with examples of a multi-term polynomial with a low sinusoidal oscillation (modes 12 and 18). Print-through may be dealt with in two ways, 1) physical reduction and/or 2) algorithmic elimination via filtering. It is likely that the regularly distributed print-through can be characterized by an image processing tool and algorithmically removed. It is also likely that adjustment of the deformable mirror's physical parameters can reduce the physical presence of print-through such as softening the struts or selective thickening of the facesheet.

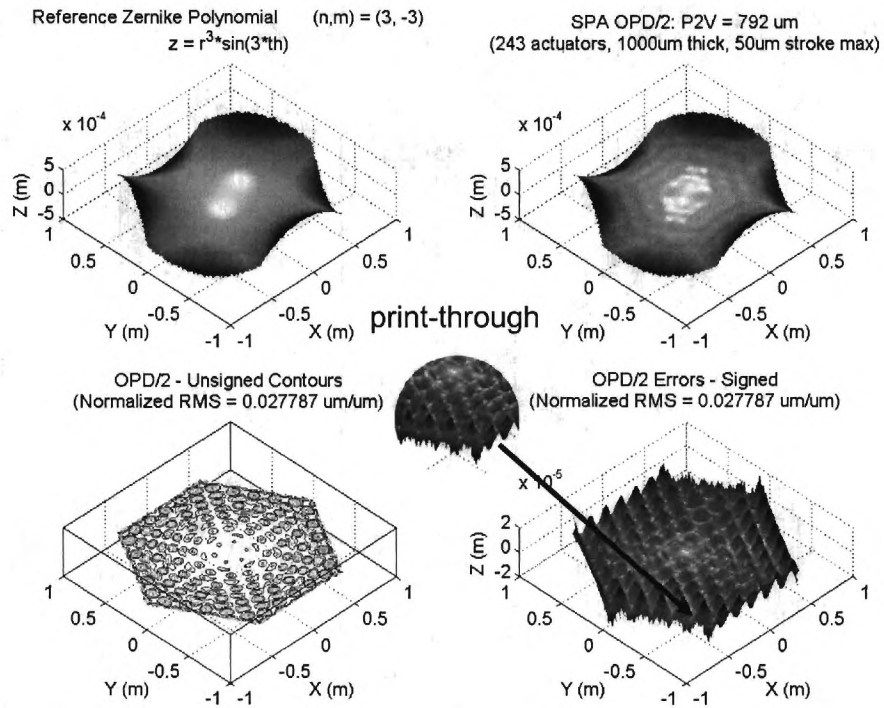


Figure 57. SPA Zernike Mode 10 -  $r^3 \sin(3\theta)$ .

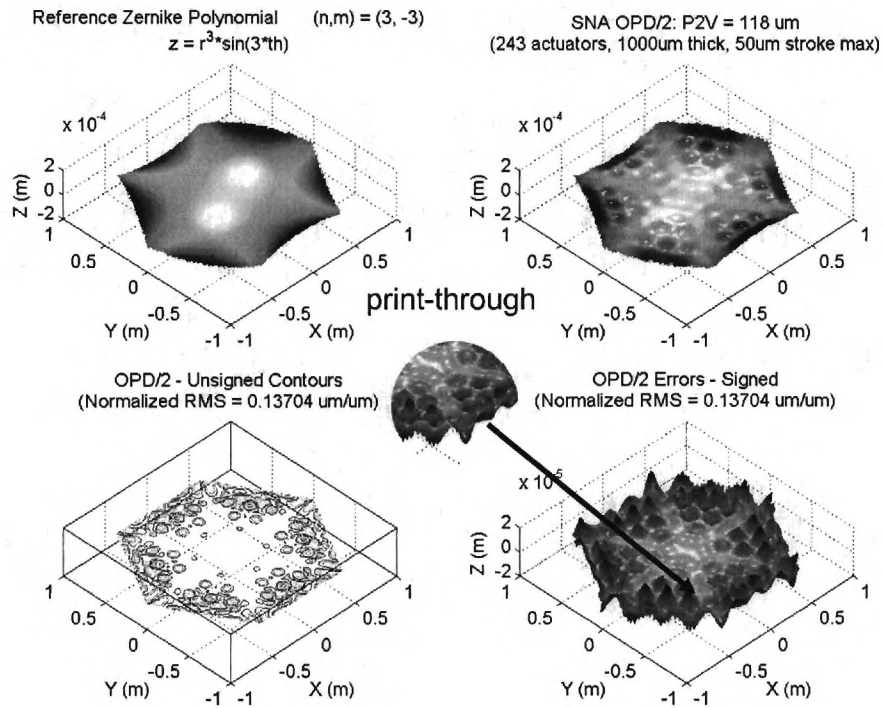


Figure 58. SNA Zernike Mode 10 -  $r^3 \sin(3\theta)$ .

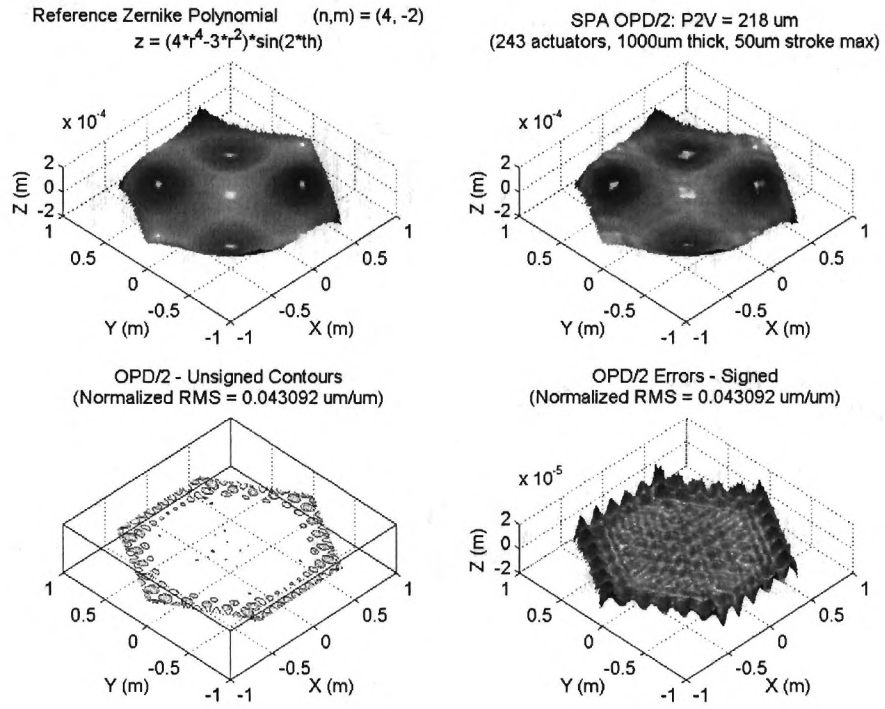


Figure 59. SPA Zernike Mode 14 -  $(4r^4 - 3r^2) \sin(2\theta)$ .

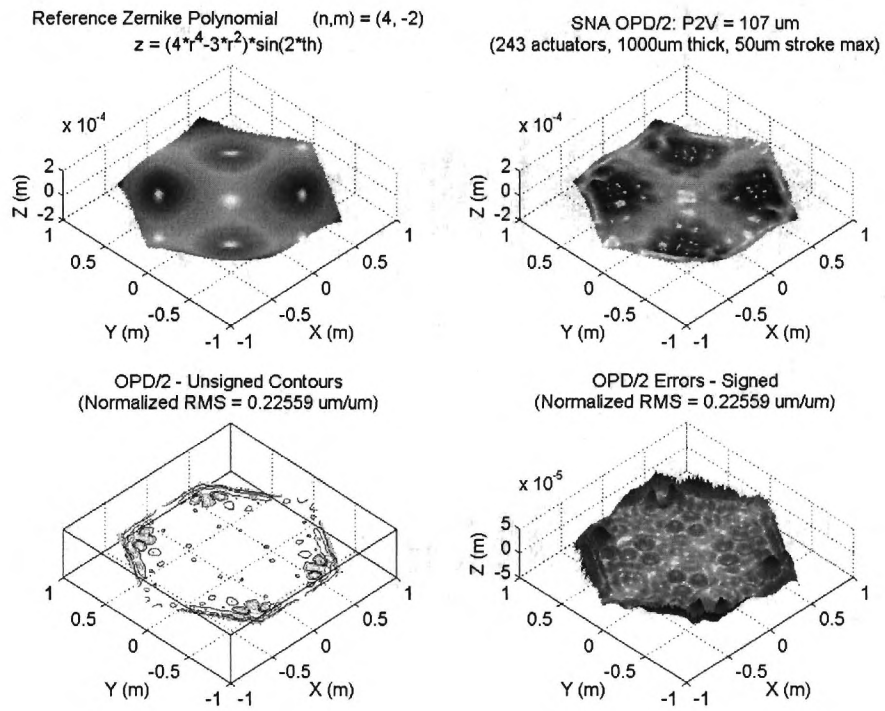


Figure 60. SNA Zernike Mode 14 -  $(4r^4 - 3r^2) \sin(2\theta)$ .

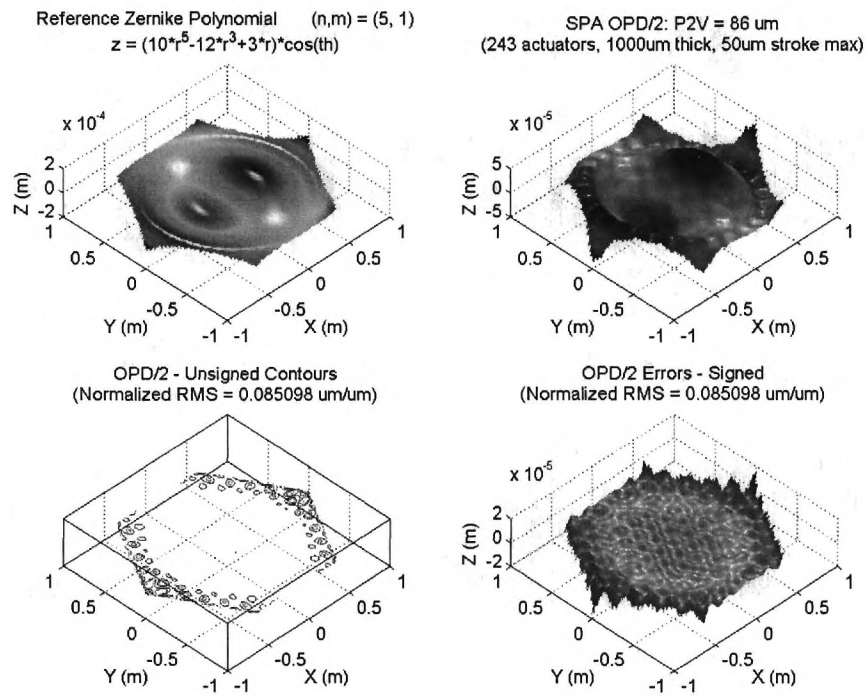


Figure 61. SPA Zernike Mode 18 -  $(10r^5 - 12r^3 + 3r) \cos(\theta)$ .

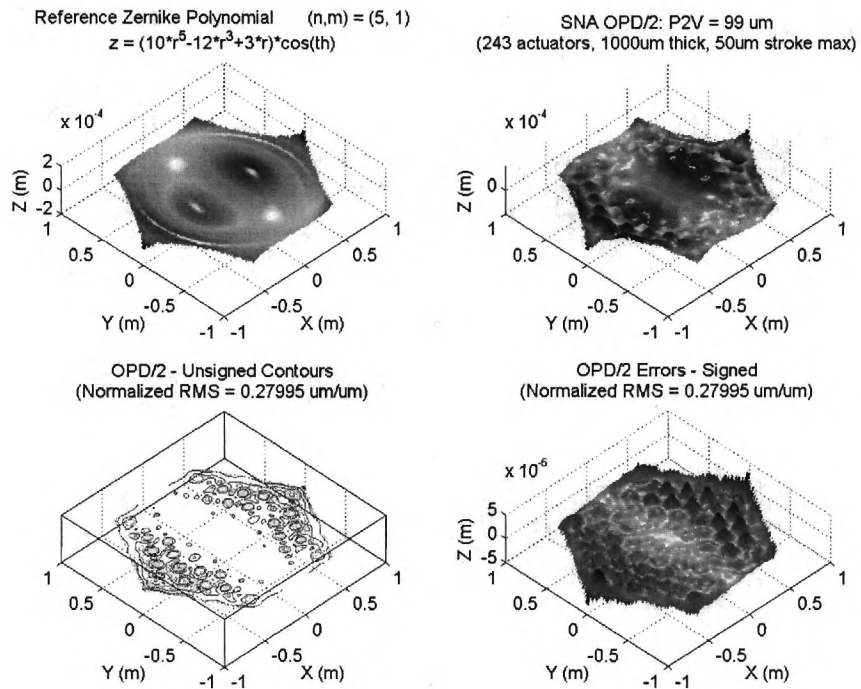


Figure 62. SNA Zernike Mode 18 -  $(10r^5 - 12r^3 + 3r) \cos(\theta)$ .

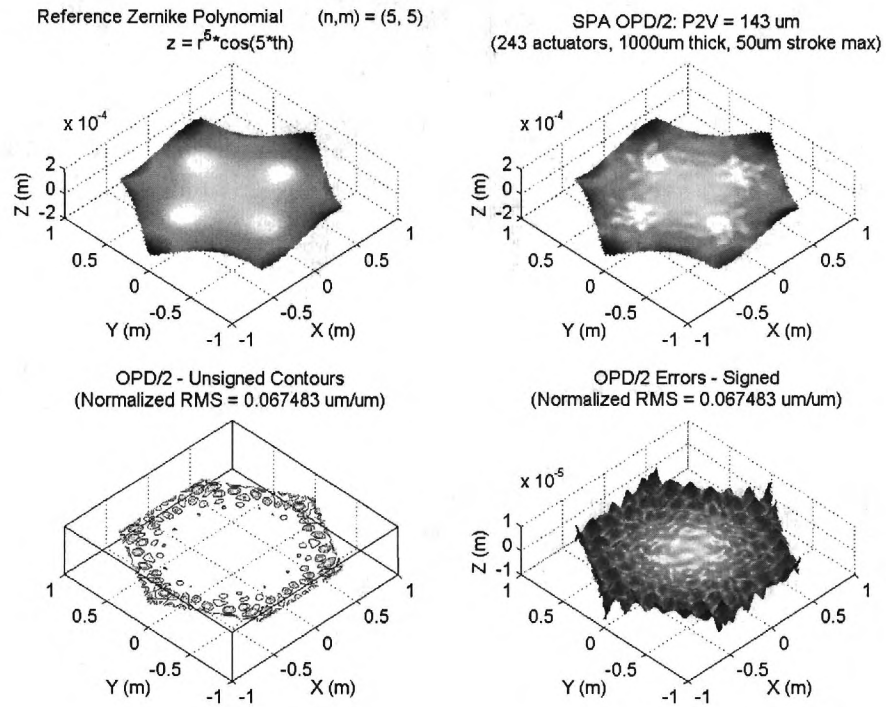


Figure 63. SPA Zernike Mode 16 -  $r^5 \cos(5\theta)$ .

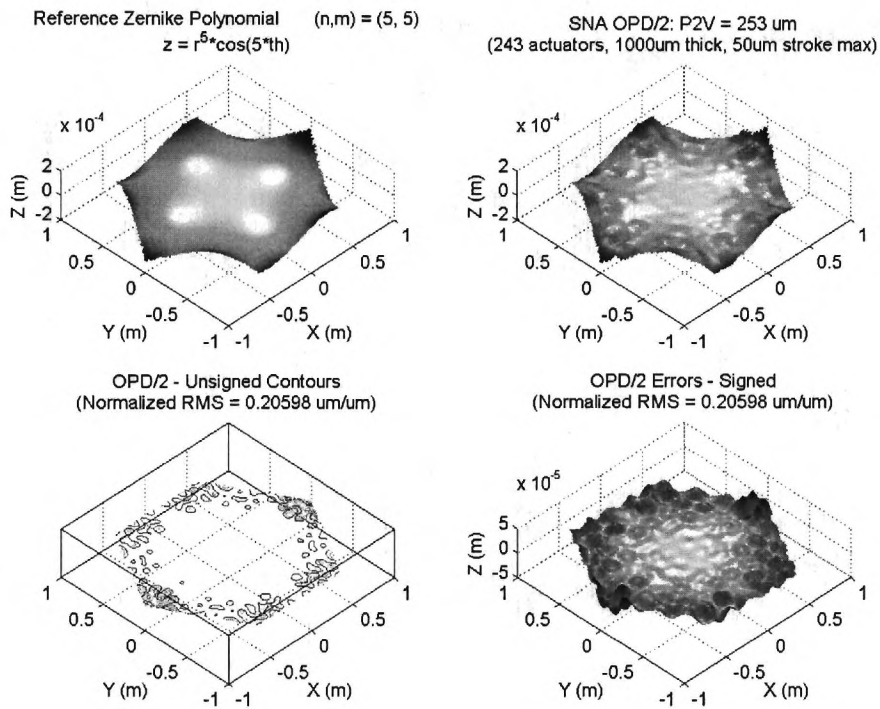


Figure 64. SNA Zernike Mode 16 -  $r^5 \cos(5\theta)$ .

#### **4.8 Conclusions and Design Criteria for Feasibility**

Feasibility of the SPA deformable mirror technology is established by comparing equivalent SPA and SNA cases to accurately form individual Zernike polynomials over a range of selected parameters: number of actuators, facesheet thickness, and truss height. Results are summarized and limited design guidelines are drawn.

In terms of RMS error the 243 actuator baseline SPA mirror with has greater accuracy over a large range of Zernike modes. Overall the performance of SPA is somewhat mode dependent and sensitive to the mode orientation with respect to the substrate.

For increasing numbers of actuators SPA effectively decreases RMS error between the desired and actuated (actual) figures, but requires more actuators than SNA. When considering for P2V deformation SPA yields greater amplitudes than SNA for increasing numbers of actuators. Furthermore each mirror type approaches a clear characteristic performance from mode to mode as the actuators increase.

Better performance at lower thicknesses is a clear advantage of SPA over SNA. Thickness influences the RMS values as well as the characteristic shape. For thinner facesheets in the 50-500  $\mu\text{m}$  range SPA does significantly better. This is highly beneficial for light-weighting the mirror.

Decreasing truss height increases facesheet displacement and in some cases helps to reduce RMS error. Truss height affects the characteristic shape of the P2V plots but the affect on RMS error is negligible. However, this comes at the cost of increased actuator forces (Section 4.2) and is a significant factor given the low-force, high-displacement actuators selected for this application.

For both designs the print-through expectedly follows the spatial pattern of the truss connection points. However, the print-through, or at least its magnitude, is evenly distributed in the SPA approach. Print-through in the SNA approach is located

towards the edges of the mirror. This even distribution indicates that SPA might be better equipped for correction via an image processing algorithm instead of additional physical manipulation. It is equally notable that if print-through could be sufficiently pushed to the edges of the mirror it could be excluded with other edged effects (similar perhaps to how gaps between segments are already handled).

## CHAPTER 5

# ANALYSIS OF THE SPA DEFORMABLE MIRROR FOR SELECT THERMAL GRADIENTS

Thermal deformation of the SPA DM is a significant source of figure error and thus a key concern of this work. Chapter 5 investigates the response of the SPA DM for select cases of thermal loading. Results are expressed in terms of the deformation under the following structural conditions:

1. Facesheet-Only Deformation

The influence of the substrate is removed by decreasing the substrate stiffness, thereby allowing the virtual free expansion of the facesheet.

2. Facesheet Deformation with Substrate Stiffness and Matched CTE

The substrate exerts limited influence on the facesheet due to equal thermal expansion of the truss.

3. Facesheet Deformation with Substrate Stiffness and Mismatched CTE

The substrate exerts a significant influence on the facesheet due to its stiffness and mismatched thermal expansion.

Condition (1) represents the ideal configuration in which the facesheet expands freely, uninhibited by the substrate. This condition allows for basic verification of the model in accordance with a simple linear calculation of the thermal expansion. Condition (2) represents the next best thermal case in which the substrate expands uniformly with the facesheet. This condition is contrasted with condition (3) which is considered here to be the worse case of a complete thermal mismatch where the substrate is defined to have a zero CTE and the facesheet a value of  $13\text{e-}6/^{\circ}\text{C}$ .

Two representative thermal loads are applied across the deformable mirror (facesheet and substrate), (1) A uniform load of 10°C and (2) a 1°C/m gradient along the  $x$ -direction of the DM. For completeness a 1°C/m thermal gradient in the  $y$ -direction and at a 45° angle with respect to  $x$ -axis are also presented. These two alternative load conditions take into account the difference in symmetry with respect to the  $x$  and  $y$  directions. Then case (3) is further studied for increasing numbers of actuators.

### 5.1 Thermal Boundary Conditions

The thermal boundary conditions are defined inside of the STAS tool (Figure 65). A different linear gradient may be applied to the facesheet, actuator layer, or to the tripod varying in the  $x$ ,  $y$ , and  $z$  directions. The unit of temperature for this study is Celsius and the reference temperature is zero for all analyses.

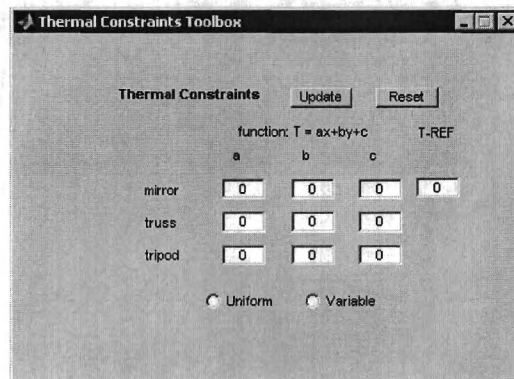


Figure 65. STAS Thermal Constraints (Boundary Conditions)

Figure 66 shows an FEM cross section of the mirror with a section of the thermal boundary conditions shown as blue tick marks on the mirror surface and at the joints of the substrate. Thermal values are explicitly defined at the end-points of the strut and actuator elements, and at each node of the mirror surface, thus when

ANSYS solves for the thermal distribution across the mirror there is virtually no difference. Note, the same structural degrees of freedom apply as in the previous structural cases.

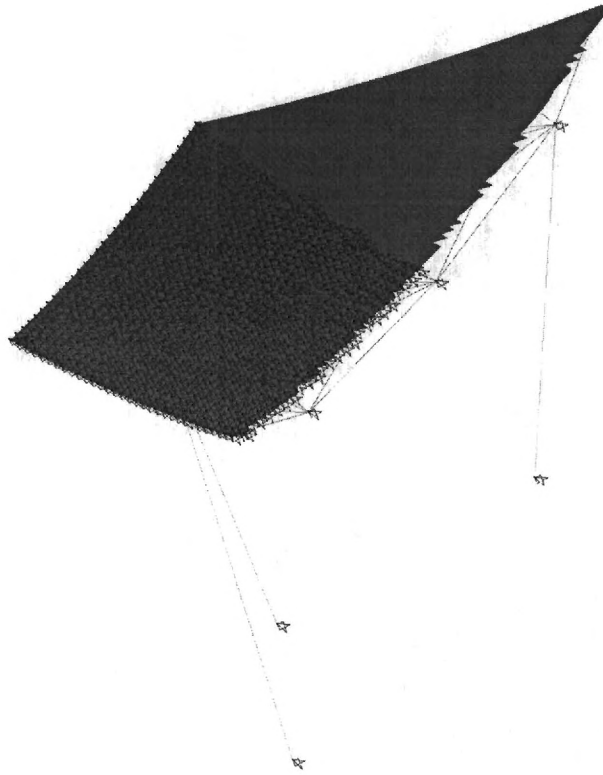


Figure 66. FEM Cross-sheet of Facesheet, Truss, and Tripod

The next section discusses the facesheet only case, followed by a discussion of the remaining cases in following sections.

## **5.2 Deformable Mirror Aberration: Negligible Substrate Structural Influence (Facesheet-Only)**

To create the facesheet-only case the rigidity of the substrate is rendered ineffective (approximately zero) by effectively removing the structural influence of the struts. To accomplish this the modulus of elasticity of the struts is reduced by a factor of  $10^{-7}$

yielding a value of about 7000 Pa, which is two orders of magnitude less than the modulus of rubber.

The spherical geometry of the facesheet (see **Error! Reference source not found.** on page **Error! Bookmark not defined.**) is used to validate the facesheet-only model. Recall that the f-number,  $f$ , is the ratio of the radius of curvature  $r_c$  to the radius of the aperture,  $\frac{a}{2}$ , and for a 4 m aperture with  $f = 1.5$  this gives  $r_c = 12$  m. If  $d$  represents the facesheet depth along the  $z$ -axis, then from **Error! Reference source not found.** the depth of the facesheet along the  $z$ -axis is

$$d = r_c - \sqrt{r_c^2 - \left(\frac{a}{2}\right)^2} \quad (30)$$

Application of a uniform thermal load causes uniform linear expansion in all directions. The increase in facesheet depth therefore is

$$\Delta d = d\Delta T\alpha \quad (31)$$

where  $\alpha$  is the coefficient of thermal expansion (CTE) from in Table 12 in Appendix A and found in [12]. For  $r = 12$  m, the depth of the mirror is  $d = 0.1678$  m which yields a change in depth of 22  $\mu\text{m}$ . This is consistent with a result in [12].

Figure 67 shows a contour plot of the net deformation of a 4 m aperture facesheet due to a 10°C uniform thermal load (note that models in Sections 5.3 – 5.6 use 2 m aperture mirror where reference [12] uses the 4 m aperture). The P2V displacement along the  $z$ -axis (out of the page) is 22  $\mu\text{m}$ . The low point (dead center) is -328 mm and the high point of -308 m is located at the vertices. The negative

displacements are caused by radial facesheet expansion and the subsequent outward movement of the tripod lowering the facesheet. Note that for the case of a 2 m facesheet the analogous deformation is 11  $\mu\text{m}$ .

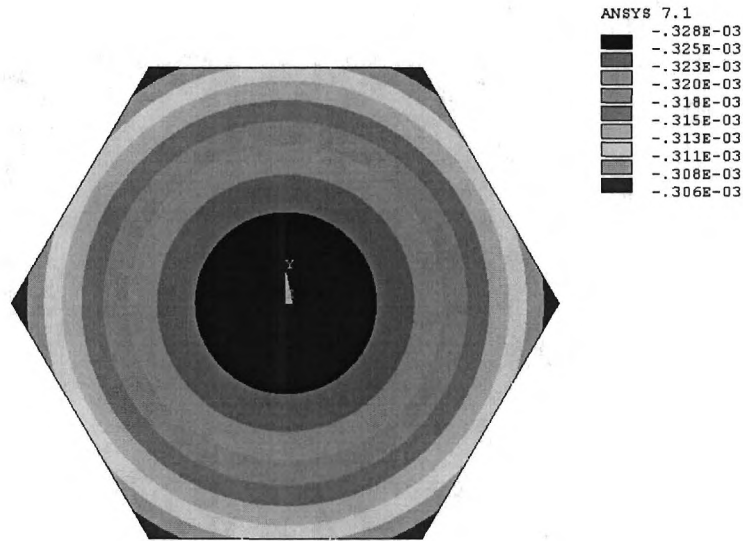


Figure 67. Facesheet-Only Simulation - 10°C Uniform Load for 4 m Aperture.

### **5.3 Deformable Mirror Aberration: Comparison of Matched and Mismatched CTE cases.**

The substrate restrains facesheet expansion and in Section 5.1 this was eliminated by decreasing the rigidity of the substrate until negligibility, thus allowing for free expansion of the facesheet. Matching the facesheet and substrate CTE values should also allow a similar free expansion since the entire system would respond monolithically. This section discusses the difference between the matched and mismatched CTE cases. It also shows that in the linear gradient case, even for matched CTE, the struts partially restrain the facesheet.

Contour plots in Figure 68 and Figure 69 show the stark difference between matched and mismatched CTE values for 159 actuators and a 10°C uniform thermal

load. The matching facesheet-substrate CTE case (Figure 68a) resembles the facesheet-only deformation (Figure 67). The P2V deflection between (a) and (b) in Figure 68 differ significantly ( $11\ \mu\text{m}$  vs.  $475\ \mu\text{m}$ ). In the zero CTE substrate case (Figure 68b) the print-through of the substrate onto the mirror surface is visually apparent in comparison with the rest of the surface.

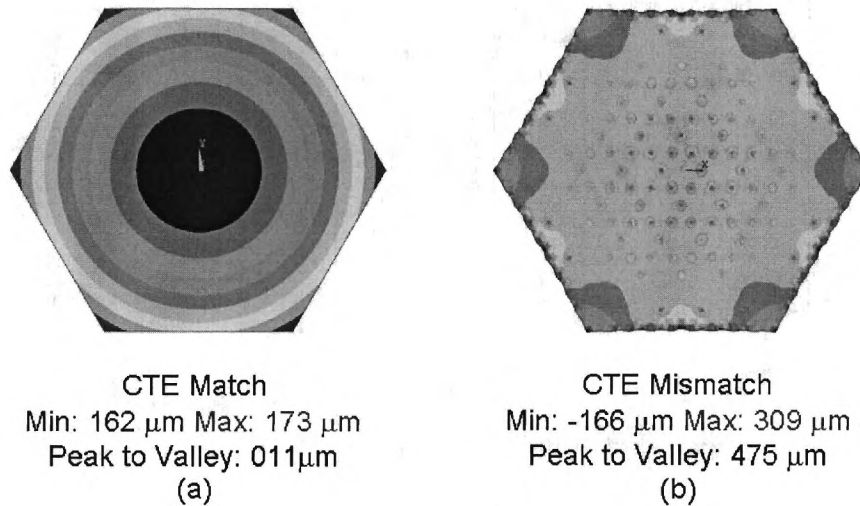


Figure 68. Comparison of CTE Match/Mismatch: 159 Actuators -  $10^\circ\text{C}$ .

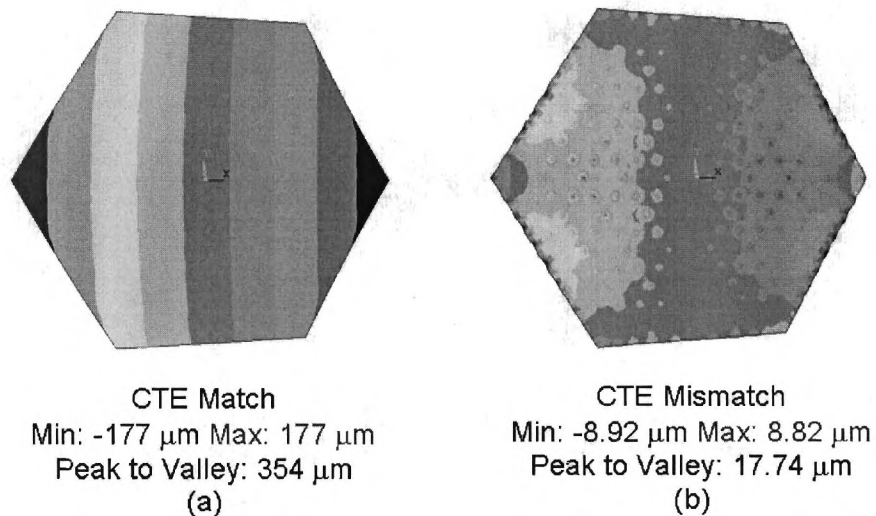


Figure 69. Comparison of CTE Match/Mismatch: 159 Actuators -  $1^\circ\text{C/m}$ .

Figure 69 shows that P2V deflection differs significantly between the mismatched and matched CTE cases ( $354\ \mu\text{m}$  vs.  $17\ \mu\text{m}$  respectively) for a  $1^\circ\text{C}/\text{m}$  gradient thermal load. Unexpectedly and as seen in the next section, for this particular loading condition the matched facesheet and substrate CTE case differ from the facesheet-only case (Figure 69a vs. Figure 70).

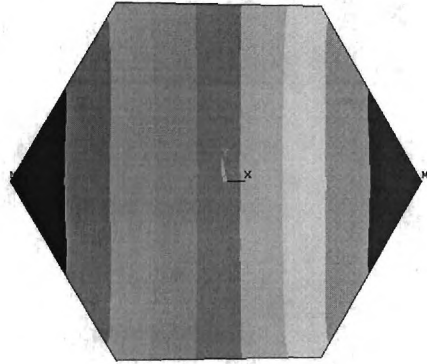


Figure 70. Facesheet-Only Simulation -  $1^\circ\text{C}/\text{m}$  Uniform Load for 2 m Aperture.

The deformation is not linear across the surface in Figure 69a, as in Figure 70. The deformation gradient (oriented left to right across the surface) curves horizontally. This is indicative of the truss constraining the mirror. This indicates that in the presence of a thermal gradient, a closely matched CTE will limit, but *may not* entirely eliminate, thermal deformation due to remaining mechanical interaction with the facesheet.

#### **5.4 Deformable Mirror Aberration: Zero Substrate CTE**

The facesheet is examined using a zero CTE for the substrate and an increasing number of actuators. A strut modulus of  $63.5\ \text{GPa}$  and actuator stiffness of  $2 \times 10^6\ \text{N/m}$  is used for actuator quantities ranging from 15 to 11775. The model again returns to a 2 m aperture and thermal loads of  $10^\circ\text{C}$  and  $1^\circ\text{C}/\text{m}$  are applied.

The case of zero substrate CTE is the worst case of a complete thermal mismatch between the facesheet and substrate. Print-through is abundant and the substrate distorts the facesheet considerably. The characteristics of interest are the aberration of the DM for increasing numbers of actuators, the somewhat asymptotic decrease in deflection, and the visually apparent print-through. These characteristics are illustrated in Figure 71 and Table 5 for 10°C and Figure 72 and Table 6 for thermal loading of 1°C/m. Figure 71 shows contour plots of the deformation under a 10°C uniform thermal load with 15-11775 actuators in the substrate.

Table 5 contains the P2V deformation values for each actuator case. Thermal distortion is magnified by the structural influence of the substrate since the deformation of the facesheet is one to two orders of magnitude greater than the facesheet-only case. The initial P2V deformation is 1131 mm and decreases somewhat asymptotically to 128 mm. A distinctive shape is reached as seen in Figure 71f.

Contour plots for 1°C/m in the  $x$ -direction are shown in Figure 72 for same quantities of actuators. In the facesheet-only case (Figure 72a) the facesheet deflects 431  $\mu\text{m}$  P2V. In adverse to the increase in deflection seen in the case of a 10°C uniform load, there is no increase in the P2V aberration relative to the facesheet-only case. The effect of the substrate is to decrease P2V by one to two orders of magnitude. For case of 15 actuators (Figure 72b) the deflection decreases to 61.6  $\mu\text{m}$  from 431  $\mu\text{m}$  in the facesheet-only case. Table 6 contains a complete listing of the deflection values for actuator cases shown in Figure 72. The P2V deflection for this set of loading conditions levels off at approximately 8  $\mu\text{m}$ .

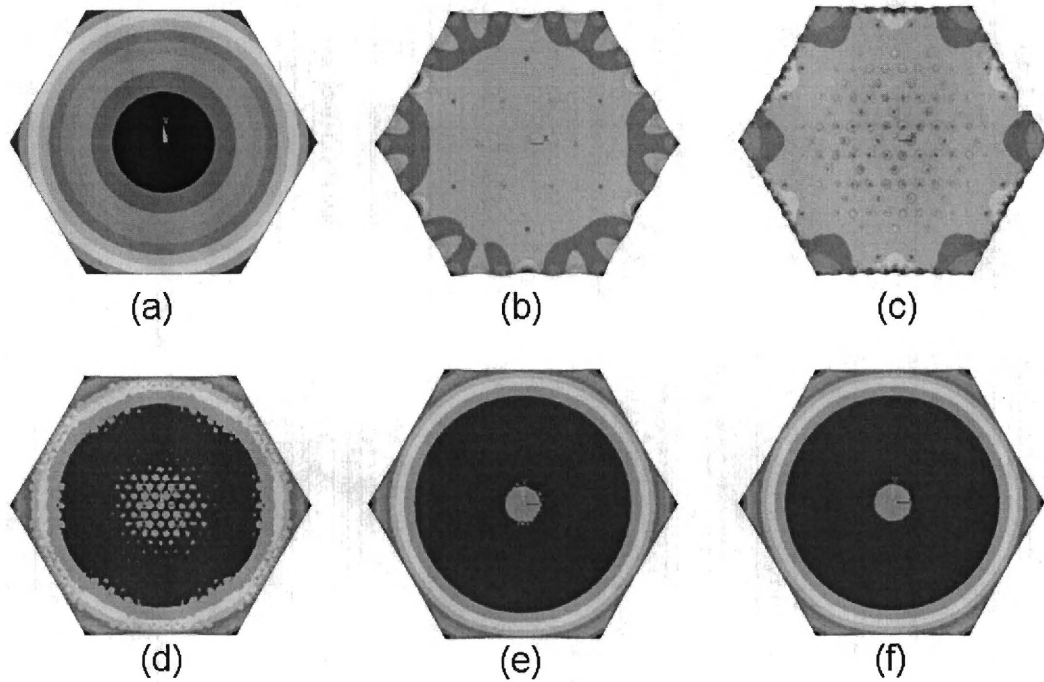


Figure 71. Mirrors with 15 to 11775 Actuators and a 10°C Uniform Thermal Load.

Table 5. Peak to Valley Deformations for the cases shown in Figure 71.

Figure Letter	Actuators	Min. $\mu\text{m}$	Max. $\mu\text{m}$	P2V $\mu\text{m}$
(a)	facesheet only			10.9
(b)	15	-630	501	1131
(c)	159	-166	309	475
(d)	1563	-64.6	79.7	144.3
(e)	5703	-51.6	76.2	127.8
(f)	11775	49.2	79.2	128.4

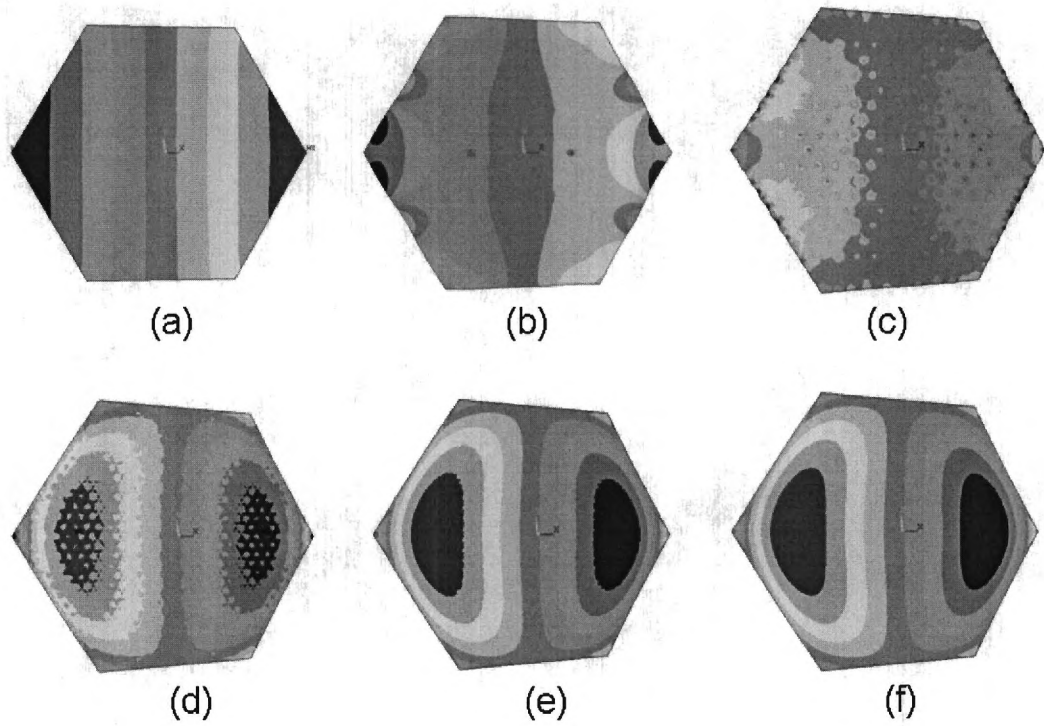


Figure 72. Mirrors with 15 to 11775 Actuators, with 1°C/m Thermal Load.

Table 6. Peak to Valley Deformations for cases shown in Figure 72.

Figure Letter	actuators	Min. $\mu\text{m}$	Max. $\mu\text{m}$	P2V $\mu\text{m}$
(a)	facesheet only			431
(b)	15	-30.9	30.7	61.6
(c)	159	-8.92	8.82	17.74
(d)	1563	-3.98	3.97	7.95
(e)	5703	-4.01	4.01	8.02
(f)	11775	-4.06	4.06	8.12

Figure 73a and Figure 73b, show a  $1^{\circ}\text{C}/\text{m}$  thermal load in the  $y$ -direction and in a  $45^{\circ}$   $x$ - $y$  direction. The  $y$ -direction is along a second axis of symmetry while the forty-five degree orientation has off axis symmetry. The deflections are in the same range as those from a  $1^{\circ}\text{C}/\text{m}$  in the  $x$ -direction. These results show that the orientation of the thermal gradient does have an effect on the deflection across the facesheet (though not much in this case).

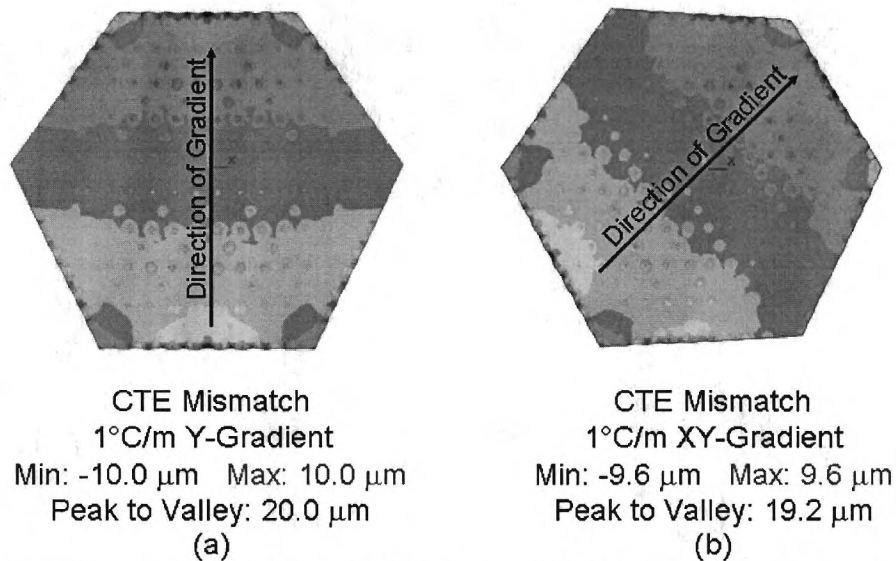


Figure 73. 159 Actuators with Mismatched CTE and  $1^{\circ}\text{C}/\text{m}$  Thermal Loads in the  $Y$  and  $XY$  directions.

In summary, the surface deflection for the case of uniform or gradient thermal loading does not vary linearly with increasing actuators but each approach an aberrated shape asymptotically. This corresponds to the idea that as the number of actuators increases the substrate becomes more like a solid two-layer material. In Chapter 6 it is shown that deformation of the mirror is tied directly to the rigidity of the substrate, and specifically to that of the truss. Based upon the results here and in

Chapter 6 it is inferred that stress induced by thermal loads increases with increasing numbers of actuators.

### **5.5 Summary of Thermal Loading**

The agreement between the cases of facesheet-only, matched CTE, and analytical calculations supports the modelling for the uniform thermal load. The 1°C/m cases for the facesheet alone and matched CTE generally agree as well. In addition, distinct differences were properly observed between the matched and mismatched CTE cases (i.e. distortion of the mirror and print-through). In both thermal loading cases an increase in the number of actuators gradually decreases the magnitude of deformation due to the thermal load.

For both thermal loading conditions the P2V deflection induced by the substrate levels off. In the case of a 1°C/m thermal load the direction across the facesheet does have a minor influence on the P2V surface deformation. However, modelling a thermal gradient in the  $x$ -direction is sufficiently representative.

The key design points in this section are:

1. The substrate acts as a mechanism around which the facesheet deforms (similar to two-layer solid material).
2. As the substrate is “thickened” by increasing the number of actuators it inhibits thermal deformation.
3. Completely matching the CTEs of the substrate and facesheet may not remove all unwanted deformations.
4. Though negligible in the case of the linear gradients ( $x$ ,  $y$ , and  $x-y$ ), orientation of the aberration does make a difference (as shown in Chapter 4).

The next chapter evaluates model linearity, actuator glitch, and force levels. It also returns to a discussion of RMS, but in terms of residual RMS error.

## CHAPTER 6

# EVALUATION OF MODEL LINEARITY, ACTUATOR GLITCH, AND FORCE LEVELS

This section focuses on three aspects of the mirror system: model linearity, the effects of actuator glitch, and the actuator force levels. 10°C uniform and 1°C/m gradient thermal loads are applied to the mirror facesheet and substrate. Coefficients of thermal expansion values are mismatched to provide a worse case differential in expansion between the facesheet and substrate. Each set of loading conditions is evaluated for increasing orders of magnitude of actuators (15, 159, and 1563).

### **6.1 Numerical (FEM) Verification of Linearity**

In previous sections (specifically Chapter 4) it was assumed that if the deformation mirror could accurately reproduce a facesheet aberration (in terms of Zernike modes) then it could correct that same aberration by reversing the actuator strokes. This section verifies this inherent linear assumption using ANSYS and thus validates the method in Chapter 4.

Three critical steps are adjusted in this chapter: (1) thermal aberrations are applied to the deformable mirror rather than representative Zernike modes, (2) a least squares fit determines the actuator strokes that best remove the aberration, and (3) the actuator strokes are fed back into the FEM model for verification. Previously these actuator strokes were reintroduced into the linear equation that generated the least squares fit, while here both the reproductions (for comparison) and corrections are generated through FEM simulation. It is shown that the two methods (reproduction and correction) yield similar results in terms of RMS errors and P2V displacements.

In this chapter RMS error is referred to as *residual RMS error* to signify the error remaining after the removal of an aberration, not simply the error between an actuated and desired surface, as in Chapter 4. Also, different from Chapter 4 is that strokes are not limited to the maximum scaled value of 50  $\mu\text{m}$ , but correspond to the actual stroke required to form or correct the thermal aberration. This is relevant in section 6.3, in which the required stroke is compared to the both the JPL actuator force and stroke limitations.

Figure 74a shows a reproduction of a uniform thermal load of 10°C with 15 actuators and the residual error after correction (of that same aberration) in Figure 74b. The RMS error values remain nearly identical between the reproduction and correction. The finite element simulation does not show obvious print-through which seems to indicate that it is not a significant source of error in the correction.

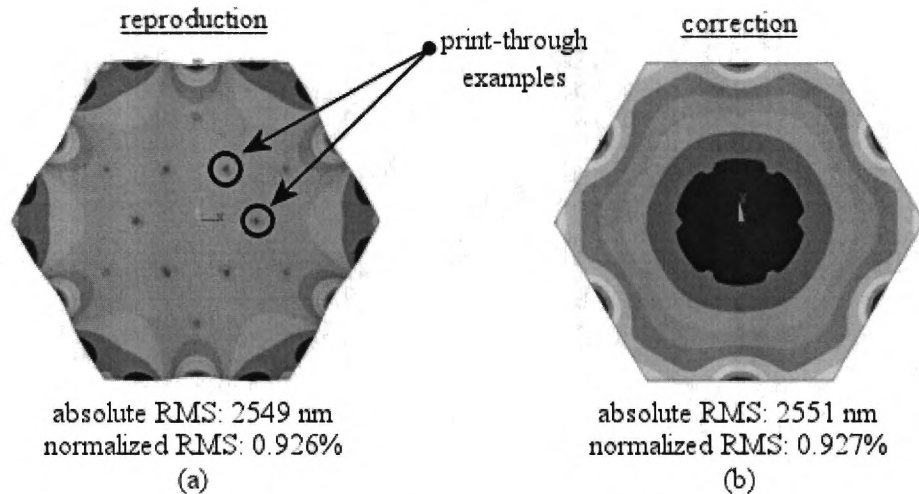


Figure 74. Reproduction vs. Correction 15 Actuators 10°C Uniform Thermal Load.

The next case (Figure 75) shows a 1°C/m  $x$ -gradient thermal load with 15 actuators, despite the exaggerated deformation in the  $y$ -direction due to an ANSYS

graphical scaling factor, it is clear that the residual RMS errors are identical to three decimal places and print-through is not observed to be a significant source of error.

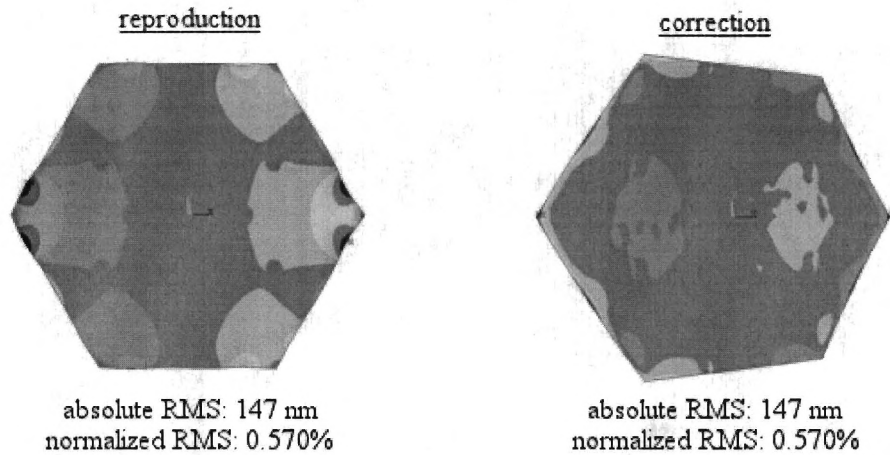


Figure 75. Reproduction vs. Correction 15 Actuators 1°C/m Thermal Load.

As the number of actuators is increased there is no significant change in the degree to which the aberration reproduction matches aberration correction. However, as shown in the uniform 10°C case with 159 actuators (Figure 76), there are signs of print-through near the center and edges of the facesheet.

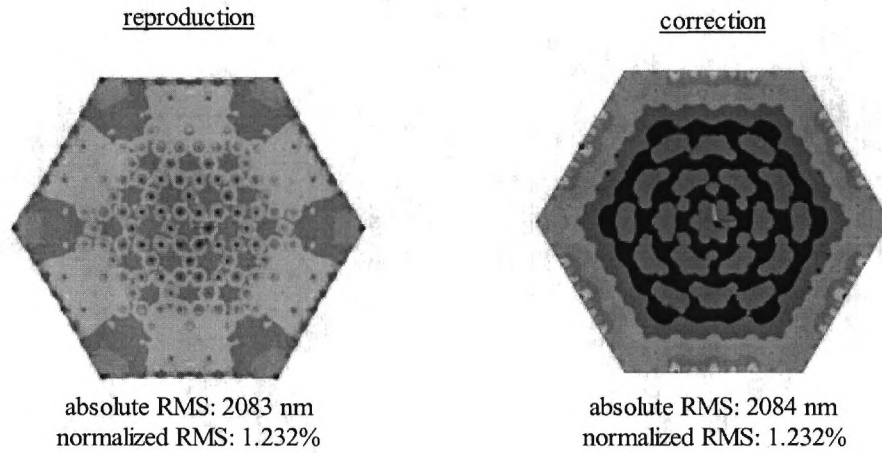


Figure 76. Reproduction vs. Correction for 159 Actuators 10°C Uniform Thermal Load.

For the case of a 1°C/m  $x$ -gradient thermal load with 159 actuators (Figure 77) that the RMS error values are still nearly identical. Localized patches of error are limited as in the 10°C, indicating that print-through is again not a significant source of error.

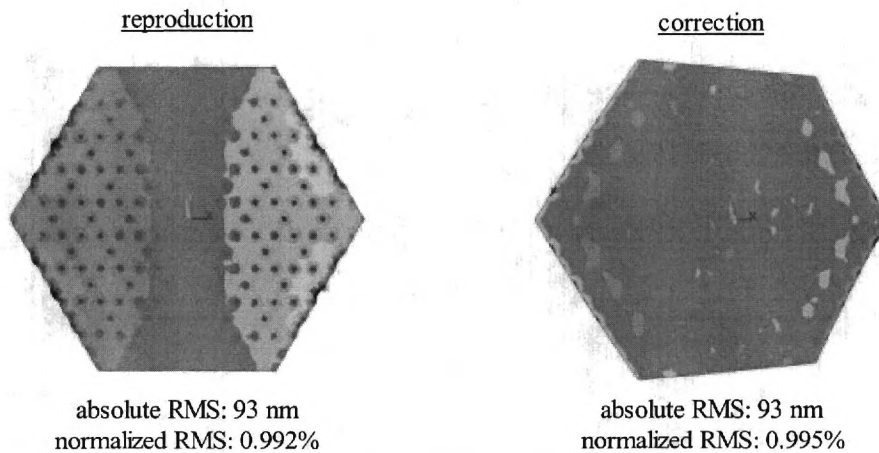


Figure 77. Reproduction vs. Correction 159 Actuators 1°C/m Thermal Load

Table 7 summarizes the results for all actuator and loading cases (including 10°C and 1°C/m with 1563). It shows that as the number of actuators is increased by two orders of magnitude the residual RMS errors for reproduction and correction remain relatively identical. It is noted that no consideration has been given to the acceptability of the RMS values, just their similarity and validation of linearity.

Table 7. Summary Reproduction vs. Correction in terms of Normalized and Absolute Error for 15, 159, and 1563 Actuators.

	15		159		1563	
Reproduction	uniform	x-grad	uniform	x-grad	uniform	x-grad
Absolute RMS (nm)	2549	147	2083	93	341	40
RMS (%)	0.926%	0.570%	1.232%	0.992%	0.127%	1.203%

	15		159		1563	
Correction	uniform	x-grad	uniform	x-grad	uniform	x-grad
Absolute RMS (nm)	2551	147	2084	93	342	40
RMS (%)	0.927%	0.570%	1.232%	0.995%	0.127%	1.204%

## 6.2 Actuator Glitch

Actuator glitch is a deviation in the final actuator position. In this section the effects of actuator uncertainty (glitch) are evaluated by application of a discrete or random glitch to the final position of the actuators. In the discrete glitch case actuator displacements are rounded to the nearest 50 nm. In the random glitch case a displacement between plus and minus 50 nm is added to each actuator.

The results suggest that RMS error is not sensitive to small glitches for the large 10°C and 1°C/m aberrations used in this study. However, despite that relative insensitivity actuator glitch is a significant source of error when compared to the possible operational spectrum of the mirror.

Figure 78 shows a representative case of random glitch applied to an otherwise unloaded facesheet and substrate with 15 actuators.

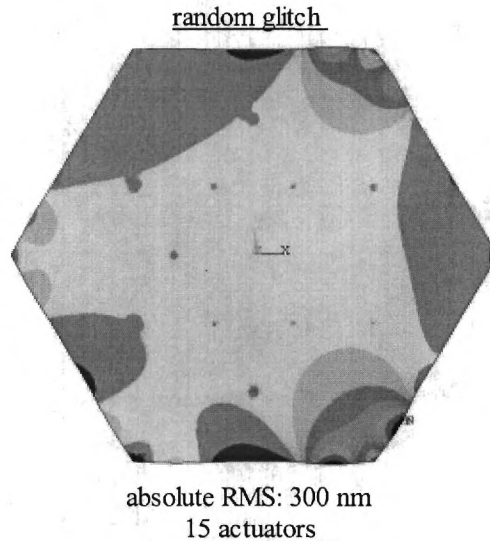


Figure 78. Random glitch applied to an unloaded facesheet (15 Actuators).

The RMS 300 nm residual error would affect telescope operation in the visible and near-infrared spectrum, essentially everything less than 6000 nm wavelength (assuming the 300 nm is  $1/20^{\text{th}}$  of a wavelength).

The absolute RMS error induced by a random glitch is about a 190 nm in the 159 actuator case (Figure 79a). While the RMS error is significantly less it is still not acceptable for the visible light range (between 20-40 nm). The value again limits use of the mirror to the mid- to far-infrared range. This is illustrated in Figure 80.

Though increasing actuators lessens the effect of glitches it is debatable whether the reduction is worthwhile as it is at the expense of increasing the rigidity and weight of the deformable mirror. The rigidity of the substrate is discussed in Section 6.3.

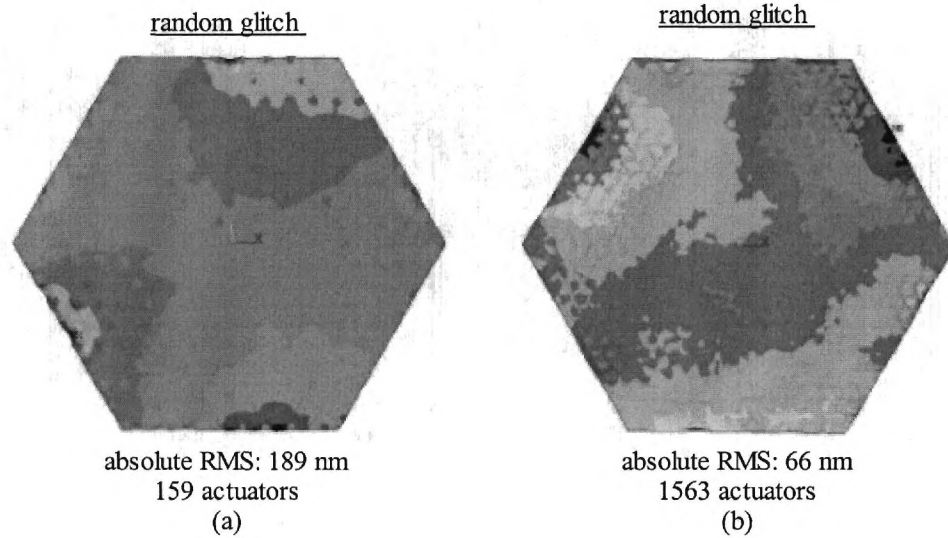


Figure 79. Random Glitch applied to a Unloaded Mirror (a) 159 and (b) 1563 Actuators.

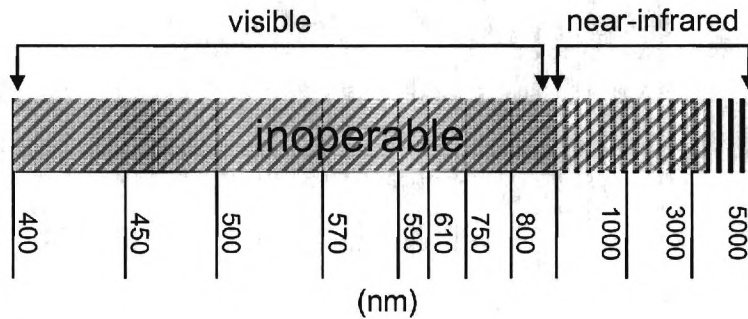


Figure 80: Visible Spectrum Exclude from Operation by Random Glitch - 159 Actuators

The 1563 actuators case with random glitch (Figure 79b) yields a deformation of 66 nm. This value still excludes visible light and a portion of the near-infrared region and is illustrated in Figure 81. Localized aberration, print-through, of the mirror is highly visible.

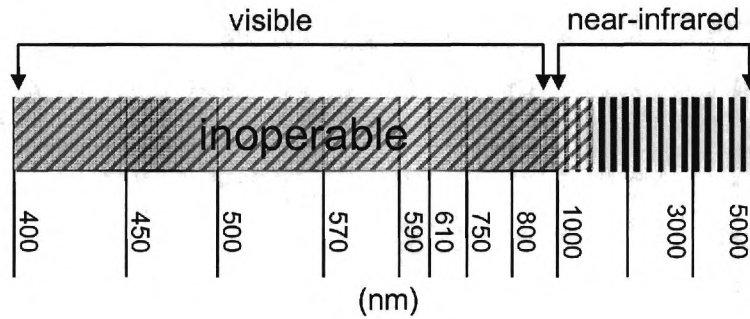


Figure 81: Depiction of Spectrum Excluded by Random Glitch (1563 Actuators)

In the next few figures random and discrete glitches are induced in the aberration removal process, and compared to the non-glitch case for 15, 159, and 1563 actuators. In Figure 82 a uniform thermal load of 10°C is applied to a 15 actuator model. The residual errors are identical to within a few thousandths of a percent between all cases.

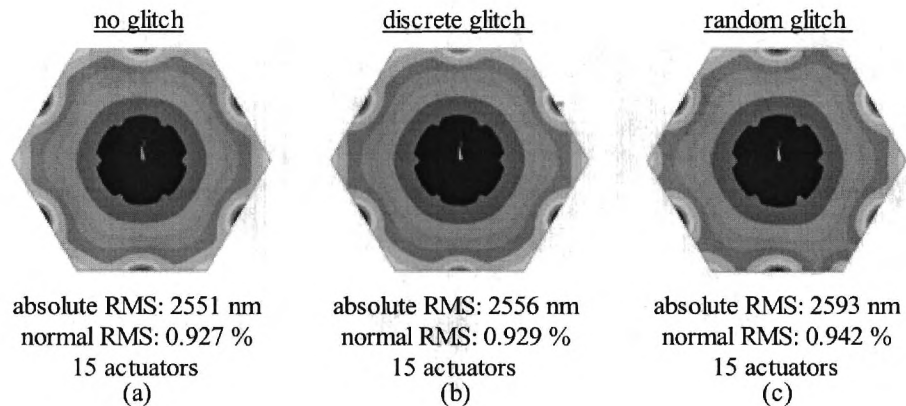


Figure 82. Discrete vs. Random Glitch – 15 Actuators 10°C Thermal Load.

The results do not differ much as the number of actuators increases (Figure 83 and Figure 84), which contains contour plots for 159 and 1563 actuators.

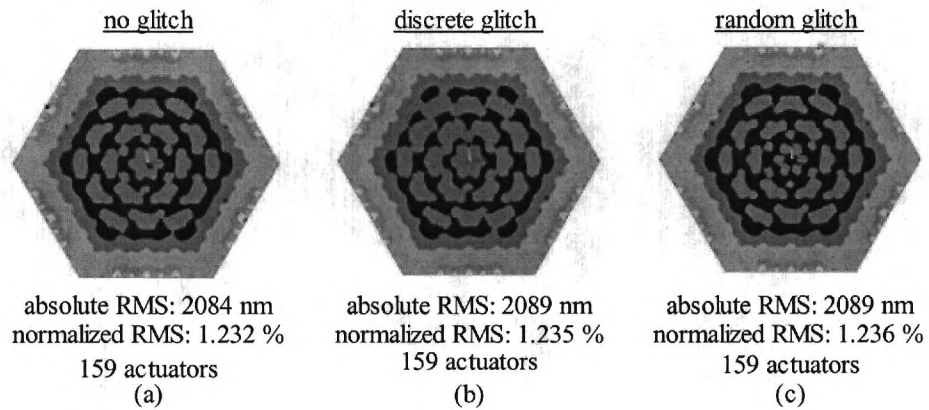


Figure 83. Discrete vs. Random Glitch – 159 Actuators 10°C Thermal Load.

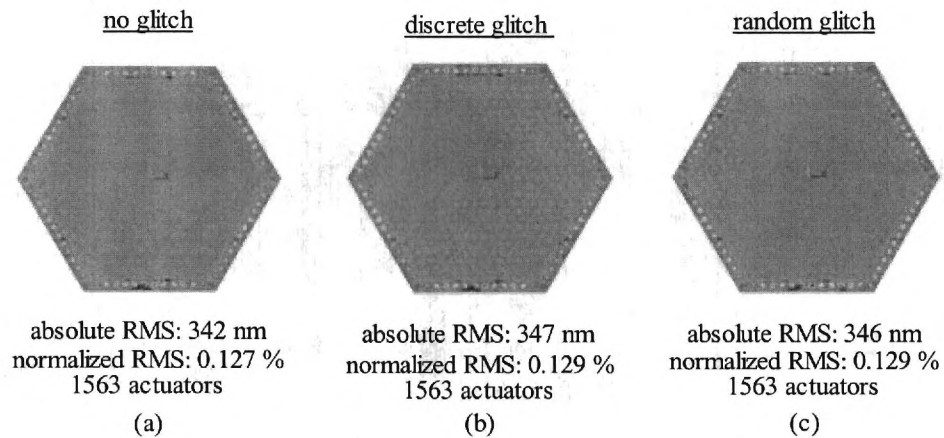


Figure 84. Discrete vs. Random Glitch – 1563 Actuators 10°C Thermal Load.

For a 1°C/m gradient in the  $x$ -direction and 15 actuators the RMS error varies somewhat (Figure 85). As the number of actuators increase, the accuracy of the correction increases by a few hundred nanometers, staying below 2.0%.

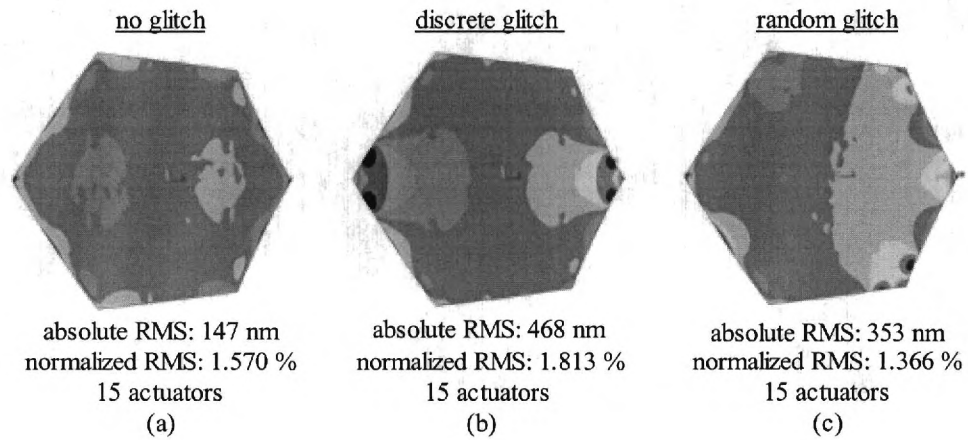


Figure 85. Discrete vs. Random Glitch – 15 Actuators 1°C/m Thermal Load.

For 159 actuators the absolute residual RMS error increases up to almost 3% (Figure 86). While the overall correction is affected very little in terms of a residual percentage of error, the error that remains is physically significant. Similar results are seen in the 1563 case shown in Figure 87.

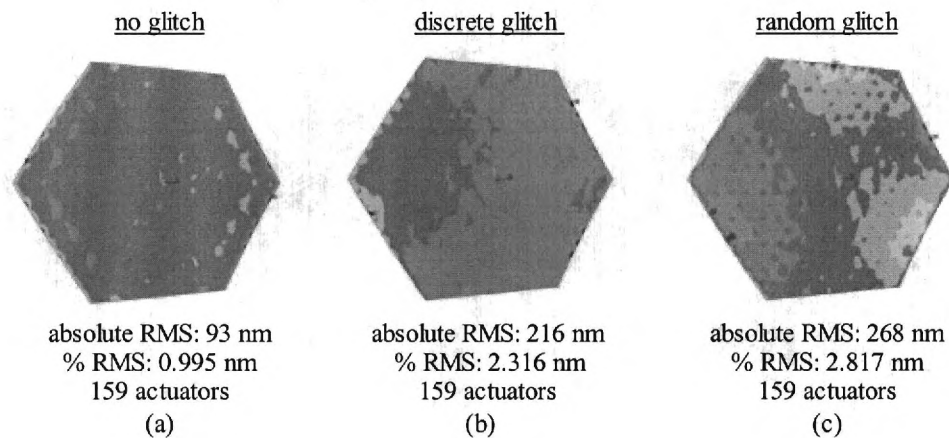


Figure 86. Discrete vs. Random Glitch – 159 Actuators 1°C/m Thermal Load.

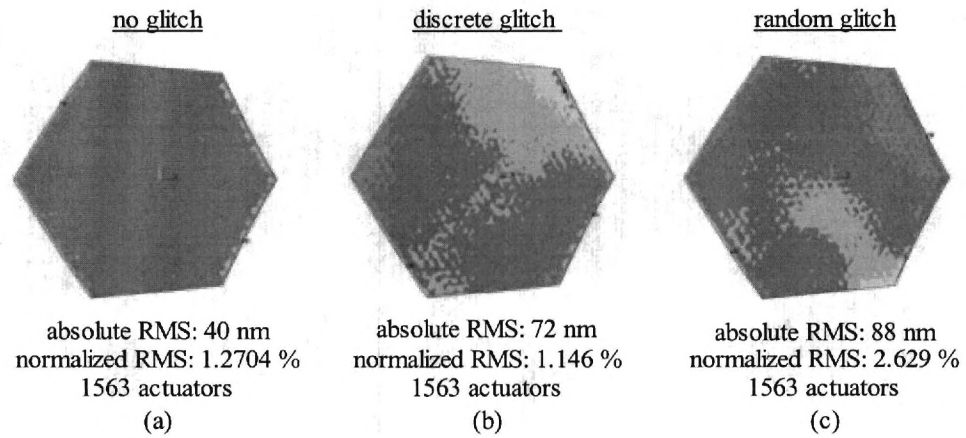


Figure 87. Discrete vs. Random Glitch – 1563 Actuators 1°C/m Thermal Load.

In summary, neither the discrete nor random glitches are presented as worst case scenarios but as representative ones. The results suggest that glitch is germane to the feasibility of the SPA DM because the induced error is physically significant in terms of the spectrum over which it might operate.

Table 8 summaries the results for 15-1563 actuators for both glitches and both thermal loads.

Table 8. Discrete vs. Random Glitch - Comparison of RMS value for 15, 159, and 1563 Actuators.

<b>No Glitch</b>	<b>15</b>		<b>159</b>		<b>1563</b>	
	<b>uniform</b>	<b>x-grad</b>	<b>uniform</b>	<b>x-grad</b>	<b>uniform</b>	<b>x-grad</b>
<b>Absolute RMS Error (nm)</b>	2551	147	2084	93	342	40
<b>RMS Error (%)</b>	0.926%	0.570%	1.232%	0.995%	0.127%	1.204%
<b>Glitch/Max Stroke (%)</b>	0.07%	1.47%	0.15%	2.00%	0.24%	1.79%

<b>Discrete Glitch</b>	<b>15</b>		<b>159</b>		<b>1563</b>	
	<b>uniform</b>	<b>x-grad</b>	<b>uniform</b>	<b>x-grad</b>	<b>uniform</b>	<b>x-grad</b>
<b>Absolute RMS Error (nm)</b>	2556	468	2089	216	347	72
<b>RMS Error (%)</b>	0.929%	1.813%	1.235%	2.316%	0.129%	2.146%
<b>Additional RMS Error (%)</b>	0.00%	1.24%	0.00%	1.32%	0.00%	0.94%

<b>Random Glitch</b>	<b>15</b>		<b>159</b>		<b>1563</b>	
	<b>uniform</b>	<b>x-grad</b>	<b>uniform</b>	<b>x-grad</b>	<b>uniform</b>	<b>x-grad</b>
<b>Absolute RMS Error (nm)</b>	2593	353	2089	268	346	88
<b>RMS Error (%)</b>	0.942%	1.366%	1.236%	2.871%	0.129%	2.629%
<b>Additional RMS Error (%)</b>	0.02%	0.80%	0.00%	1.88%	0.00%	1.42%

The effect of the discrete glitch does not differ significantly from that of the random glitch. The additional RMS errors induced by the glitches are less than 2 % in all cases. Even so, the additional RMS error is enough to make the deformable mirror inoperable over a significant portion of the spectrum. Thus, actuator glitch must be minimized and included as part of the error budget.

A significant difference exists between the 10°C uniform and 1°C/m thermal loading cases. The glitch has a greater effect in the case of the 1°C/m thermal gradient. The uniform loading case experiences an increase in additional RMS error of no more than 3/10 %, while the *x*-gradient case experiences about 1-2 %. Referring to Chapter 5, from Table 5 and Table 6 the aberration caused by the 1°C/m load is much less than that caused by the uniform 10°C load. Thus, actuator glitch should affect the 1°C/m linear gradient case more.

As might be expected from the previous non-thermally loaded cases, the presence of glitches is capable of pushing the residual RMS error beyond the acceptable level for observations in the visible light spectrum. This is seen most apparently in the cases of 159 and 1563 actuators with a 1°C/m *x*-grad thermal load. The no glitch case yields 93 nm and 40 nm of residual error respectively. For the

discrete cases 216 nm and 72 nm are yielded respectively and for the random cases 268 nm and 88 nm. All of these values preclude operation in significant portions of the visible spectrum. For further reference,

Table 9 lists the absolute RMS error and the corresponding cut-off wavelength below which the telescope would not operate based on the  $1/20^{\text{th}}$  requirement for the  $1^{\circ}\text{C}/\text{m}$  thermal load.

Table 9. Residual RMS Error and Operable Cut-off Wavelength.

1°C/m Thermal Load	absolute residual RMS (nm)		operable wavelength cut-off (nm)	
	Number of Actuators	159	1563	159
No Glitch	93	40	1860	800
Discrete	216	72	4320	1440
Random	268	88	5360	1760

### 6.3 Actuator Forces and Stroke Levels

Section 4.3 showed that for increasing numbers of actuators the RMS error could be reduced significantly. However, no consideration was given to the required actuator force. Here the forces levels are analyzed for increasing numbers of actuators. Results indicate that for high numbers of actuators with the baseline substrate the required force exceeds the maximum 0.1 N available from the suggested JPL inch worm actuators. Despite the low force output the actuator is capable of large displacements ( $\pm 250 \mu\text{m}$ ). Subsequently, a substrate with reduced rigidity is tried and shown to greatly improve loading conditions as well as reduce absolute RMS error levels.

For the baseline 68.3 GPa strut modulus and a 10°C thermal load, the 15 actuator case is the one for which the force levels are less the 0.1 N limit (Figure 88). The maximum required stroke is reasonable based on the JPL actuator stroke limit. While the residual RMS % error is only 0.9% the absolute RMS error (2550 nm) is unacceptable.

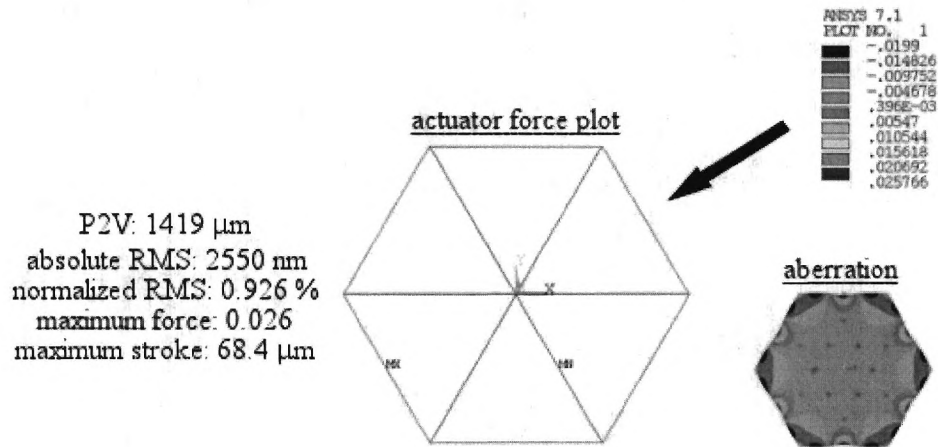


Figure 88. Actuator Force Plot for 15 Actuators 10°C - Thermal Load.

Figure 89 show the 159 actuator case, in which the maximum required actuator stroke to correct the aberration is halved for order of magnitude increase in number of actuators, going from 68.4  $\mu\text{m}$  to 32.9  $\mu\text{m}$ . While the RMS error improves with 159 actuators the force levels increase by four orders of magnitude. Generally, increases in force levels, decreases in residual RMS error, and decreases in maximum required actuator stroke are evident through the 15, 45, 93, 159, and 1563 actuators cases. The values for all cases are summarized in Table 10.

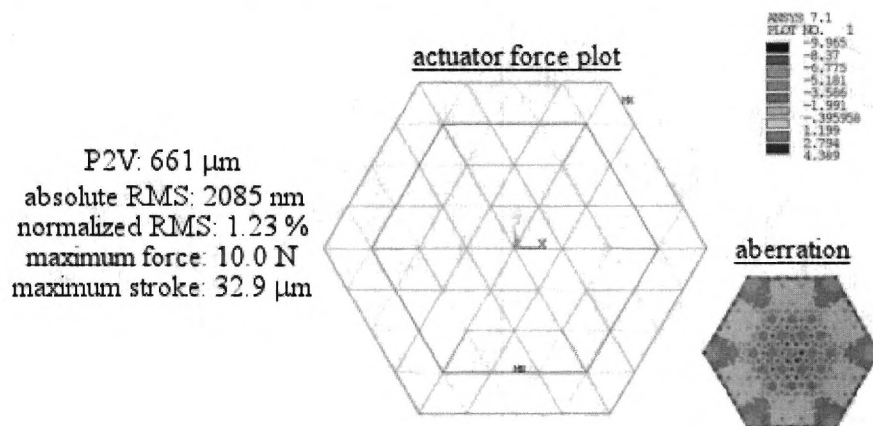


Figure 89. Actuator Force Plot for 159 Actuators 10°C - Thermal Load.

For a gradient load in the  $x$  direction (Figure 90) the facesheet deflection is much less than for the uniform thermal load as is the RMS error. Consequently the actuator stroke and force requirements are also lower.

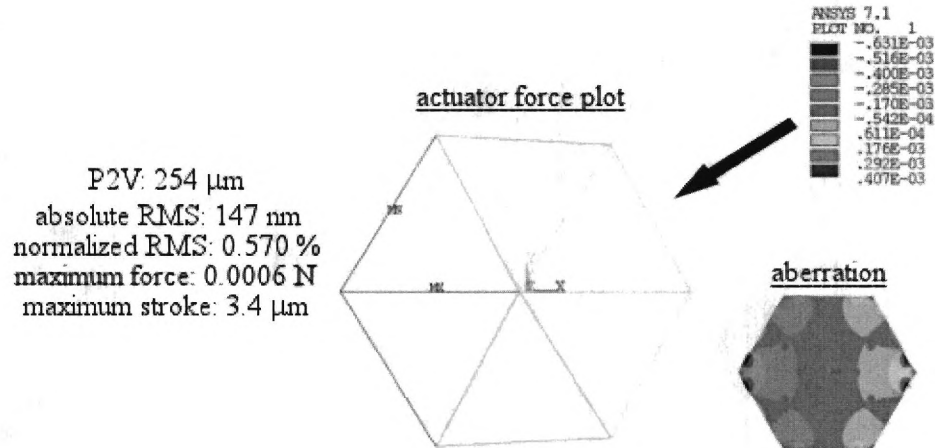


Figure 90. Actuator Force Plot for 15 Actuators -  $1^\circ\text{C}/\text{m}$  Thermal Load.

Increasing the number of actuators by an order of magnitude significantly reduces the P2V and RMS error (Figure 91). The force requirements exceed the JPL actuator limit but are still low. Stroke requirements are low as well. Table 10 also summarizes these force results.

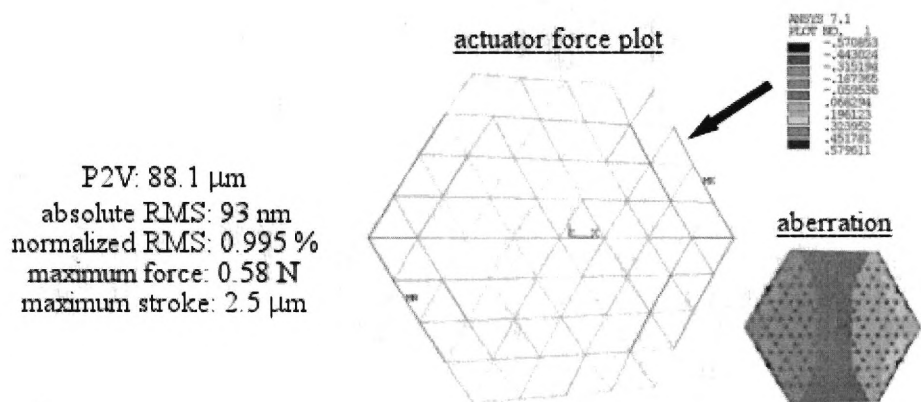


Figure 91. Actuator Force Plot for 159 Actuators -  $1^\circ\text{C}/\text{m}$  Thermal Load.

The observable trends are: (1) as the number of actuators increase the RMS values decrease, (2) the P2V and maximum stroke values increase, and (3) for both the uniform and gradient loading cases force levels increase significantly. Only the fifteen actuator case meets the actuator criteria thus far set forth by the JPL actuator specifications. Table 10 shows the cut-off wavelength below which the mirror would be unable to operate. Accordingly, only actuators of quantities greater than 1500 would operate in the visible light spectrum.

Table 10. Performance Values for Representative Thermal Loads, 15-1563 Actuators, and Stiffness of 68.3 GPa.

Uniform 10°C Thermal Load	Number of Actuators				
	15	45	93	159	1563
P2V ( $\mu\text{m}$ )	1419	592	651	661	654
Absolute RMS (nm)	2550	2482	2329	2085	342
Cut-Off Wavelength (nm)	51000	49640	46580	41700	6840
Normalized RMS (%)	0.926	4.72	2.03	1.23	0.127
Max. Actuator Force (N)	0.026	3.09	6.92	10.0	23.0
Max. Stroke ( $\mu\text{m}$ )	68.4	49.3	38.8	32.9	20.8

1°C/m Thermal Load	Number of Actuators				
	15	45	93	159	1563
P2V ( $\mu\text{m}$ )	254	283	170.7	88.1	16.1
Absolute RMS (nm)	147	121	106	93	40
Cut-Off Wavelength (nm)	2940	2420	2120	1860	800
Normalized RMS (%)	0.570	0.635	0.763	0.995	1.204
Max. Actuator Force (N)	0.0006	0.347	0.469	0.58	4.9
Max. Stroke ( $\mu\text{m}$ )	3.4	3.45	2.98	2.5	2.8

The actuator forces are likely related to the combined stiffness matrix of the mirror and a question of optimization arises: with more control points (actuators) the accuracy of the truss is increased; however the rigidity is also increased and therefore,

is there an optimal number of actuators for a given stiffness? Can the truss parameters be optimized to decrease the stiffness of the mirror, while maintaining the RMS, P2V, and force values? Though optimization would be subject of future work however, one parameter can be easily adjusted to show the likely affect of an optimization, specifically the substrate or strut stiffness.

In earlier chapters it was shown that the substrate causes significant deformation of the facesheet. Furthermore, as the number of actuators is increased the deflection for given thermal load is decreased. This implies that the mirror system “stiffens” to the effects of the thermal load. Thus, a logical next step is to relax the substrate. This can not be achieved by adjusting the actuator stiffness since it merely increases the required actuator displacements.

Instead the substrate is relaxed by lowered by decreasing the modulus of the struts. For contrast, the modulus is lowered by a factor of three orders of magnitude to 68.3 MPa which is equivalent to a material change from aluminium to rubber. This decreases the deformation of the facesheet and significantly lowers the corrective force required of the actuators (

Table 11).

Table 11. Performance Values for Representative Thermal Loads, 15-1563 Actuators, and Stiffness of 68.3 MPa.

Uniform 10°C Thermal Load	Number of Actuators				
	15	45	93	159	1563
P2V ( $\mu\text{m}$ )	511	419	379	332	238
Absolute RMS (nm)	2500	2476	2418	2281	487
Cut-Off Wavelength (nm)	50000	49580	48360	45620	9740
Normalized RMS (%)	1.63	6.8	5.33	3.3	0.5
Max. Actuator Force (N)	.003	.030	.075	.217	.825
Max. Stroke ( $\mu\text{m}$ )	15.3	5.9	4.0	3.43	1.62

1°C/m Thermal Load	Number of Actuators				
	15	45	93	159	1563
P2V ( $\mu\text{m}$ )	43.2	26.6	19.1	14.7	9.8
Absolute RMS (nm)	138	129	128	120	48.9
Cut-Off Wavelength (nm)	2760	2580	2560	2400	978
Normalized RMS (%)	2.0	5.6	9.0	8.3	2.5
Max. Actuator Force (N)	.0002	.002	.004	.013	.033
Max. Stroke ( $\mu\text{m}$ )	10	4.5	2.7	2.3	0.9

In doing this, the normalized and *absolute RMS* error is increased slightly for higher numbers of actuators in comparison to the results in Table 10. For lower numbers of actuators it remains virtually the same in terms of absolute RMS. The required stroke is in fact decreasing the rigidity of the substrate. Force levels are reduced such that for 1°C/m all cases (15-1563) meet the force constraints of the JPL actuators. For a 10°C uniform load that requirement is met up to 93 actuators. In the 1563 actuators case for both thermal loads, the RMS is error is still exclusive of the visible light range with a value 48.9 nm for the 1°C/m case and 487 nm in the uniform 10°C case. Thus, it can be concluded that by decreasing the stiffness further, and judiciously increasing the number of actuators that feasibility, over the entire visible to near infrared spectrum may be achieved.

## **6.4 Summary**

The

results

of

Table 11 are very promising when compared to the initial results of Table 10. These lend to the eventual successful use of the JPL actuators if truss flexibility can be increased and if the actuator force capability can be increased slightly. More importantly, the conclusion is drawn that for an optimization of the truss parameters, the entire visible spectrum and near-infrared can be operated upon by this deformable mirror technology.

The summary points for this chapter are:

1. The SPA deformable mirror is linear for small deformations.
2. Actuator glitch has the potential to significantly disturb image clarity and therefore must be accounted for in the error budget.
3. As the number of actuators increase so to do the force requirements for a given thermal aberration.
4. Decreasing the rigidity of the substrate, and specifically, the modulus of the strut, decreases the magnitude of the thermal aberrations and the forces required to negate them.
5. For both  $10^{\circ}\text{C}$  and  $1^{\circ}\text{C}/\text{m}$  thermal loads the absolute residual RMS error decreases for a less rigid substrate.
6. Correction of the given aberrations does not even come close to exceeding the maximum travel of the JPL actuators ( $\pm 250 \mu\text{m}$ ).

For uniform thermal loads a higher number of actuators greater than 1563 would be required to remove the resulting aberrations to an acceptable level for use in the visible spectrum.

## CHAPTER 7

### CONCLUSIONS

In this study tools were developed to examine the feasibility of a thin-shell deformable mirror for space-based telescopes with an adaptive truss. Performance was evaluated for varying physical parameters according to the two primary metrics of evaluation: RMS error and P2V deflection.

In Chapter 4, RMS error and P2V deflection were examined in terms of the first sixty-six Zernike modes for increasing numbers of actuators, thickness, truss-height, and print-through (qualitatively). The following conclusions were drawn based upon available data:

1. While the SPA deformable mirror (DM) does not perform equally for all Zernike modes, it is nonetheless capable of effectively removing all aberrations types.
2. The modal nature of the SPA DM indicates that parameters should be selected such that they are optimal for the modes upon which the DM will operate.
3. The truss height should be adjusted to provide optimal forces to the facesheet.

In Chapter 5, simulations were run to evaluate the performance of the deformable mirror for thermal loads of  $10^{\circ}\text{C}$  and  $1^{\circ}\text{C}/\text{m}$ . Again varying numbers of actuators were considered while evaluating the thermal loads. Recall, that the substrate acts as a mechanism around which the facesheet deforms. This deformation is shown to be a controllable function of the substrate stiffness, specifically the struts.

The following additional conclusions were drawn:

1. While the numbers of actuators can be increased to improve RMS error levels, additional actuators should be used sparingly, as it increases substrate stiffness, and decreases P2V deflection.
2. The response of the SPA DM to a thermal load is dependent upon the orientation of the load. Though this is subtly illustrated in the case of the linear gradients ( $x$ ,  $y$ , and  $x-y$ ) it is clearly supported by the Zernike results.
3. Even if, substrate and facesheet CTE could be completely matched it may not remove all unwanted deformations.

Finally, in Chapter 6 the deformable mirror was evaluated for linearity, the effects of actuator glitch, and force levels. Substrate stiffness was adjusted to show its effects on force levels and feasibility. Thus, the follow conclusions were drawn:

1. The SPA deformable mirror is a linear system, meaning that reproduction of an aberration is the same as correcting it with regard to residual RMS error.
2. Actuator glitch has the potential to significantly disturb image clarity, and therefore must be accounted for in the error budget.
3. As the number of actuators increases, so to do the forces required to correct a given thermal aberration.
4. Decreasing substrate stiffness, specifically the stiffness of the struts, decreases the magnitude of the thermal aberrations and the forces required to remove them.
5. RMS error is not invariant with regard to strut stiffness.

6. With regard to stroke limits, correction of the given aberrations does not exceed the maximum travel of the JPL.

To further summarize the Surface Parallel Actuated Deformable Mirror performs at least as well as the SNA deformable mirror, and in some cases performs better in terms of both P2V and RMS. Based upon results the SPA DM should be optimized for the application and environment for which it is selected; the SPA DM is highly modal. The numbers of actuators, truss height, thickness, and substrate stiffness are all critical parameters. Since, both the 10°C and 1°C/m cases are extreme cases of thermal loading and it is equally expected that great care would be taken to minimum difference in CTE, performance requirements could be up to 10 times less than those considered here. Considering all the previous points the SPA DM is a feasible technology.

## CHAPTER 8

### FUTURE WORK

As stated previously, there is a limited body of work discussing membrane or thin shell mirrors directly attached to and supported by an active truss network. The next step in advancing this mirror system is to increase the realism of the design and move towards a multi-segment hexagonal mirror. To move to that point the following objectives must be met:

1. Develop a realistic component level model of the mirror system: mirror, truss, joints, and actuators.
2. Develop an advanced understanding of the thermal-structural properties using representative thermal profiles.
3. Develop a more refined actuator model such as using the JPL inch worm actuators.
4. Develop a refined control/correction algorithm.
5. Optimize the mirror-system.
6. Optionally: Tie multiple mirror segments into an array.

An extensive set of library routines has been developed to support modelling and simulation of an active truss and thin-shell mirror design. These libraries are modular, adaptable, and provide a foundation for further study. Modules can be added and enhanced to provide the additional functionality necessary to bring the complete deformable mirror model to fruition. Thus, the following bullets expand on achieving the objectives above:

1. A complete component level model of the mirror system should be developed. A solid flexure connection should be created between the

mirror and struts. A padded area capable of supporting the flexure like connection modelled at the same points of connection. The ability to vary the thickness of the mirror from its center to its edge added to the model. Finally, a realistic lightweight strut should be modelled that incorporates bending loads. Each new feature would be evaluated for its affect on the correctability of the mirror.

2. Full investigation of thermal-structural properties using realistic thermal profiles is important to a successful mirror design. The effect of thermal gradients on the mirror system is a critical source of optical aberration. The effect of linear and stepwise varying gradients on each individual component could be evaluated. The mechanical properties of the deformable mirror when loaded by thermal gradients are not well understood. In-mirror circumferential stress/strain could be analyzed for its affects on correctability. Counterintuitive actuator force requirements have been observed with force levels increasing non-monotonically with increasing numbers of actuators. The stress/strain levels could be clarified as it relates to the number and placement of actuators.
3. Based on the force levels and actuator strokes from the initial analyses it is not yet determined whether short-stroke high force or long-stroke low force actuators are optimal for the mirror system. Current models account only rudimentarily for the kinematics of the piezoelectric inch-worm actuators currently under development at JPL. An actuator model that incorporates realistic stroke and force capabilities, in addition to stiffness and uncertainty must be completed. In addition,

other possible candidates should be examined for use with the deformable mirror.

4. The control algorithm of the deformable mirror is a simple least-squares fit that considers error along the optical ( $z$ -axis) of the mirror. The fit determines the actuator strokes that produce the least residual RMS error. Revision of the algorithm could consider whether correction of deformations in the  $x$  and  $y$  directions significantly decreases figure error. In addition, the optimum choice of figure restoration should be reconsidered. Revised models could consider the use of a homologous optical figure, thus providing for the next best figure. It is believed that this might yield far better results than attempts to return the mirror to its original figure.
5. An optimum configuration of the deformable mirror has not been decided upon. Excluding portability concerns, an optimized mirror-system should yield the highest correctability and the least weight for a given aperture size. Based upon those criteria the other variables of concern are the number of actuators, thickness profile, and truss geometry that require optimization. It is believed that a genetic algorithm could be of use in addressing this optimization problem.
6. Once a fully modelled and simulated deformable mirror is developed it is then necessary to consider how such a structure might be ported into space. More specifically, it is relevant to consider what advantages might be inherent to a truss based support system. The JWST's 18 segments could deploy from a folded position and it is likely that such a design could work for this primary mirror technology. However,

should a thin flexible mirror substrate become a feasible component of this design it is equally likely that some degree of collapsibility could be imparted to each mirror segment by manipulating the support truss.

The success of the SPA approach is based on the creation of a deformable mirror that is able to remove residual figure error from the mirror due to thermal or other aberration causing sources. It must do so with less aerial density than existing adaptive optics systems. Furthermore, a model with realistic thermal-structural properties must be developed if this new primary mirror type is to be properly designed. It is important that an optimal control algorithm and deformable mirror configuration be determined. This would serve to maximize correctability and minimize required force and/or stroke requirements. Once a final configuration of a deformable mirror segment is determined a means of linking multiple segments could be developed, at which point this technology becomes highly competitive among other deformable mirror technologies.

# APPENDIX A

## MATERIAL PROPERTIES

Table 12. Material Properties for Each Component.

### Material Properties of Various Mirror-Truss Components

#### Standard Strut

Modulus of Elasticity, X-Axis	ex,	6.83E+10	(LINK8)
Coefficient of Thermal Expansion	alpx,	0 or 0.000013	(LINK8)
Thermal Conductivity	kxx,	70	

#### Tripod Strut (Thermal Modeling Only)

Modulus of Elasticity, X-Axis	ex,	6.83E+10	(LINK8)
Coefficient of Thermal Expansion	alpx,	0 or 0.000013	(LINK8)
Thermal Conductivity	kxx,	70	

#### Actuator

Modulus of Elasticity, X-Axis	ex,	calculated	(LINKXXX)
Coefficient of Thermal Expansion	alpx,	0 or 0.000013	(LINKXXX)
Thermal Conductivity	kxx,	70	

#### Actuator - Tripod

Modulus of Elasticity, X-Axis	ex,	calculated	(LINKXXX)
Coefficient of Thermal Expansion	alpx,	0 or 0.000013	(LINKXXX)
Thermal Conductivity	kxx,	70	

#### Facesheet

Modulus of Elasticity, X-Axis	ex,	9.50E+10	(SHELLxxx)
Modulus of Elasticity, Y-Axis	ey,	9.50E+10	(SHELLxxx)
Modulus of Elasticity, Z-Axis	ez,	9.50E+10	(SHELLxxx)
Shear Modulus, XY-Plane	gxy,	3.50E+10	(SHELLxxx)
Shear Modulus, YZ-Plane	gyz,	3.50E+10	(SHELLxxx)
Shear Modulus, XZ-Plane	gxz,	3.50E+10	(SHELLxxx)
Poisons Ratio	nuxy,	0.35	(SHELLxxx)
Coefficient of Thermal Expansion	alpx,	1.30E-05	(SHELLxxx)
Thermal Conductivity	kxx,	70	

# APPENDIX B

## SPA AND SNA PERFORMANCE FOR HIGH ACTUATOR QUANTITIES

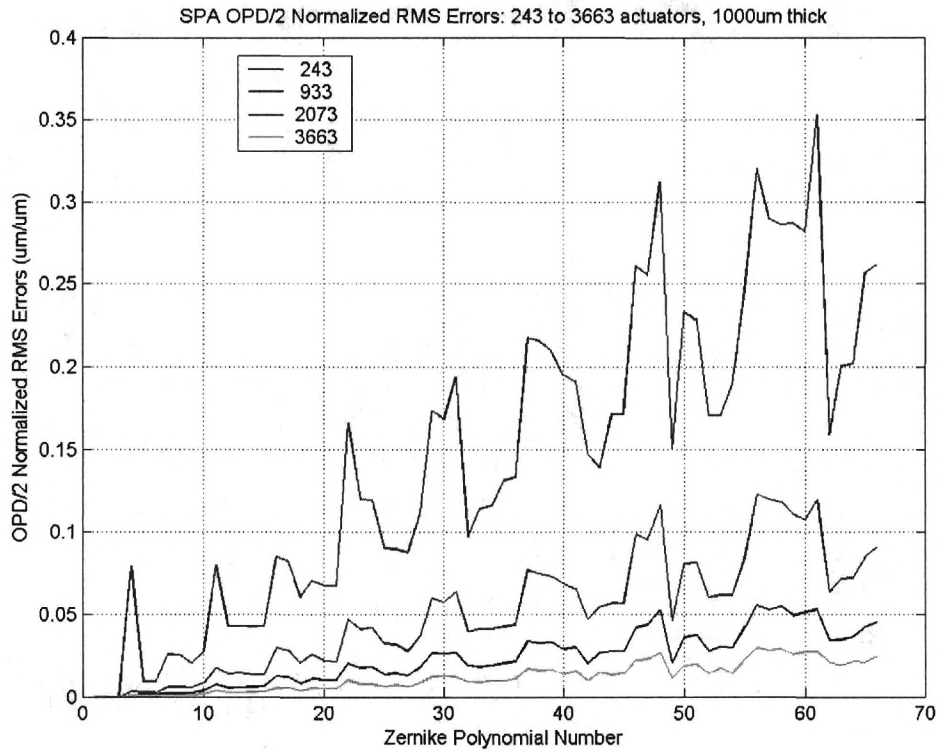


Figure 92. SNA RMS Error for 243, 933, 2073, and 3663.

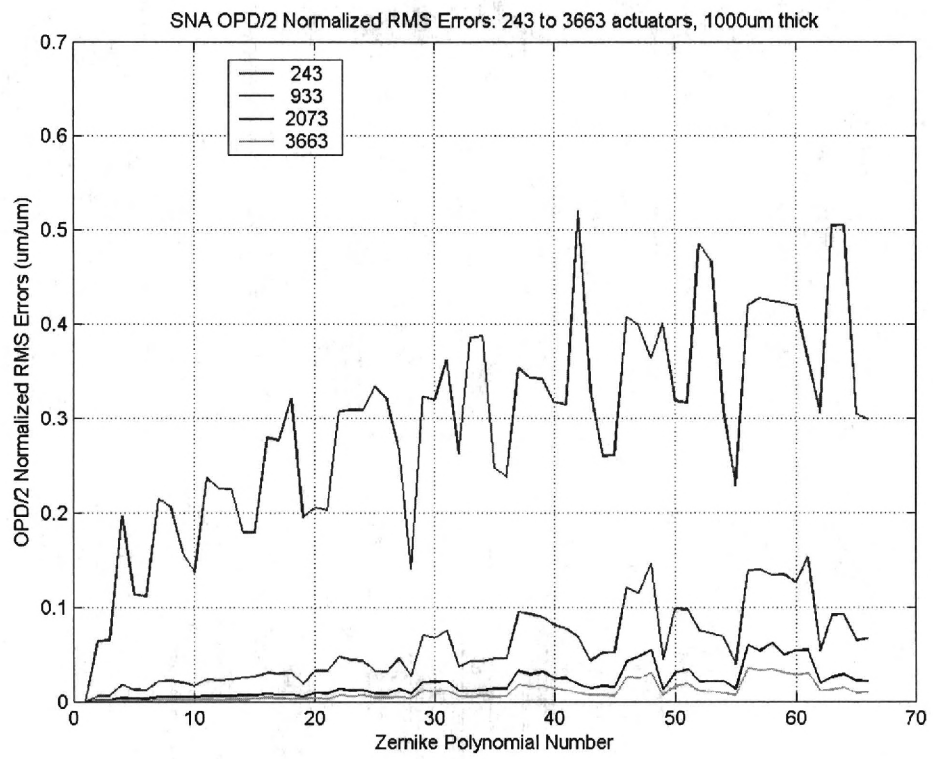


Figure 93. SNA RMS Error for 243, 933, 2073, and 3663.

# APPENDIX C

## SPA AND SNA P2V FOR LOW ACTUATOR QUANTITIES

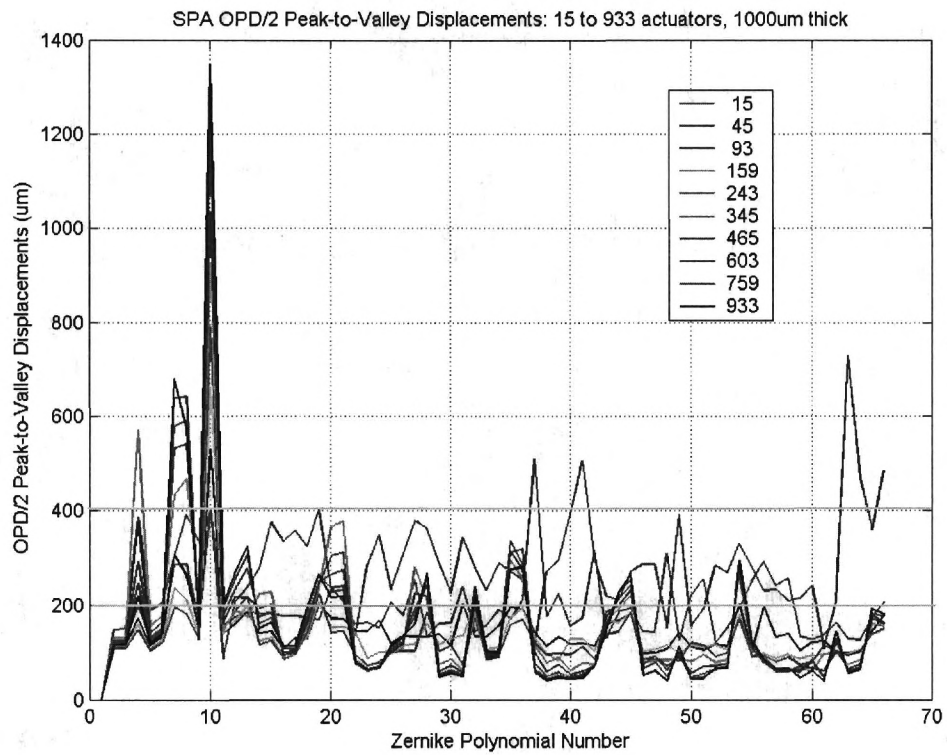


Figure 94. SPA P2V Performance for 15-933 Actuators.

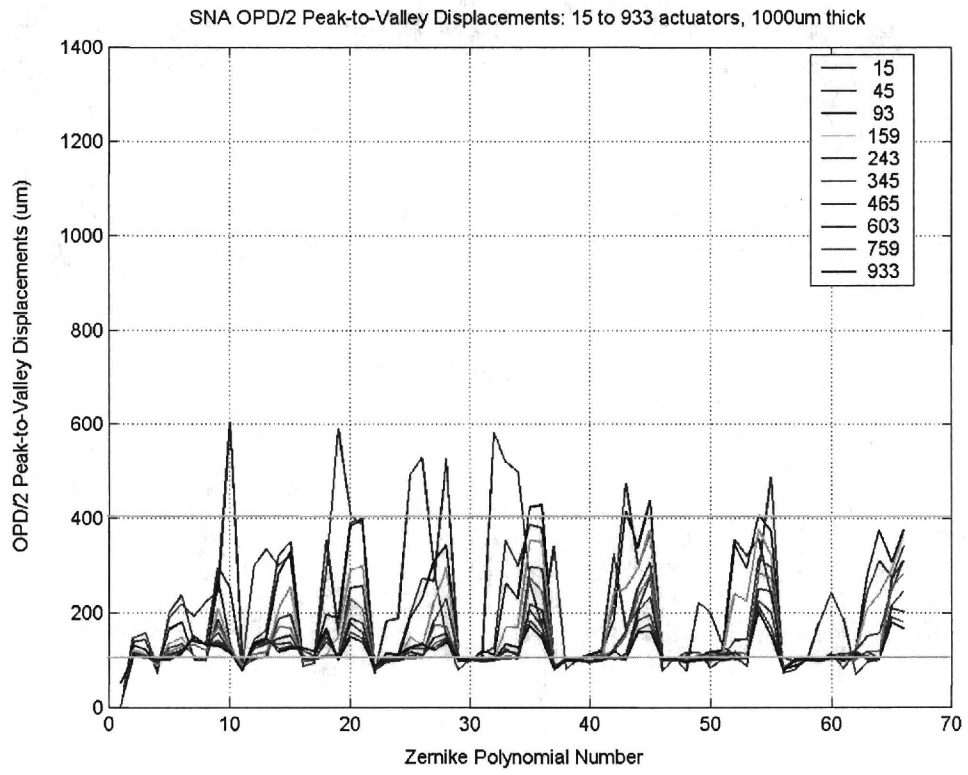


Figure 95. SNA P2V Performance for 15-933 Actuators.

# APPENDIX D

## SPA AND SNA P2V FOR VARYING TRUSS HEIGHTS

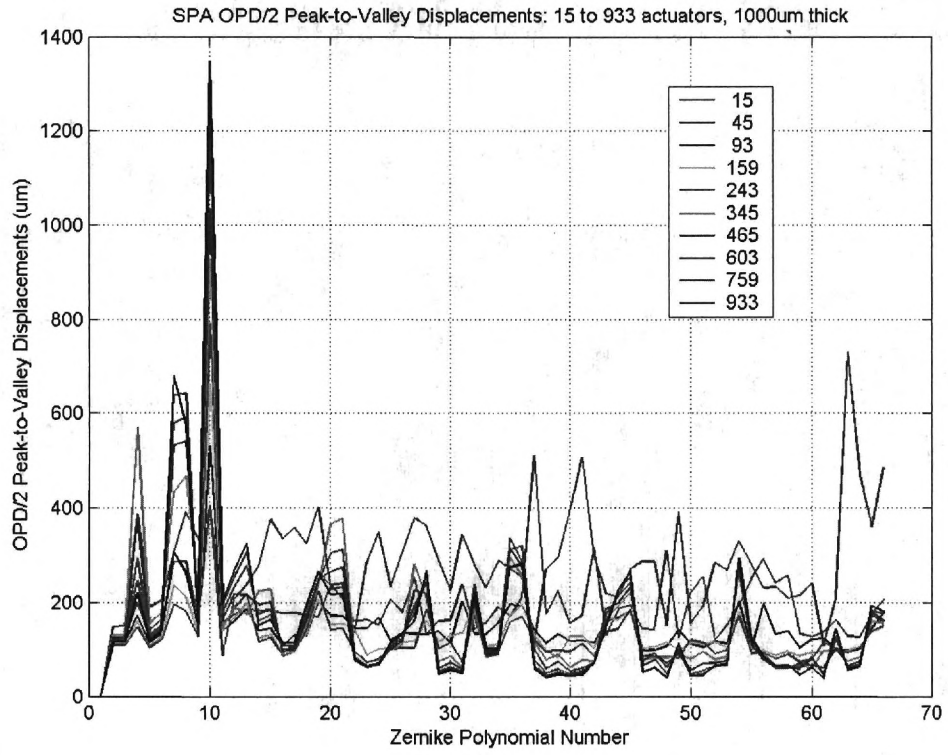


Figure 96. SPA P2V Deflection for 15- 933 Actuators for 100% Truss Height.

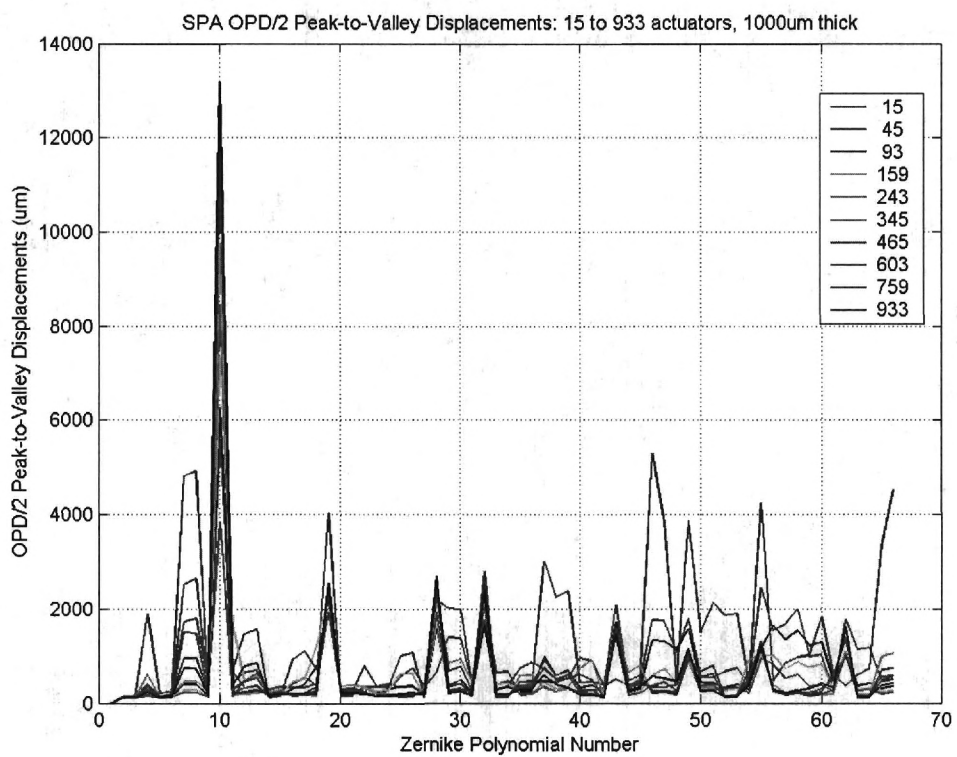


Figure 97. SPA P2V Deflection for 15- 933 Actuators for 10% Truss Height.

## REFERENCES

- [1] V. S. Krabbendam, T. Ray, F. Fowler, J., "Development and performance of Hobby Eberly Telescope 11 meter segmented mirror," presented at Advanced Technology Optical/IR Telescopes VI, Kona, HI, 1998.
- [2] F. Bash, "The Hobby-Eberly Telescope," presented at Instrumentation and Measurement Technology Conference, IMTC/99, Proceedings of the 16th IEEE, Venice, Italy, 1999.
- [3] B. D. Seery, "The James Webb Space Telescope (JWST): Hubble's Scientific and Technological Successor," presented at IR Space Telescopes and Instruments, Waikoloa, HI., 2003.
- [4] STAFF, "W.M. Keck Observatory." <http://www.keckobservatory.org/>.
- [5] P. B. Dierickx, J. Delabre, B. Ferrari, M. Gilmozzi, R. Hubin, N., "The Optics of the OWL 100-M Adaptive Telescope," presented at Bäckaskog Workshop on Extremely Large Telescopes, 2000.
- [6] P. B. Dierickx, E. Comeron, F. Gilmozzi, R. Gonte, F. Koch, F. and M. M. le Louarn, G. Spyromilio, J. Surdej, I. Verinaud, C., Yaitskova, N., "Owl Phase A Status Report," presented at Proc. SPIE 5489, Bäckaskog, Sweden, 2004.
- [7] J. K. Durr, Honke, R., von Alberti, M., Sippel, R., "Development and Manufacture of an adaptive lightweight mirror for space application," *Smart Material and Structures*, pp. 1005-1016, 2003.
- [8] J. D. Offenber, "JWST Fast Facts," 2004.
- [9] S. N. Gullapalli, Duffy, J., Crane, C., White, N., Lipkin, H., "Hinged Substrate for Large Aperture Lightweight Deformable Mirrors." USA, Patent Pending
- [10] G. S. Hickey, Lih, S.S., Barbee, T.W., Jr., "Development of Nanolaminate Thin Shell Mirrors," presented at Highly Innovative Space Telescope Concepts, 2002.
- [11] R. K. Tyson, *Introduction to Adaptive Optics*, vol. TT41, Bellingham: SPIE, 2000.
- [12] S. N. Gullapalli, Flood, R., Yang, E., Lih, S., "New Technologies for the Actuation and Control of Large Aperture Lightweight Optical Quality Mirrors," 2003
- [13] M. W. Born, E., *Principle of Optics*, 7 ed. Cambridge: Cambridge University Press, 1999.

- [14] S. N. Gullapalli, Flood, R., "Performance of Flexure Hinged Substrate-Nanolaminate Deformable Mirror Through Modeling and Simulation," presented at UV/Optical/IR Space Telescopes: Innovative Technologies and Concepts, San Diego, Ca., 2003.